# NONDESTRUCTIVE DETECTION OF POST-TENSIONING TENDONS AND SIMULATED VOIDS IN CONCRETE SPECIMENS USING THERMAL IMAGING

By

RYAN ROSS MUSGROVE

This thesis submitted in partial fulfillment of
the requirements for the degree of

MASTER OF SCIENCE IN CIVIL ENGINEERING

WASHINGTON STATE UNIVERSITY
Department of Civil and Environmental Engineering

MAY 2006

To the Faculty of Washington State University:

The members of the Committee appointed to examine the thesis of RYAN ROSS MUSGROVE find it satisfactory and recommend that it be accepted.

_____
Chair

_____

_____

# Acknowledgement

First, I would like to thank Dr. David Pollock for allowing me to work on this research project and for all of his help and guidance during my graduate curriculum. His easy-going attitude made the completion of this thesis and my graduate school experience much more enjoyable than I had expected it to be. I would like to thank Dr. William Cofer for serving on my committee and for his priceless assistance with my finite element models. Our hallway discussions of college football were always enjoyable when I needed a break from what I was working on. I would also like to thank Dr. Donald Bender for serving on my committee and for his valuable assistance throughout this research project.

I want to acknowledge Robert Duncan and Scott Lewis at the Wood Materials and Engineering Laboratory for all of their time and help during the experimental phase of my research. Helping me move my specimens in all types of weather conditions was greatly appreciated.

I would also like to thank my parents for all of their encouragement and financial support throughout my entire college experience. Their guidance and support helped me keep going with my schooling when I was discouraged and frustrated. I cannot thank them enough for everything they have done for me. Finally, I would like to thank my brother Ross for being there when I needed someone to talk to. Our conversations always helped cheer me up when I was having a bad day.

# NONDESTRUCTIVE DETECTION OF POST-TENSIONING TENDONS AND SIMULATED VOIDS IN CONCRETE SPECIMENS USING THERMAL IMAGING

## Abstract

by Ryan Ross Musgrove, M.S.
Washington State University
May 2006

Chair: David G. Pollock

When post-tensioning steel strands are used in concrete bridges, it is assumed that grout used in the post-tensioning ducts will encase the steel strands and prevent corrosion. However, corrosion of steel strands in grouted post-tensioning ducts has been observed during recent invasive inspections of bridges in Florida and Great Britain. The purpose of this research is to evaluate the use of thermal imaging as a nondestructive inspection method for locating post-tensioning steel strands and voids inside grouted ducts embedded in concrete.

Two-dimensional finite element models of heat flow through eight previously constructed concrete test specimens were developed. Incremental temperature loadings were applied to one face of the specimens to study the temperature distribution throughout the specimens. Models were developed with both insulated and uninsulated boundary conditions at the edges of the specimens.

Experimental testing of six of the concrete specimens was conducted by heating one face of the specimens. The specimens were heated using either solar energy, silicone rubber flexible heating blankets, or an infrared heater. Thermal energy propagation through the thickness of the specimens varied depending on concrete thickness and the embedded materials. This caused

surface temperature variations on the concrete specimens that were monitored with a thermal camera.

Detection of simulated voids and post-tensioning ducts with 5 cm (2 in) of concrete cover in 20 cm (8 in) thick specimens was possible with a temperature gradient of 11.1°C (20°F) obtained during solar heating and silicone rubber flexible heating blanket tests. Post-tensioning ducts and simulated voids were detected in specimens up to 30 cm (12 in) thick with a 75°C (135°F) temperature gradient using an infrared heater. The post-tensioning ducts were detected in 30 cm (12 in) thick specimens with a maximum of 15 cm (6 in) of concrete cover. Simulated voids were detected when concrete cover was less than 10 cm (4 in). The temperature trends observed for each specimen during the experimental research were very similar to the results predicted from the finite element models.

# Table of Contents

# List of Tables

# List of Figures

# Chapter 1 – Introduction and Objectives

## 1.1 – Introduction

The ability to locate and inspect post-tensioning steel strands inside the grouted ducts in prestressed concrete bridges has become a very important issue after corroded strands were detected during recent bridge inspections. The corrosion of the post-tensioning strands is attributed primarily to inadequate grouting procedures. When the ducts are not completely filled with grout during construction, the air voids in the grout are potential locations where bleed water can accumulate and cause corrosion of the exposed strands.

Post-tensioning bridge systems consist of concrete members, post-tensioning strands, ducts, anchorages, and grout. The ducts can be made from steel or high density polyethylene (HDPE). There are three common types of steel strands used for post-tensioning: cold drawn round wires, stranded cable, and alloy steel bars. In internal post-tensioned bridge systems, the hollow ducts are placed in the concrete bridge forms in specific locations. Therefore, the entire length of the duct is embedded inside the concrete section. The ducts are held in the desired profile by the surrounding concrete along the entire duct length. In external post-tensioning systems, the ducts are not encased in concrete. Used primarily in hollow box sections, the ducts pass through sleeves positioned in intermediate diaphragms along the section length to achieve the desired strand profile. External post-tensioning systems are easier to inspect compared to internal post-tensioning systems, but external systems have disadvantages not found in the internal post-tensioning systems. There is no reserve strength when an anchorage fails in an external system and the tendons are more susceptible to vandalism because they are not encased in the concrete bridge section (Breen et al., 2004).

After the concrete has cured, the post-tensioning strands are positioned inside the ducts. The strands are then anchored at one end of the bridge and stretched from the other end with hydraulic jacks until the correct tension is achieved. The strands are then anchored at the jacking end of the bridge. After the strands are tensioned and anchored, grout is pumped into the ducts to encase the tensioned strands.

The tension developed in the post-tensioning strands provides a compressive stress in the concrete section. This minimizes tension stresses in the concrete that would occur under normal loading conditions. Since concrete is weak in tension, this allows the section to withstand much larger service loads.

The grout used in the ducts serves two purposes in the post-tensioning system. When the grout cures, it creates a bond between the steel strands and the duct. This helps transfer the compressive stress caused by the steel strands into the concrete section. Additionally, the grout helps with corrosion prevention by covering the strands with a protective layer. This works quite well when the grouting process is completed in the approved manner. The duct is filled with grout by pumping the grout in one end of the duct until it flows out of the other end of the duct. This method theoretically fills the entire length of the duct completely full of grout. When the duct is completely filled with grout, the steel strands are protected from damage due to water or chloride penetration through the concrete section.

If the grout does not completely fill the duct and the steel strands are left exposed, locations of air cavities or voids will be present. These voids can then become locations where bleed water from the grout or outside corrosive agents can come in contact with the steel strands. This can lead to corrosion and in extreme events, eventual failure of the strands. Figure 1.1

presents an illustration of a typical steel strand anchorage with the grout port and a potential void area.

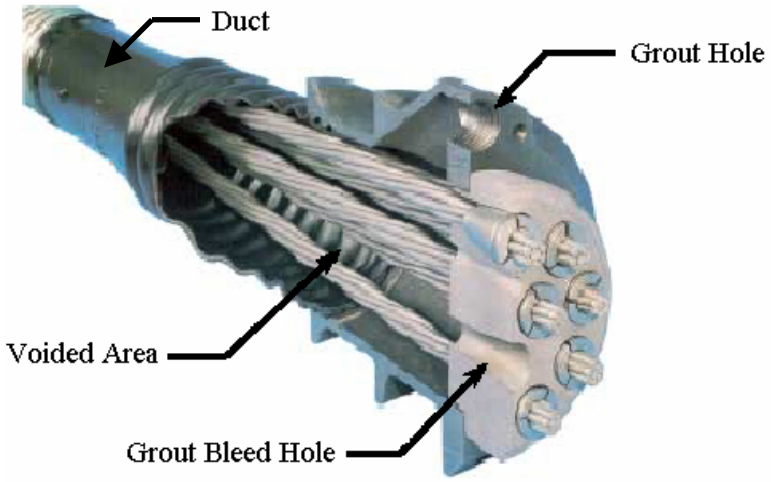


Figure 1.1 – Typical post-tensioning
strand anchorage (Chajes et al., 2003)

A study was conducted between 1992 and 1996 by the British and another was completed by the Florida Department of Transportation in 2000 that examined the condition of the steel strands in post-tensioned concrete bridges (Chandra et al., 2004). The basic conclusions of the reports were that the quality of construction materials needs to be improved and strict grouting procedures need to be specified. Additionally, a certification process should be implemented to ensure only skilled grouting contractors are used.

One of the bridges examined in the Florida study was the Mid-Bay Bridge which is located near Niceville, Florida. The bridge, which was completed in 1993, is approximately 5.8 km (3.6 mi.) long and spans the Choctawahatchee Bay. The superstructure is a precast segmental box girder consisting of 141 spans with an average span length of 41.5 m (136 ft) and a main span 68.6 m (225 ft). The post-tensioning system on the bridge is external and consists of six post-tensioning tendons (three on each side of the bridge) located in the interior cavity of the

bridge. A post-tensioning tendon is comprised of the steel strands, the duct, the anchorages, and the grout (Hartt and Venugopalan, 2002).

The ducts used in the Mid-Bay Bridge are four inches in diameter and are composed of HDPE. Each of the ducts are filled with 19 post-tensioning steel strands that are 16 mm (5/8 in) in diameter and span approximately eight to nine of the bridge segments. During a walkthrough bridge inspection in 2000, problems were observed with the bridge including two tendon failures. One of the tendons had multiple individual strand ruptures along the free length of the tendon between anchorages points. The other tendon was found to have completely failed at an anchorage point when the tendon pulled completely out of an expansion joint diaphragm. Additionally, the inspections revealed that the HDPE ducts exhibited multiple cracks along the lengths of the tendons (Frank et al., 2003). Figures 1.2 and 1.3 display some typical corrosion on strands taken from the Mid-Bay Bridge.

Figure 1.2 – Pitting corrosion on a post-tensioning strand from the Mid-Bay Bridge, Florida (Beitelman, 2000)

Figure 1.3 – Corroded strand ends removed from an anchorage in the Mid-Bay Bridge, Florida (Beitelman, 2000)

Corrosion of the steel strands was observed at various locations along the length of the tendons and at the anchorages. The corrosion of the strands near the anchorages was determined to be caused by two contributing factors. Possible accumulation of bleed water in the voids near the anchorage as indicated in Figure 1.1 and moisture and chloride penetration around the end protection were the main sources of the corrosion. This would not have been as much of a factor if the voids in those locations were not present. The voids near the anchorages were a result of excessive accumulations of bleed water, improper water content in the grout, and improper grouting practices (FDOT, 2001).

Corrosion along the length of the tendons also was caused by multiple factors. Bleed water in the voids and cracks or splits in the HDPE ducts were the most notable problems. The voids found along the length of the tendons were also a result of excessive accumulations of bleed water, improper water content in the grout, and improper grouting practices (FDOT, 2001). Testing was conducted on the HDPE ducts and it was established that the environmental stress cracking resistance (ESCR) of the HDPE material did not meet the standards at the time the bridge was constructed. Mechanical damage to the ducts was also observed in limited cases. The primary damage noted was intentional punctures. These punctures had been made in the ducts to check for voids in the grout during construction (Frank et al., 2003). Figure 1.4 shows a failure along the length of one of the tendons in the Mid-Bay Bridge.


Figure 1.4 – Failure of a tendon in the
Mid-Bay Bridge, Florida
(Breen et al., 2004)

As can be seen in the figures above, after only seven years of service, the Mid-Bay Bridge had significant structural damage to the post-tensioning system. After the inspections were completed and all of the major problems were addressed, eleven of the tendons had to be replaced at a cost of approximately $1 million dollars (Frank et al., 2003). Since the Mid-Bay Bridge had an external post-tensioning system, the tendons were not encased in the concrete cross section of the bridge, but the problems observed could occur in a similar fashion on an internal post-tensioning system.

In 1992, the Highways Agency in the United Kingdom implemented a ban on all construction of grouted post-tensioned bridges. The ban was not lifted until 1996, after an extensive study was conducted and a report was developed regarding the improved design and construction of these bridges. The report, "Technical Report 47 – Durable Post-Tensioned

Concrete Bridges", was completed by The Concrete Society in the United Kingdom. The study looked at all aspects of bridge design and detailing, the specification of grouting materials, and the qualifications required for the personnel completing the grouting procedures (Chandra et al., 2004).

During the study, 447 state-owned bridges throughout the United Kingdom were inspected for problems regarding the post-tensioning systems. Out of the 447 bridges inspected, 47% had no voids present in the grout, 23% had small voids, 18% had medium to large voids in the grout, and 12% had no grout at all. This means that 53% of the bridges inspected had some type of detectable problem with the post-tensioning system. Additionally, 10% of the bridges showed moderate to severe corrosion of the strands (VSL International, 2002).

The Florida Department of Transportation (FDOT) has adopted several new policies to minimize future problems in post-tensioned bridges. The FDOT now requires internal post-tensioning bridge systems to be constructed from only corrugated HDPE ducts with positively sealed connections. The post-tensioning ducts must be pressure tested before the grout is pumped into the ducts to ensure there are no leaks in the system. Additionally, the grout material that is used must minimize bleed water formation and must be pre-bagged (FDOT, 2002). Another thing that is being investigated is positive pressure injection of the grout throughout the ducts versus vacuum injection. Initial studies have shown that the vacuum injection does a more complete job of filling the duct with grout and minimizing voids. Figures 1.5 and 1.6 illustrate ducts that have been grouted with positive pressure injection and vacuum injection, respectively. The duct in Figure 1.5 grouted using positive pressure injection is not completely filled with grout and contains voids as indicated while the duct in Figure 1.6 grouted using vacuum injection does not contain any voids.

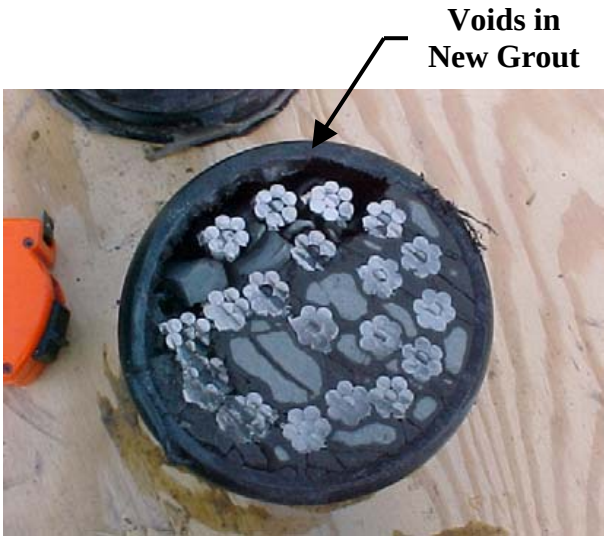


Figure 1.5 – Result of positive pressure injection of grout in a post-tensioning duct (FDOT, 2001)

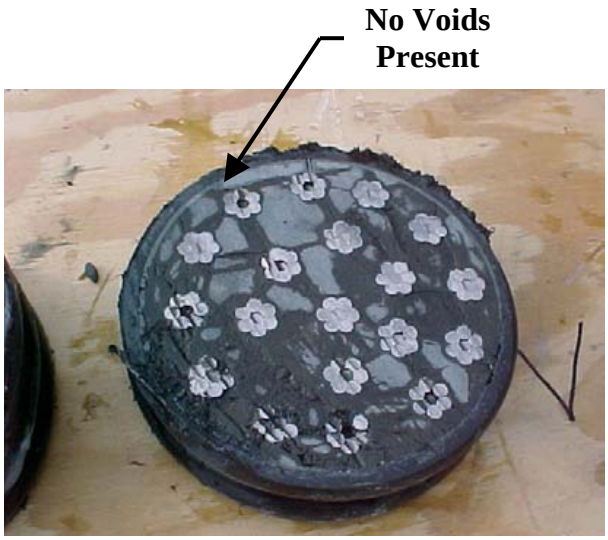


Figure 1.6 – Result of vacuum injection of grout in a post-tensioning duct (FDOT, 2001)

## 1.2 – Problem Statement

A primary problem with both external and internal post-tensioned bridge systems is that there is not an efficient and effective way to examine the post-tensioning strands and grout without damaging part of the structure. The steel strands are surrounded by grout inside the HDPE or steel ducts. In internal post-tensioning systems, the ducts are then located inside the concrete section and are typically surrounded by standard reinforcement. This makes the investigation of the steel strands very difficult. Current methods to inspect the strands and grout include removing the cover blocks from anchorages, removing the grout caps, drilling through grout vents, and drilling and cutting concrete to expose the ducts, which then can be cut open to inspect the strands (Potter, 2002).

There are several alternate methods that exist and have been implemented, but each has its drawbacks. Bore scope inspections require small holes to be drilled into the duct to allow a

small bore scope into the hole to take pictures of the void area. The problem with this method is that the duct can possibly move during construction, so numerous test holes may be required until the duct is found. If these holes are not sealed properly after the inspection is completed, they can become pathways for chloride and water penetration into the ducts. Additionally, care needs to be taken while drilling the test holes to ensure that the steel strands are not damaged by the drill bit. Another drawback to the bore scope inspections is that the test hole only allows inspection of a small area inside the duct. A void location or strand corrosion could be a small distance from the test hole and not be detected.

Another technique that has been used and has shown promising results is radiography (x-ray inspection). Radiography is the only current method that displays a clear 2-D image of the location of the post-tensioning ducts and displays the condition of the steel strands and void size and locations inside the ducts. One of the major downfalls of this method of testing is that it is cost prohibitive. The equipment costs are large and the need for the structure to be closed while the testing takes place increases the costs further. Additionally, radiation exposure from the x-ray testing can be harmful to personnel carrying out the bridge inspections (Serluppens and Shaw, 2000). Therefore, a method of inspection that is more cost effective and less hazardous to human health would be quite valuable.

Ground-penetrating radar (GPR) is another nondestructive method of inspection that has been investigated as a bridge inspection tool. GPR transmits electromagnetic waves with frequencies ranging from $3x10^{8}$ Hz to $3x10^{12}$ Hz through nonconductive materials. Materials with high conductivity reflect the electromagnetic waves making anything beneath the conductive material undetectable (Conner, 2004). Conner (2004) investigated using ground-penetrating radar to inspect grouted post-tensioning ducts embedded in concrete. Simulated

Styrofoam voids as small as 5 cm (2 in) in length were detected when embedded in HDPE ducts. The simulated voids embedded in steel ducts were not detected because of the high dielectric constant of the steel. The primary disadvantages of GPR are that only small areas of the bridge can be scanned at one time and voids embedded in steel ducts cannot be detected.

The research described in this report involves evaluating thermal imaging for locating post-tensioning tendons and detecting voids inside the post-tensioning ducts. Simply locating the post-tensioning tendons would be highly beneficial since the positions of the tendons may vary during construction. This research is directed toward post-tensioned box girder bridges because a temperature differential is required between the inside and outside surfaces of the box girder walls. This temperature differential will cause thermal energy to propagate through the wall and cause surface temperature variations depending on the internal discontinuities and materials embedded in the concrete.

This research is important since a cost-effective method for evaluating the condition of post-tensioning tendons is not readily available. With an effective nondestructive inspection method available, the problems seen in Florida and in the United Kingdom could be averted and public safety would be enhanced.

### 1.3 – Objectives

The goal of this study was to evaluate the use of thermal imaging as a nondestructive inspection method for locating post-tensioning tendons and detecting voids inside the post-tensioning ducts due to improper/incomplete grouting procedures. Concrete test specimens with simulated voids in grouted ducts were used to simulate the walls of concrete box girder bridges.

Thermal imaging is intended to be used as a nondestructive method of analysis for evaluating the in-service condition of the post-tensioning system.

The primary objectives of this research are:

- Develop a two-dimensional finite element model of heat flow through concrete test specimens.
- Verify the effectiveness of the finite element model through experimental analysis of six concrete test specimens.
- Determine the necessary temperature conditions to achieve useful thermal images for locating post-tensioning tendons with HDPE and steel ducts in 20 cm (8 in) and 30 cm (12 in) thick concrete specimens.
- Determine the temperature conditions required to attain thermal images that show locations of simulated voids inside grouted HDPE and steel ducts.
- Determine the feasibility of using thermal imaging to detect tendons and simulated voids in concrete specimens thicker than 20 cm (8 in).
- Determine the feasibility of using silicone rubber flexible heating blankets or an infrared heater to heat one surface of the concrete specimens to achieve larger temperature differentials than can be obtained through passive solar heating.

# Chapter 2 – Literature Review

## 2.1 – Thermal Imaging Background

All objects with a temperature above absolute zero emit infrared radiation. As an object is heated, molecular activity increases, thus resulting in a larger amount of infrared radiation being emitted. These emissions cannot be seen with the human eye. This is because infrared radiation is a form of electromagnetic radiation that occurs at wavelengths longer than visible light. The thermal radiation that is emitted is what is detected by thermal imaging cameras since the cameras cannot directly measure temperature or heat. The camera then converts this radiation into a visual temperature display of the surface of the object being examined (Infrared Training Center, 2002). Additionally, thermal cameras cannot see through objects. The images obtained only represent the surface temperatures of the object. Even though only surface temperatures will appear on the thermal camera display, information about subsurface conditions can be determined. These conditions, whether they are different materials or discontinuities, may cause localized differences in surface temperatures depending on the thermal properties that are associated with the conditions.

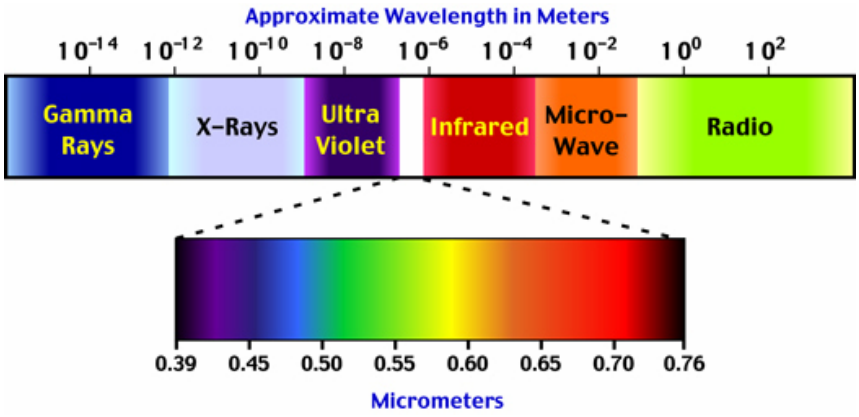


Figure 2.1 – Electromagnetic spectrum
(University of Arizona, 2004)

As previously stated, thermal cameras only display surface temperatures of objects being examined. To obtain valuable results, a temperature difference through the thickness of the object is mandatory. This difference in temperatures through the thickness of the specimen is also known as a temperature gradient. When there is a temperature gradient through the thickness of an object, heat transfer or flow occurs. The heat flows though the solid object by means of conduction (Jones and Botsko, 1995). Heat energy transfers from the warmer areas to the cooler areas until thermal equilibrium is reached. If the temperature gradient were not present, the temperature at the surface of the object would be constant and subsurface anomalies would not be evident.

The conduction of heat through materials with different thermal conductivities is what makes thermal imaging of post-tensioned box girder bridge walls possible. Thermal conductivity is a measure of the amount of heat that can be transferred through a unit thickness of material for a unit time duration and a unit temperature differential (Jones and Botsko, 1995). Internal anomalies with different thermal conductivities than the basic material will conduct heat at different rates. This difference in thermal characteristics will cause a warm or cool spot on the surface of a box girder wall directly beneath the subsurface anomaly in question. For example, steel, which has a thermal conductivity approximately twenty five times larger than that of normal weight concrete, will transfer heat at a faster rate and more efficiently than the normal weight concrete that surrounds it. Therefore, depending on whether the heated or unheated surface of the box girder wall is being viewed, the area beneath the location of the steel ducts or rebar embedded in concrete will appear warmer or cooler than the surrounding surface area depending on the direction the heat is flowing.

## 2.2 – Historical Development of Thermal Imaging Techniques

Thermal imaging is an inspection tool that has been used for over 30 years. Some of the initial applications of thermal imaging include military use and inspection of electric power distribution and transmission systems. During the Vietnam War and shortly thereafter, thermal imaging was researched and resulted in a number of military surveillance applications such as target locating, tracking, weapons guiding, and intelligence gathering (NDT Resource Center, 2001).

Inspection of transmission lines, substations, and distribution systems using thermal imaging has become a common practice in many countries. The problems that arise in these applications involve elevated electrical resistances which result in locations of elevated temperatures in the system. Loose connections, dirty contact surfaces, and broken strands in conductors are all possible conditions that may result in the elevated temperatures (Jones and Botsko, 1995). Additionally, thermal imaging has been used to inspect bushings or bearings that are not being lubricated properly, identify overloaded motors and pumps, and locate flaws or cracks in materials and machinery (NDT Resource Center, 2001). All of these problems can be a serious threat to public safety. Due to the increased heat generation in the component, thermal imaging is quite useful for inspection of these systems.

## 2.3 – Thermal Imaging Inspection of Structures

Thermal imaging has been used for a variety of different applications, but very little research has been conducted on locating post-tensioning ducts or voids embedded inside the ducts of post-tensioned concrete bridges. One study investigated using a finite element modeling program to identify specific conditions required to detect voids in post-tensioning ducts in a

laboratory environment. Additionally, two studies looked at running an electric current through the steel strands to identify possible locations of corrosion on the strands at void locations. Research has also been conducted for locating voids and delaminations in concrete bridge decks, grout inspection in concrete masonry unit (CMU) walls, and the detection of concealed inner-wall structural details in historic buildings.

An investigation to detect voids inside post-tensioning ducts by using finite element modeling in correlation with laboratory studies was conducted by researchers at the Technische Universität in Berlin, Germany. Models of the post-tensioning tendons were initially constructed in ANSYS, a finite element modeling software, to obtain the basic thermal parameters required to detect the voids during the laboratory testing. The model only displayed one quarter of the specimen because of symmetry. A constant heat-flux of 5 $kW/m^2$ (0.2 $BTU/min*in^2$) was applied to the top of the model for 500 seconds. The other surfaces were modeled as adiabatic. The maximum temperature difference was reached after 45 minutes. Further simulations concentrated on different diameters of ducts, varying amounts of steel strands, and different concrete covers (Hillemeier and Rieck, 2003).

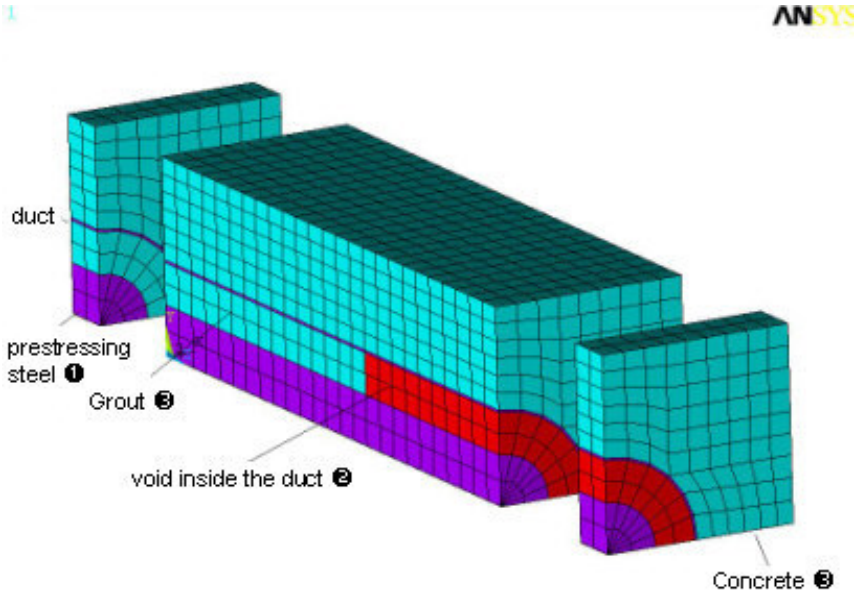


Figure 2.2 – Finite element model of a single duct
with a void (Hillemeier and Rieck, 2003)

To complete the investigation of detecting voids in the post-tensioning ducts, three concrete specimens were constructed, using two different types of tendons with cover depths varying from 5 cm (2 in) to 10 cm (4 in). Cylindrical, 40 cm (16 in) long air voids were located inside the ducts. One of the specimens was constructed with a rebar grid located 3 cm (1.2 in) beneath the surface of the concrete above and below the tendons. The specimens were heated using both internal and external heating sources. These heating methods included using the heat of hydration of the grout as an internal heating method as the grout hardens. Cement grouts generate heat during hardening as a result of the exothermic chemical process when the cement reacts with water to form a hard, stable paste. The heat generated is called heat of hydration (Cement Association of Canada, 2003). Another method used to internally heat the specimens was to heat the post-tensioning strands using a welder to generate electric currents ranging between 50 A and 100 A through the strands. Utilizing the electric resistance of the steel

strands, the applied current created a heat source inside the ducts. Finally, the specimens were heated externally using an infrared heater (Hillemeier and Rieck, 2003).

The method of using the heat of hydration of the grout provided some beneficial results. The heat developed was noticeable with the thermal camera within 30 minutes after the grout was placed inside the ducts. The voids were not visible with this method of heating, but the locations of all of the ducts were clearly visible (Hillemeier and Rieck, 2003).

Heating of the specimens using the infrared heater or by running electrical current through the post-tensioning strands also provided positive results. The 40 cm (16 in) long voids and the location of the tendons were detected at concrete cover depths of 5 cm (2 in) and 7 cm (2.8 in). The tendons and embedded voids with concrete cover of 10 cm (4 in) were too deep to be detected (Hillemeier and Rieck, 2003).

Another investigation using an electrical current to heat a section of rebar embedded in concrete was conducted at the University of Nebraska-Lincoln. The primary purpose of this study was to develop an alternative to solar heating of the concrete specimens. Using the sun for the thermal energy is effective, but is time and weather dependent. Three concrete specimens were constructed with a single uncoated piece of rebar 1.9 cm (3/4 in) in diameter placed along the centerline of each specimen. The approximate depth of the rebar below the concrete surface was 2.0 cm (0.8 in). Artificial defects were produced in two different pieces of rebar. In the first sample, notches were milled into the bar at 10 cm (4 in) increments along the length so that the cross-sectional area of the bar was reduced to 60%, 75%, and 90% of the original area. The notched areas were filled with a paste composed of iron oxide powder and acetone to simulate the thermal properties of corrosion products that would be present in the defect and allowed to dry. The second rebar specimen contained four “v-shaped” notches, each representing a 50%

reduction in cross-sectional area. The notches were oriented in 90° increments around the circumference of the rebar (Alexander, Krause, and Poulain, 1999).

Each of the specimens had an electrical current of 1500 A applied to the rebar for 30 seconds. All of the defects were distinguishable in the thermal images obtained for the specimen that had three different milled notches cut into the rebar to reduce the cross-sectional area. The thermal images of the specimen with the v-shaped notches cut at 90° increments around the rebar also provided valuable results. The notches that were located on the sides of the rebar were visible, but the notches located on the top and bottom of the rebar were not detected. It was believed that these regions were not apparent due to the iron oxide paste that was directly above or below the defect. The paste was cooler than the heated rebar and it was assumed that the improved heat flow through the rebar was minimized by the iron oxide paste, giving the appearance that no defect was present result in only these two locations (Alexander, Krause, and Poulain, 1999).

Delaminations in concrete bridge decks are another structural problem that researchers have used thermal imaging as a nondestructive method of inspection to try and locate these discontinuities. Delaminations occur when the steel reinforcement inside the concrete bridge deck corrodes, creating air-filled and debris-filled gaps that separate regions of the concrete. Currently, the main methods of inspecting for delaminations are visual inspections and dragging a chain over the roadway surface while listening for changes in the sounds created. Because these methods are slow and unreliable, researchers at the Lawrence Livermore National Laboratory (LLNL) developed a dual-band thermal imaging system to examine concrete bridge decks for delaminations.

The principle that makes the detection of the delaminations possible is known as thermal inertia. Thermal inertia is a bulk material property that is a measure of the resistance of a material to temperature change. It was found that the delaminated bridge decks have a below average thermal inertia, or exhibit above average day-night temperature variations, relative to the surrounding normal deck areas (Del Grande et al., 1996).

Single-band infrared (SBIR) thermal imaging has been used in previous research to detect delaminations in the concrete bridge decks. The problem with SBIR is that it is difficult to distinguish roadway surface features from the subsurface delaminations because of unwanted details on the thermal image. Dual-band infrared (DBIR) thermal imaging systems are improvements over SBIR systems because they read two separate ranges of wavelengths versus just one. This makes it possible to screen out the unwanted details in the thermal image caused by contaminants on the roadway surface and varying surface emissivities.

The first phase of the research involved construction of concrete slabs that were representative of a bridge deck. The slabs were 1.8 m (6 ft) square, 19 cm (7.5 in) thick, and had steel reinforcement embedded in them. Each of the slabs contained five simulated delaminations that were constructed from expanded polystyrene (Styrofoam) and were placed in the concrete specimens with 5 cm (2 in) of concrete cover. One of the slabs had an additional 5 cm (2 in) thick layer of asphalt applied to the top surface. Surface objects that produced clutter were placed at various locations on the top surface of the specimens. The square Styrofoam delaminations ranged from 10 cm (4 in) to 23 cm (9 in) across and between 3.2 mm (1/8 in) and 14.3 mm (9/16 in) in thickness.

During the testing, the concrete specimens were placed flat on the ground so the surface would be exposed to the direct sunlight. The DBIR thermal imaging cameras were mounted on a

tower constructed next to the specimens. Testing was conducted under various environmental conditions during the day and night of both the spring and winter. The results of phase one of the research found that the 23 cm (9 in) simulated delamination was on average 3.6°C (6.5°F) warmer during the daytime and 0.6°C (1.1°F) cooler than the surrounding concrete during the evenings. The 23 cm (9 in) square Styrofoam delamination that was covered with 10 cm (4 in) of concrete and asphalt was detected. However, the smaller delaminations were not detected in the specimen with 10 cm (4 in) of cover.

The second phase of the research conducted at the LLNL involved using the DBIR thermal imaging system to conduct bridge deck inspections at the Grass Valley Creek bridges near Redding, California. In order to perform the tests on the bridge decks, a mobile DBIR laboratory was constructed. The laboratory consisted of the DBIR cameras with image processing software, a camera mounting/positioning device, video recorder, and a 27 foot recreational vehicle. The camera mount was located about 4 m (12 ft) above the surface of the bridge deck on a telescoping mast attached to the vehicle.

According to the findings compiled by the researchers LLNL, the delaminated deck areas were about 2°C (3.6°F) to 3°C (5.4°F) warmer during the daytime hours and about 0.5°C (0.9°F) cooler in the evenings compared to the surrounding normal deck areas. These results can be attributed to the fact that the air in the gap of the delaminations does not transfer the thermal energy as well as the surrounding areas of concrete. The best times to carry out the thermal imaging of the bridge decks were between the hours of 12:00 P.M. and 3:00 P.M. for daytime testing and between the hours of 10:00 P.M. and 6:00 A.M. for testing at night. It was at these times that the temperature differences between delaminated areas and undamaged areas of bridge deck were the greatest (Del Grande et al., 1996). Due to the amount of research that has been

conducted on thermal imaging of bridge decks, American Society for Testing and Materials (ASTM) Standard D 4788-88 was developed to address the use of thermal cameras for detecting delaminations in bridge decks (Guthrie and Hema, 2005).

Thermal imaging has also been researched as a method to determine the presence and correct placement of the grouted cells in single-width concrete masonry unit (CMU) walls. This nondestructive testing method is needed because the current inspection method, which involves drilling small holes into the wall, does not cover a large area of the wall and is time consuming. The inspections are required to assure that the design specifications have been implemented correctly.

In order to create the required temperature gradient between the interior and exterior surfaces of the CMU walls, the heating ventilation and air conditioning (HVAC) system of the building was used. This created a temperature differential of approximately 13°C (23.4°F) between the interior and exterior wall surfaces (Allen and Stockton, 1999). Additionally, instead of heating the interior of the building to develop the required temperature gradient, solar radiation could also be used to heat the exterior surface of the wall. This is an excellent method to use during building construction when the HVAC system may or may not be operational.

Thermal energy from the sun during the month of July was strong enough to create the necessary temperature differential through the CMU walls. The thermal inertia of the grouted cells was higher than the non-grouted cells, which causes the grouted cells to retain heat longer than the non-grouted cells. These thermal differences allowed for the grouted and non-grouted areas to be easily distinguished with a thermal imaging camera (Allen and Stockton, 1999).

Thermal imaging was conducted at the St. Abbondio Abbey located in Como, Italy to determine the extent of renovation that had been implemented from the time when the building

was constructed. The building was believed to have been constructed in the 10th century A.D. and received extensive renovations in the 19th century. The main focus of the research on the Abbey dealt with detecting the boundaries of the original building and determining the texture of the most altered and damaged surfaces. This was a necessary preparation for a subsequent preservation project and would help uncover any unknown building modifications that had been completed.

Thermal imaging was used exclusively on the eastern wall of the complex. An interesting finding from the research was that direct sunlight could mask small deviations in temperature emanating from inside the wall. The testing was conducted at 8:00 A.M. on a cloudy day after 30 minutes of diffused radiation. The radiation becomes diffused when it is filtered through a thick cloud layer. The temperature gradient between the inside and outside faces of the walls was approximately 8°C (14.4°F) and was sufficient for the thermal inspections to be conducted. The obtained images clearly show locations of several ancient archways that were covered during past renovations near the ground level of the structure. Additionally, colder areas corresponding to water infiltration in the stucco were found. In one location of the building, a chimney was discovered encased in an existing wall. Thermal discontinuities in the walls also confirmed the use of molera stone bands in the façade, which helped date the renovations that occurred in that portion of the building back to 1868 (Bugini et al., 2003).

Similar research involving detection of discontinuities in walls and water infiltration using thermal imaging was conducted at the Santa Maria Incoronata Church in Martinengo, Italy by Ludwig in 1998. The surfaces of the walls being examined were covered with plaster with areas of fresco present. The heating was achieved by using warm air convection supplied by the church heating system. Due to the various materials that the walls were composed of, the walls

had to be heated for hours to obtain the necessary temperature gradient. Heat transfer simulation models predicted that the walls would have to be heated for at least four hours to increase the temperature of a 15 cm (6 in) thick 1°C (1.8°F).

Researchers found several locations throughout the church where openings that existed in the structure at one time had been filled in. Areas that were considered more homogeneous appeared colder than discontinuous areas or areas composed of several different materials due to the higher conductivity of the homogeneous material. Similarly, an area that contained an internal discontinuity would appear warmer due to the lower overall conductivity of the wall in that location. Delaminations of the fresco and detachments of plaster were also found. Additionally, analysis of one of the walls determined that at one time there was a balcony and a corridor in the middle of the church that was filled in during a past renovation (Ludwig, 2003).

Finally, an investigation regarding the feasibility of using thermal imaging to locate and inspect post-tensioning cables in concrete box girder bridges was conducted by Pearson in 2003. Six reinforced concrete specimens of varying thickness were constructed that contained both HDPE and steel ducts with varying depths of cover. Varying amounts of steel strands were placed in the ducts to represent different possible conditions for concrete box girder walls. There were ducts with 30 strands, 20 strands, and 4 strands in various layouts in the six specimens. Some of the ducts had small pieces of Styrofoam placed over the steel strands instead of grout to simulate voids inside the ducts. Standard reinforcement grids were located around the ducts. In order to create the required temperature gradient through the specimens, three insulated sheds were constructed to support the specimens. This allowed the interior surface to be heated or cooled while the exterior surface was heated or cooled by the outside environmental conditions.

Pearson (2003) found that it was possible to locate the tendons in a 20 cm (8 in) thick specimen when a temperature gradient of 20°C (36°F) or larger was present through the thickness of the specimen. Simulated voids located in the ducts of the 20 cm (8 in) specimen were also detected. It was noted that it was more difficult detecting the voids in the steel ducts than detecting the voids in the HDPE ducts. This was attributed to the larger thermal conductivity of the steel ducts counteracting the low conductivity of the simulated voids. Additionally, the standard reinforcing steel was visible in many of the images. Simulated voids and the locations of the tendons were not detected during inspection of the 30 cm (12 in) and 40 cm (16 in) thick specimens with the temperature gradient achieved. It took approximately 2.7 hours for the thermal energy to propagate through a 20 cm (8 in) thick specimen. Pearson (2003) also mentioned that a method or apparatus to minimize edge effects on the concrete specimens would help produce higher quality images. The edge effects masked the small temperature differences on the specimen surfaces that were a result of subsurface discontinuities (Pearson, 2003). Figure 2.3 displays a thermal image of a 20 cm (8 in) specimen with a 15 cm (6 in) long simulated void detected in the center of the specimen.

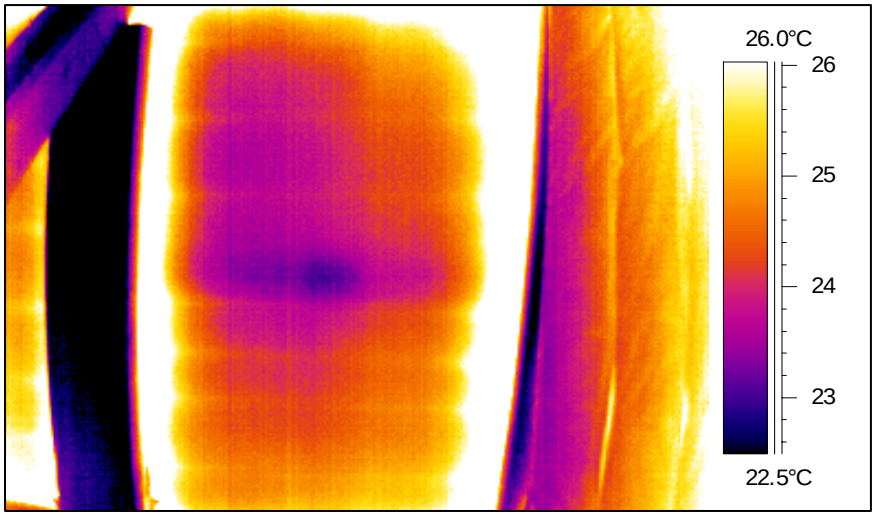


Figure 2.3 - Interior thermal image of a 20 cm (8 in) thick specimen (Pearson, 2003)

## 2.4 – Thermal Properties of Specimen Materials

Concrete has a relatively low thermal conductivity and therefore heats up very slowly. Normal weight concrete transfers heat in a more efficient manner than lightweight concrete. This can be attributed to the fact that the lightweight concrete has a lower density than normal weight concrete due to the porous aggregate used in the mix. The air pockets in the lightweight concrete provide a lower overall thermal conductivity.

When steel and concrete are used together in a reinforced, prestressed, or post-tensioned concrete system, different amounts of heat will propagate through the system in different locations. This is attributed to the different thermal conductivities of concrete and steel. When one surface of a concrete specimen with embedded steel is heated, the location of the steel would appear warmer than the surrounding concrete on the unheated surface. The thermal energy flows more efficiently through the steel than it does through the concrete because the steel is a much better conductor and has a much larger value of thermal conductivity.

To determine the time required for thermal energy to flow through the concrete specimens, the thermal diffusivity of normal weight concrete can be compared to known thermal lag values of lightweight concrete specimens. Thermal diffusivity measures the ability of a material to conduct thermal energy relative to its ability to store thermal energy. Thermal diffusivity is defined as (DeWitt and Incropera, 1996):

$$\alpha = \frac{k}{\rho \cdot c_p}$$

k = thermal conductivity

$\rho$ = density

$c_p$ = specific heat

$\alpha$ = thermal diffusivity

If a material has a large thermal diffusivity, it will transfer heat more rapidly than a material with a small thermal diffusivity. Considering both thermal conductivity and thermal diffusivity, a material's ability to transfer thermal energy can be quantified. Thermal conductivity is a constant value that designates the amount of heat that can be transferred across a unit thickness of material for a unit time duration and a unit temperature differential (Jones and Botsko, 1995). Materials with low densities and low thermal conductivities can still have large thermal diffusivities according to the equation. Air for example, is poor at transferring thermal energy compared to steel because of its low thermal conductivity, but it can transfer that heat more rapidly than steel due to its larger thermal diffusivity. Therefore, materials with high thermal conductivities will transfer larger amounts of thermal energy in a given time period where materials with large thermal diffusivities will be able to transfer that thermal energy at a faster rate.

Calculations were completed by Pearson in 2003 to determine the time required for thermal energy to travel through a 20 cm (8 in) thick specimen of normal weight concrete. Comparing thermal diffusivities for lightweight concrete specimens of a known thickness with the thermal diffusivities of normal weight concrete, the ratio between the diffusivities could be determined. Research conducted by Van Geem and Fiorato at the Oak Ridge National

Laboratories established that it took between five and six hours for thermal energy to travel through a 21 cm (8.1 cm) thick specimen constructed from lightweight concrete (Fiorato and Van Geem, 2003). Therefore, using the computed thermal diffusivities ratio of 2.3, the time for thermal energy to travel through a 20 cm (8 in) thick specimen constructed from normal weight concrete was calculated to be between 2.2 to 2.6 hours (Pearson, 2003). Table 2.1 displays values of thermal conductivity for each of the materials used in a post-tensioning concrete system.

| Material | Thermal Conductivity (W/m*K) |
|---|---|
| Normal Weight Concrete | 2.32 |
| Polyethylene | 0.39 |
| Steel | 50 |
| Air | 0.025 |
| Expanded Polystyrene | 0.027 |

Table 2.1 – Thermal conductivities of concrete specimen materials (MatWeb, 2005; Hukseflux Thermal Sensors 2003; Goss and James, 1993; Salazar, 2003; Callister, 2001)

**2.5 – Thermal Imaging Guidelines**

There are many factors to consider that may negatively influence the results of thermal imaging. Therefore, guidelines found in the Infrared Training Center (ITC) Level 2 Course Manual are helpful to assure that meaningful results are obtained. Some of the guidelines found in the Manual are given below.

Environmental conditions can have some of the largest effects on thermal images. Taking readings on a windy day can cause observed temperatures to be lower than actual temperatures. This is due to the convective cooling caused by the wind blowing over the object being surveyed. A constant wind blowing can completely eliminate a warm temperature region located on the surface of a specimen.

Testing in direct sunlight during days with very few clouds can also affect thermal images. Surface properties of the material such as reflectivity and emissivity affect the surface temperature readings obtained in direct sunlight. Reflectivity is a measure of the ability of a material to reflect thermal energy. When the energy from direct sunlight contacts the surface being examined, some of the energy is absorbed to heat the surface of the object and the rest of the energy is reflected. This reflected energy that is picked up by the camera can cause the camera to display incorrect surface temperature readings. Emissivity is the ability of a material to absorb and emit infrared radiation and is affected by material type, surface roughness, and the thermal camera viewing angle. Therefore, the emissivity of a material can vary without the temperature of the surface changing. This can cause the temperature recorded by the camera to change, when in reality the surface temperature remains constant.

Distances between the surfaces being targeted and the infrared camera can also affect the temperature readings collected. Taking a thermal image of a target at a distance farther than the spot size ratio of the specific camera lens permits may result in a recorded temperature lower than the actual temperature because the thermal camera takes an average from the surrounding area. If the target is too large to capture at the maximum viewing distance of the lens used, a wide angle lens can be used. Finally, things as simple as assuring the image is in focus on the camera can greatly affect the recorded temperatures. Images taken out of focus

will prevent the extreme temperatures from being captured. The smaller the target, the more pronounced this problem becomes (Infrared Training Center, 2002).

Pearson also discussed the problems with using the camera when direct sunlight is reflecting from the surfaces of concrete specimens. He noted that small differences in temperatures were difficult to detect due to reflection from the concrete surfaces. Taking thermal images of the specimens just after sunset provided the best results and was recommended for future research. When surface heating produced uneven temperature distributions, Pearson (2003) also recommended removing the heat source from the specimens and allowing the surface temperatures to equalize to achieve the best thermal image. The recommended equalization time was between 10 minutes and 45 minutes (Pearson, 2003).

**2.6 – Summary**

Based on the information in the literature review, subsurface discontinuities in concrete specimens can be detected under some conditions. A common aspect in all of the research was that the discontinuities detected were close to the surface being inspected. Delaminations in the concrete bridge decks were generally within 10 cm (4 in) of the surface. The research involving grout inspections of CMU walls confirmed the locations of ungrouted cells, but the detection depth was only the wall thickness of the CMU, which is less than 5 cm (2 in). Conclusions from the inspections of churches in Italy also indicated that discontinuities were less than 10 cm (4 in) from the surface of the wall.

The research conducted at LLNL showed that only the 23 cm (9 in) square Styrofoam delaminations could be detected with a concrete and asphalt cover depth of 10 cm (4 in) (Del Grande et al., 1996). Smaller delaminations at that depth of cover were not detected. Research

conducted by Pearson (2003) found that simulated voids in post-tensioning ducts could be detected in 20 cm (8 in) thick concrete specimens with 5 cm (2 in) of cover. Simulated voids, tendons, and standard reinforcement steel placement could not be detected in the specimens with 10 cm (4 in) and larger depths of concrete cover. Results from Pearson (2003) correlated well with the research conducted by Hillemeier and Rieck (2003) who also concluded that voids were not detectable when specimens with concrete cover depths of 10 cm (4 in) and larger were inspected. In both research conducted by both Pearson (2003) and researchers at LLNL, larger discontinuities were easier to detect than small ones.

In all of the research conducted, the temperature differentials between surfaces of the specimens were less than 25°C (45°F). Therefore, larger temperature differentials may allow for detection of discontinuities at deeper concrete cover depths. Additionally, materials with larger differences in thermal characteristics produced the most distinguishable results. Materials with similar thermal properties would make detection of discontinuities difficult at best.

# Chapter 3 – Finite Element Modeling

## 3.1 – Specimen Construction

Eight rectangular concrete specimens of various thicknesses were constructed to simulate concrete box girder bridge walls containing post-tensioning ducts by Pearson (2003) and Conner (2004). The sample sections were 102 cm (40 in) wide by 163 cm (64 in) long with thicknesses of 20 cm (8 in), 30 cm (12 in), or 40 cm (16 in). The thicknesses were chosen because they are common wall thicknesses in post-tensioned concrete box girder bridges. The 20 cm (8 in) thick specimens are the thinnest section that can accommodate a 10 cm (4 in) diameter duct and still have room for a rebar grid with 2.5 cm (1 in) of concrete cover (Pearson, 2003).

The concrete used for the specimens was a seven-sack mix containing a maximum crushed rock aggregate size of 1.9 cm (0.75 in). The mix from two separate batches had a measured slump of 15 cm (6 in) to 20 cm (8 in) and a target compressive strength of 34.5 MPa (5000 psi). Compressive strength tests were conducted for the specimens constructed by Conner and determined the average 28 day compressive strength of the concrete was 33 MPa (4800 psi) (Conner, 2004).

In order to simulate an actual box girder wall, a rebar grid was placed near each face of the specimens for standard reinforcement. The rebar was a No. 5 Grade 60 bar spaced at approximately 20 cm (8 in) on center for Specimen 1 through Specimen 6 (Pearson, 2003). Specimen 7 and Specimen 8 contained No. 4 Grade 60 bars spaced at approximately 30 cm (12 in) on center. The rebar cage was constructed to maintain concrete cover to the rebar of at least 2.5 cm (1 in) on all faces (Conner, 2004).

The post-tensioning ducts used in each of the specimens were either high density polyethylene (HDPE) or steel with a nominal 10 cm (4 in) diameter. The steel ducts were chosen because they are the most commonly used in Washington State. However, HDPE ducts are becoming more popular in many other states because of their corrosion resistance and durability during construction. The HDPE ducts had a wall thickness of approximately 3.0 mm (0.12 in) while the steel ducts were approximately 1.5 mm (0.06 in) thick.

Each specimen contained three post-tensioning ducts extending across the 102 cm (40 in) width, spaced at approximately 40 cm (16 in) on center. The ducts in the 20 cm (8 in) thick specimens and one 30 cm (12 in) specimen were placed at mid-thickness in the specimens to achieve identical concrete cover on both surfaces. In the other 30 cm (12 in) and 40 cm (16 in) thick specimens, the ducts were positioned at different depths in the specimens to provide varying concrete cover to each face (Pearson, 2003). In some of the specimens, the ducts shifted slightly from their original positions during construction. Figure 4.1 shows the formwork, rebar, and post-tensioning ducts for two 20 cm (8 in) thick specimens and one 40 cm (16 in) thick specimen.

Figure 3.1 - Formwork, rebar and post-tensioning ducts in 20 cm (8 in) and 40 cm (16 in) thick specimens (Pearson, 2003)

Various quantities of post-tensioning steel strands were inserted in each of the ducts after the concrete had cured and the forms were removed. The amount of steel used in each duct was varied to replicate various steel layouts in a post-tensioned bridge. An investigation conducted on a post-tensioned box girder bridge in Seattle, Washington by Pearson (2003) concluded that full length post-tensioning ducts in the bridge contained 31 steel strands and intermediate ducts contained 22 strands per duct. Therefore, the specimens were constructed containing 30, 20, and four steel strands to simulate the full length and intermediate tendons of a post-tensioned box girder bridge wall. The ducts with only four steel strands contained 15 cm (6 in) long Styrofoam specimens to simulate a large void in the grout. The steel strands used in the specimens were 1.3 cm (1/2 in) diameter seven wire AASHTO M203 Grade 270 strands. Specimen 7 and Specimen

8 each contained one tendon with steel strands that had been exposed to outside weather conditions for 12 months to allow them to corrode (Conner, 2004).

The simulated voids in the post-tensioning ducts were Styrofoam pieces placed adjacent to the steel strands inside the ducts. The simulated voids in Specimen 1 through Specimen 6 were 15 cm (6 in) long and were placed directly at mid-length of the ducts (Pearson, 2003). Some of the ducts in Specimen 7 and Specimen 8 contained smaller voids that were 5 cm (2 in) or 10 cm (4 in) long. The Styrofoam pieces were cut to fill the ducts as completely as possible and were placed approximately 35 cm (14 in) from each end of the duct (Conner, 2004).

When the steel strands were inserted into the post-tensioning ducts, the specimens were lying flat on the ground. The post-tensioning steel strands were then placed in the bottom of the ducts. After the steel strands were placed in each duct, the Styrofoam voids were placed on the steel strands inside the ducts at the desired locations. Therefore, the simulated voids were located closer to one surface of the specimen, while the post-tensioning steel strands were located closer to the opposite surface of the specimen. The orientation of the steel strands and simulated voids is illustrated in Figure 3.2

Table 3.1 lists the duct layouts, steel strand quantities, and concrete cover for each specimen. The concrete cover for each duct refers to the distance between the face of the concrete specimen and the surface of the post-tensioning duct. The concrete cover designation used in table 3.1 refers to the depth of cover to each surface of the specimen. For example, the designation of 7.5 cm - 12.5 cm (3 in - 5 in) listed for the center duct of Specimen 3 indicates that the surface of the duct is located 7.5 cm (3 in) beneath one face of the specimen and 12.5 cm (5 in) beneath the opposite face (Pearson, 2003). This designation provides the location of any duct not located directly at mid-depth in the specimen. The designation top, center, and, bottom

was used in Table 3.1 and throughout the report because the tendon adjacent to the specimen lifting hooks was always at the top of the specimen for all of the thermal imaging tests. Figure 3.2 illustrates the cover depth designation and provides construction details for Specimen 5.

The grout used in each of the ducts was PTX cable grout manufacturer by The Euclid Chemical Company for post-tensioning applications. The specimens were tilted on blocks so the grout could be poured into the ducts after the post-tensioning steel strands were inserted in the ducts. During the grouting process, the Styrofoam pieces were inserted into the selected ducts to create simulated voids (Pearson, 2003).

**Specimen 1: 20 cm (8 in) Thick**

| Tendon Location | Concrete Cover | Duct Material | Steel Strands Per Duct | Simulated Voids |
|---|---|---|---|---|
| Top | 5 cm (2 in) | Steel | 20 | No |
| Center | 5 cm (2 in) | Steel | 30 | No |
| Bottom | 5 cm (2 in) | Steel | 30 | 1 Void |

**Specimen 2: 20 cm (8 in) Thick**

| Tendon Location | Concrete Cover | Duct Material | Steel Strands Per Duct | Simulated Voids |
|---|---|---|---|---|
| Top | 5 cm (2 in) | Steel | 4 | 1 Void |
| Center | 5 cm (2 in) | HDPE | 4 | 1 Void |
| Bottom | 5 cm (2 in) | HDPE | 30 | No |

**Specimen 3: 30 cm (12 in) Thick**

| Tendon Location | Concrete Cover | Duct Material | Steel Strands Per Duct | Simulated Voids |
|---|---|---|---|---|
| Top | 10 cm (4 in) | Steel | 30 | No |
| Center | 7.5 cm - 12.5 cm (3 in - 5 in) | Steel | 20 | No |
| Bottom | 5 cm - 15 cm (2 in - 6 in) | Steel | 30 | No |

**Specimen 4: 30 cm (12 in) Thick**

| Tendon Location | Concrete Cover | Duct Material | Steel Strands Per Duct | Simulated Voids |
|---|---|---|---|---|
| Top | 10 cm (4 in) | Steel | 4 | 1 Void |
| Center | 7.5 cm - 12.5 cm (3 in - 5 in) | HDPE | 20 | No |
| Bottom | 10 cm (4 in) | HDPE | 30 | No |

**Specimen 5: 40 cm (16 in) Thick**

| Tendon Location | Concrete Cover | Duct Material | Steel Strands Per Duct | Simulated Voids |
|---|---|---|---|---|
| Top | 15 cm (6 in) | Steel | 30 | No |
| Center | 12.5 cm - 17.5 cm (5 in - 7 in) | Steel | 20 | No |
| Bottom | 10 cm - 20 cm (4 in - 8 in) | Steel | 30 | No |

**Specimen 6: 40 cm (16 in) Thick**

| Tendon Location | Concrete Cover | Duct Material | Steel Strands Per Duct | Simulated Voids |
|---|---|---|---|---|
| Top | 15 cm (6 in) | HDPE | 30 | No |
| Center | 12.5 cm - 17.5 cm (5 in - 7 in) | HDPE | 20 | No |
| Bottom | 15 cm (6 in) | Steel | 4 | 1 Void |

**Specimen 7: 20 cm (8 in) Thick**

| Tendon Location | Concrete Cover | Duct Material | Steel Strands Per Duct | Simulated Voids |
|---|---|---|---|---|
| Top | 5 cm (2 in) | HDPE | 20 | No |
| Center | 5 cm (2 in) | HDPE | 20 | 2 Voids |
| Bottom | 5 cm (2 in) | HDPE | 20 (Corroded) | No |

**Specimen 8: 30 cm (12 in) Thick**

| Tendon Location | Concrete Cover | Duct Material | Steel Strands Per Duct | Simulated Voids |
|---|---|---|---|---|
| Top | 10 cm (4 in) | HDPE | 20 (Corroded) | No |
| Center | 10 cm (4 in) | HDPE | 20 | 2 Voids |
| Bottom | 10 cm (4 in) | HDPE | 30 | 2 Voids |

Table 3.1 – Duct positions, duct materials, and steel strand quantities for Specimens 1 – 8 (Pearson, 2003; Conner, 2004)

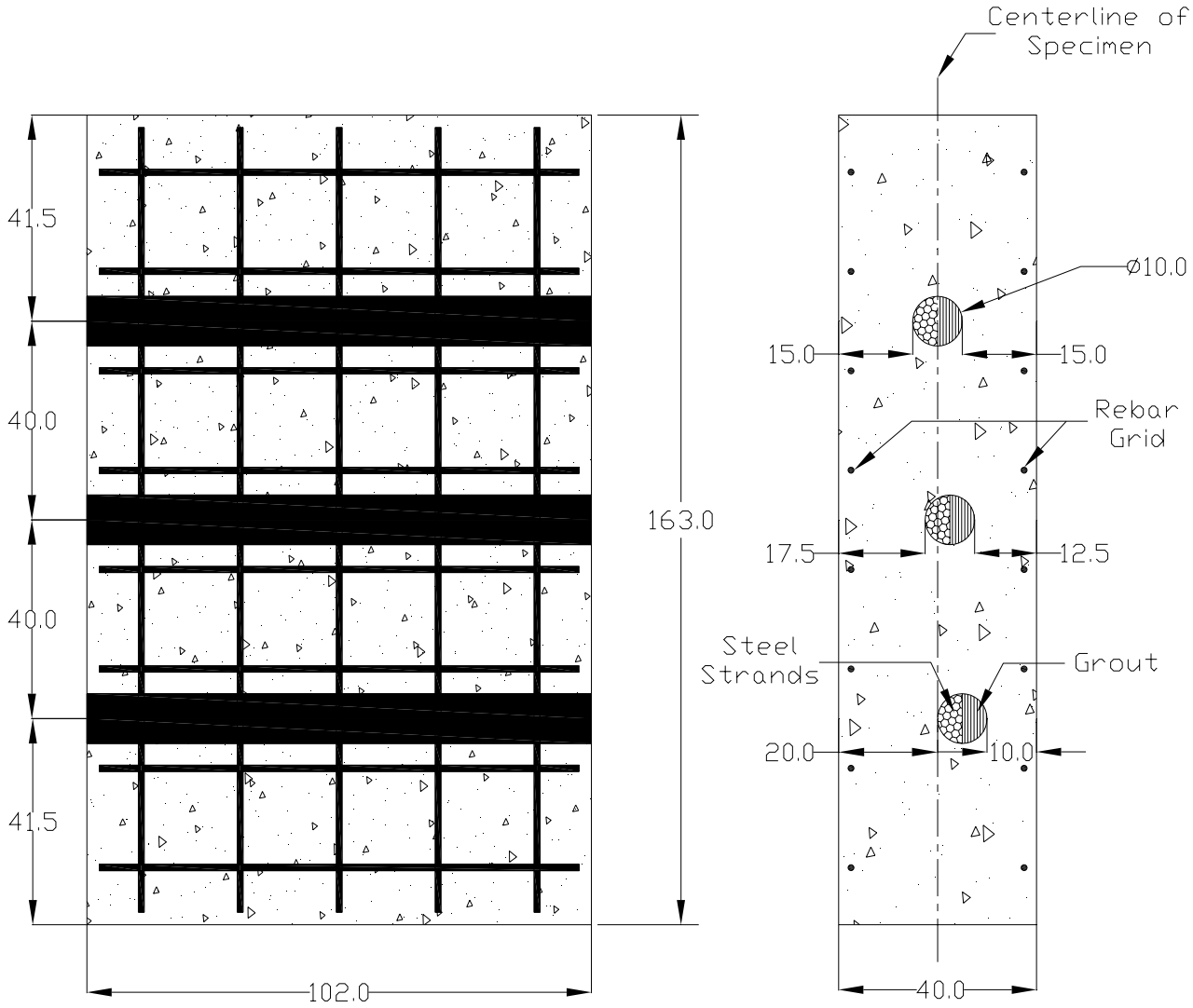


Figure 3.2 – Construction details for Specimen 5.
All dimensions are in centimeters

### 3.2 – Introduction

In order to evaluate the thermal conditions required to detect tendons and discontinuities in the specimens constructed by Pearson (2003) and Conner (2004), finite element models were created representing each of the eight specimens. Models of the specimens were created using the commercial software ADINA Version 8.2. The models were created in the ADINA-T section of the software which is used for thermal analyses. The completed models were analyzed

and the results were obtained in the ADINA-PLOT division of the software. Output data from ADINA-PLOT was transferred into Microsoft Excel for analysis and to allow for data comparison between the different specimens.

Three main types of analysis were emphasized during the modeling portion of the research. Models were developed with a temperature loading applied on one edge and the other edges of specimens were modeled with air temperature convection loadings. Models were also developed with the same applied temperature loadings and the edges along the thickness of the specimens modeled as insulated boundary conditions. Additionally, models were constructed that eliminated the voids in each specimen to determine the baseline temperature profile if the specimens did not contain any voids. This data was compared to the results obtained from models containing voids to quantify the temperature reduction caused by each size void. All of the models were two-dimensional replicas of the cross section of the specimens. The cross-sections were modeled as a slice cut through the long dimension of the specimens. This allowed each of the three different tendons to be included in the model.

The entire cross-section of each specimen was modeled because the specimens were not symmetrical due to varying cover depths, various amounts of post-tensioning steel, and different duct materials that were used throughout the cross-section of the specimens. Each specimen was constructed using normal weight concrete, rebar, post-tensioning steel, grout, HDPE or steel ducts, and Styrofoam for simulated voids. Thermal conductivities for these materials were used in the finite element models based on information given in the literature review. Since grout and concrete are both cement based mixes, the grout was assumed to have the same thermal conductivity as normal weight concrete.

The models were developed using eight-node quadrilateral elements for the mesh created on the face of the models. Each model was created in the same manner with respect to the mesh density used. The mesh density was kept constant around the boundary edges of the model. Near each of the post-tensioning tendons and the standard steel reinforcement, the mesh density was increased to provide more accurate results as the heat flux traveled through the different material interfaces. The mesh density was specified by defining the length of each finite element along any edge of the model. The 20 cm (8 in) thick models used a finite element edge length of 0.5 cm (0.2 in) around the perimeter of the model and the 30 cm (12 in) and 40 cm (16 in) thick models used a length of 0.75 cm (0.3 in). The finite element edge length for all of the interior edges of the models was set at 0.15 cm (0.06 in) for all specimens. After the mesh density was defined, the auto-mesh function in ADINA was used to develop the mesh for the entire model.

Since the amount of post-tensioning steel varied for each specimen, an area of steel in each duct needed to be determined. To simplify the modeling process, the steel strands in the ducts were modeled as a solid mass rather than as individual strands. This was assumed to closely approximate the actual condition in a bridge since the seven-wire steel strands are packed tightly together when tensioned. The height to the top of the strands was measured from the inside surface of the ducts and used in the model as the height inside the duct for the location of the steel-grout interface. For the ducts containing four, 20, and 30 steel strands, the height of the steel inside the duct was measured at 1.25 cm (0.5 in), 4.5 cm (1.8 in), and 6.0 cm (2.4 in) high, respectively. Figure 3.3 illustrates modeling of the tendons using an approximate area of steel for the post-tensioning steel strands.

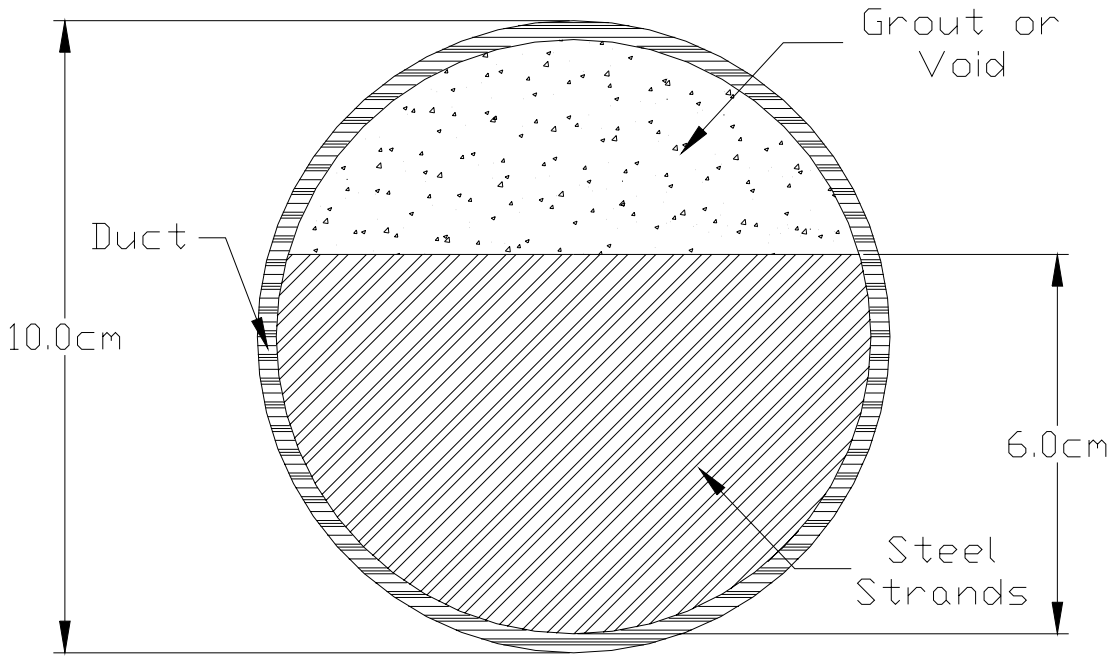


Figure 3.3 – Typical tendon model with 30 post-tensioning steel strands in a 10 cm (4 in) diameter HDPE duct

There were five different planar conduction elements used in the models that represented concrete, steel, grout, HDPE, and Styrofoam. Planar line boundary convection elements were used to account for the cooling that occurred at the air-concrete interface on the three unheated boundary edges of the specimens. The value for the heat transfer coefficient used in the finite element models for the air-concrete interface was 34 $W/m^2*K$ (5.9 $BTU/hr*ft^2*°F$). The value was within the range of values listed in the ASHRAE Fundamentals Handbook for air circulating at less than 24.1 kph (15 mph) (ASHRAE, 1989).

The boundary convection edges were developed with an applied ambient temperature of 23.9°C (75°F) which represents an approximate daytime temperature during the spring and summer months. This temperature was initially applied on the three surfaces of the model that were not being heated. Temperatures of 37.8°C (100°F), 65.6°C (150°F), 93.3°C (200°F), and 148.9°C (300°F) were applied successively to the heated surface of the 20 cm (8 in) thick

specimens. For the 30 cm (12 in) thick specimens, temperatures of 93.3°C (200°F), 148.9°C (300°F), 204.4°C (400°F), 260°C (500°F), and 315.6°C (600°F) were applied successively to the heated surface. Temperatures of 93.3°C (200°F), 148.9°C (300°F), 204.4°C (400°F), 260°C (500°F), 315.6°C (600°F), 371.1°C (700°F), and 426.7°C (800°F) were applied successively to the heated surface of the 40 cm (16 in) thick specimens. The temperatures on the opposite unheated surface were then plotted in Microsoft Excel.

Figure 3.4 displays the applied convection and temperature loadings with three different amounts of post-tensioning steel in a 30 cm (12 in) thick specimen. The values in Figure 3.4 have units of degrees Celsius. The green color designates areas of concrete, while the red color represents locations of steel. This could designate the location of the rebar, the post-tensioning steel strands, or the steel ducts. The magenta colored arrows represent either prescribed temperature or prescribed convection temperature loadings. Blue represents the locations of grout and orange designates locations of Styrofoam voids located inside the ducts. Lastly, purple represents the HDPE duct material. In each finite element model, the top surface was the only surface modeled with an applied temperature loading.

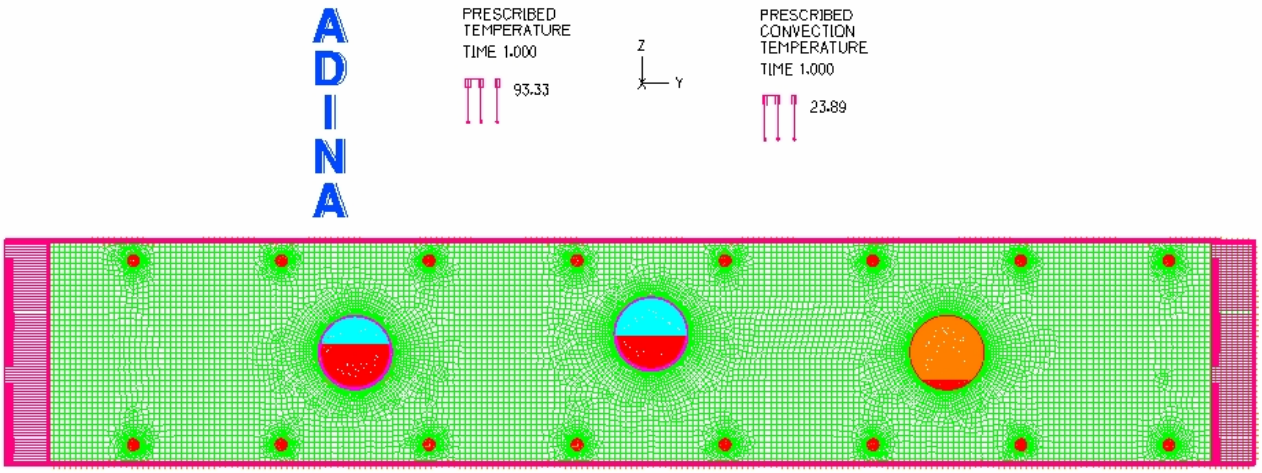


Figure 3.4 – Finite element model of 30 cm (12 in) thick specimen displaying three different amounts of post-tensioning steel

### 3.3 – Uninsulated Boundary Conditions

The first models of the specimens were developed with three of the boundary edges modeled as convection edges. This closely modeled the thermal loading achieved by the testing setup used by Pearson (2003) and specimen heating conducted using silicone rubber flexible heating blankets. The models were developed using the exact measurements recorded by Pearson (2003) and Conner (2004) during specimen construction.

All of the ducts in 20 cm (8 in) thick Specimen 1 were steel. The bottom duct (located near the right edge of the specimen in Figure 3.5) contained 30 post-tensioning steel strands with a 15 cm (6 in) long by 3.7 cm (1.5 in) thick simulated void. The top duct (located near the left edge of the specimen in Figure 3.5) contained 20 steel strands and the center duct contained 30 steel strands, each without simulated voids. The depth of concrete cover to each of the tendons was 5 cm (2 in). Figure 3.5 displays the temperature distribution throughout the cross-section of Specimen 1 for a 93.3°C (200°F) applied temperature loading.

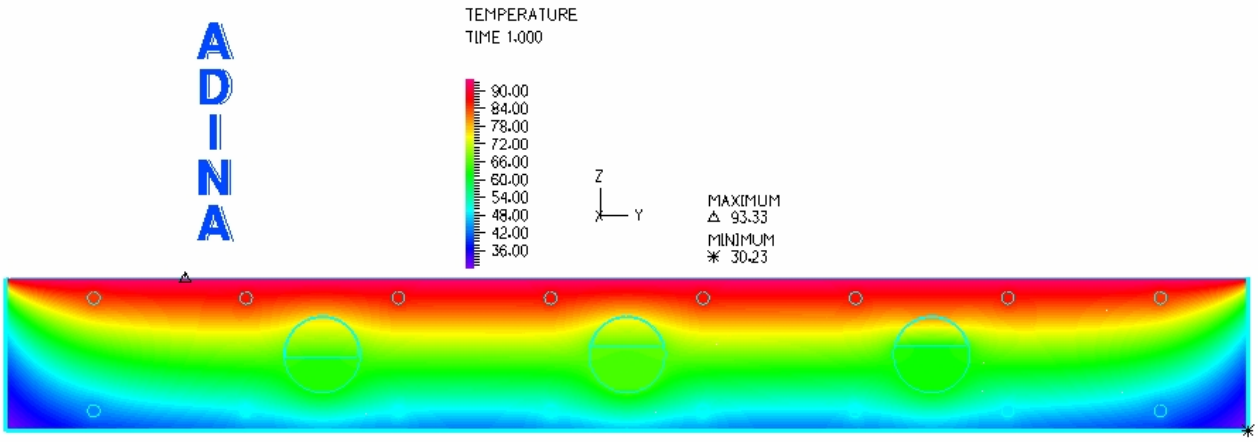


Figure 3.5 – Temperature distribution throughout Specimen 1
with a 93.3°C (200°F) temperature loading from ADINA

The center duct transferred heat the most efficiently due to the 30 post-tensioning steel strands within the duct without the presence of a void. Therefore, during testing the location of the center duct should appear the warmest on the unheated surface. Heat was transferred least efficiently through the duct with the 30 steel strands and a simulated Styrofoam void. The location of each of the tendons should appear as warm spots on the unheated surface during testing.

The temperature profile of Specimen 1 along the bottom surface clearly shows that temperature gradients larger than 14°C (25.2°F) between the surfaces of the concrete should be adequate to detect the location of each tendon. Figure 3.6 illustrates a plot of the temperature profile as a function of position along the bottom surface of the model for four different temperature loadings for Specimen 1. An applied temperature of 93.3°C (200°F) or temperature differential through the thickness of Specimen 1 of 65°C (117°F) results in almost a 5°C (9°F) warmer surface temperature at locations where the ducts were present. The locations of the ducts should be visible when viewed with a thermal imaging camera since the camera can detect temperature differences as small as 0.1°C (0.2°F). A temperature gradient of approximately 15°C (27°F) obtained from the 37.8°C (100°F) applied temperature loading resulted in a 1°C (1.8°F) warmer surface temperature at locations where the ducts were present. However, since the two-dimensional model does not address three-dimensional heat flow in the specimen, it is questionable that the tendons could not be detected with a temperature gradient of 15°C (27°F).

Another main point to observe was the obvious decrease in temperature between the outside ducts and the uninsulated edges. This was present in all of the uninsulated boundary condition models. This was attributed to the convective cooling from the ambient air conditions that was modeled on the three unheated surfaces. In the 30 cm (12 in) and 40 cm (16 in) thick

specimens where the convection cooling was more predominant, the surface temperature variations caused by materials embedded in the specimens were more difficult to detect near the edges of the specimens. Warm spots on the unheated specimen surface caused by embedded steel were masked by the convection cooling.

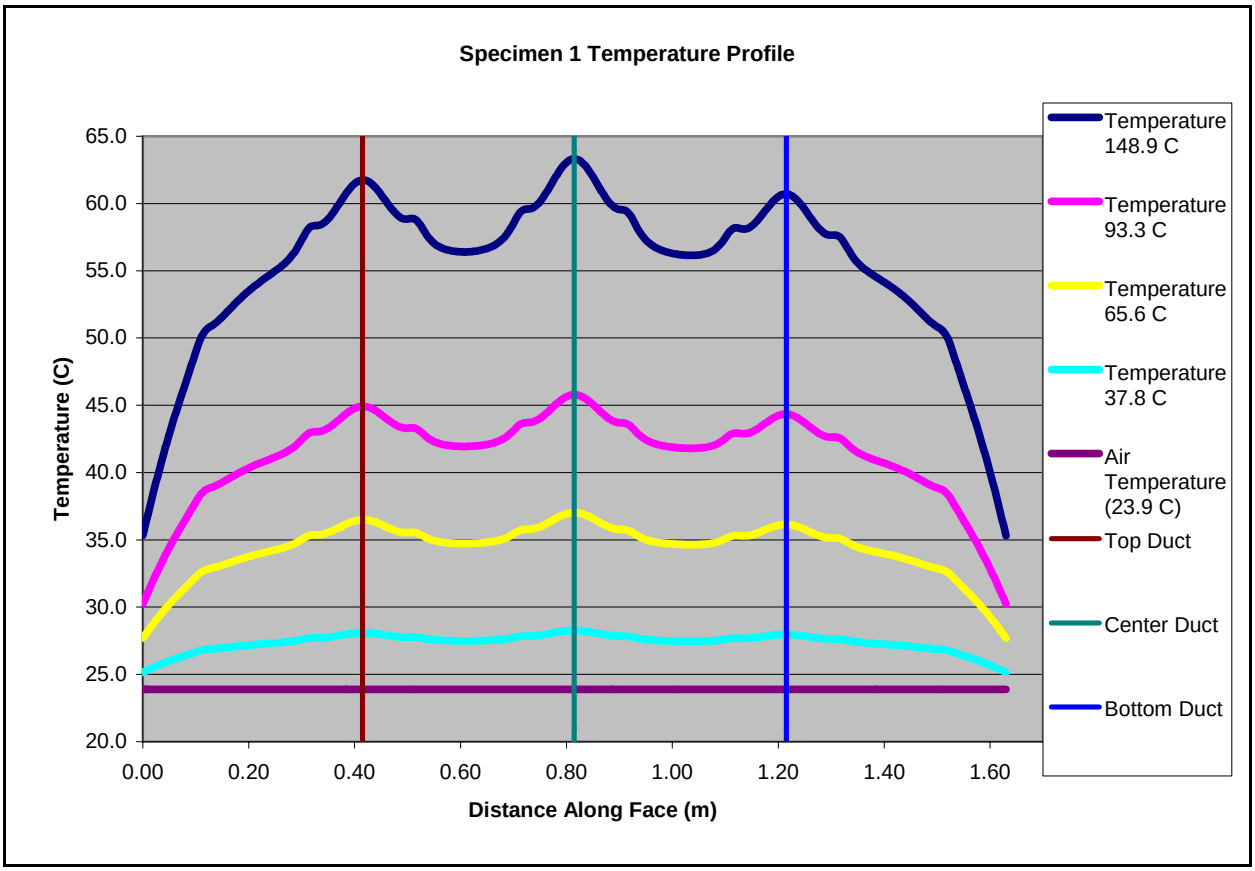


Figure 3.6 – Temperature profile along bottom surface
of Specimen 1 for various temperature loadings

Specimen 2 was 20 cm (8 in) thick and featured two HDPE ducts and one steel duct with the center HDPE duct containing four post-tensioning steel strands and a 15 cm (6 in) long by 8.5 cm (3.3 in) thick simulated void. The top steel duct (located near the right edge of the specimen in Figure 3.7) also contained four post-tensioning steel strands and a 15 cm (6 in) long by 8.5 cm (3.3 in) thick simulated void. The bottom HDPE duct (located near the left edge of the

specimen in Figure 3.7) contained 30 steel strands without a simulated void. The main focus of this model was to distinguish the differences between simulated voids located in HDPE versus steel ducts since the model has two tendons that contain the same amount of steel strands, but different duct materials. The depth of cover to each of the tendons was 5 cm (2 in). Figure 3.7 displays the temperature distribution throughout the cross-section of Specimen 2 for a 93.3°C (200°F) applied temperature loading.

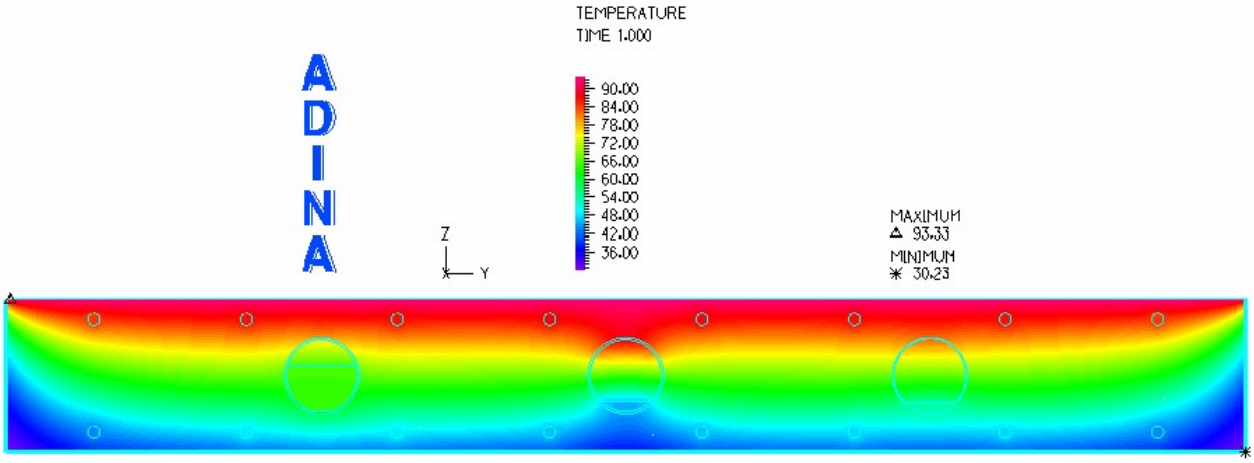


Figure 3.7 - Temperature distribution throughout Specimen 2
with a 93.3°C (200°F) temperature loading from ADINA

The finite element model for Specimen 2 established that the bottom duct transferred heat most efficiently due to the 30 post-tensioning steel strands within the duct. This is the same scenario as in Specimen 1 and the results between the two models are quite similar. The location of the center tendon should appear the coldest on the unheated surface because the thermal energy was transferred the least efficiently through this tendon. This can be attributed to the fact that the center duct was made from HDPE, there were only four post-tensioning steel strands in the duct, and a large simulated void was placed on top of the steel. The tendon with the 30 post-

tensioning steel strands enclosed in the HDPE duct should appear the warmest of the three tendons due to the large amount of steel on the unheated surface of the specimen.

The temperature profile of Specimen 2 also shows that temperature gradients larger than 15°C (27°F) between the specimen surfaces should produce at least 1°C (0.9°F) temperature differences on the specimen surface. Figure 3.8 is a temperature profile plot with respect to position along the bottom surface of the model for four different temperature loadings for Specimen 2. Similarly to Specimen 1, an applied temperature loading of 93.3°C (200°F) results in approximately a 4°C (7.2°F) temperature difference occurring between the center HDPE tendon with the four steel strands and the location where no tendons were present. The center HDPE duct containing four steel strands and the bottom steel duct containing 30 steel strands should be the most distinguishable with the thermal camera. Also, the 15°C (27°F) temperature gradient obtained from the 37.8°C (100°F) applied temperature loading should still provided at least a 1°C (1.8°F) temperature difference on the surface to facilitate in obtaining meaningful thermal images. One interesting thing to note is the difference in maximum surface temperatures between the steel tendon with 30 steel strands of Specimen 1 and the HDPE tendon with 30 steel strands. The HDPE tendon resulted in a surface temperature 5°C (9°F) cooler than the steel tendon. This can be attributed to the lower thermal conductivity of the thicker HDPE duct compared to the steel duct.

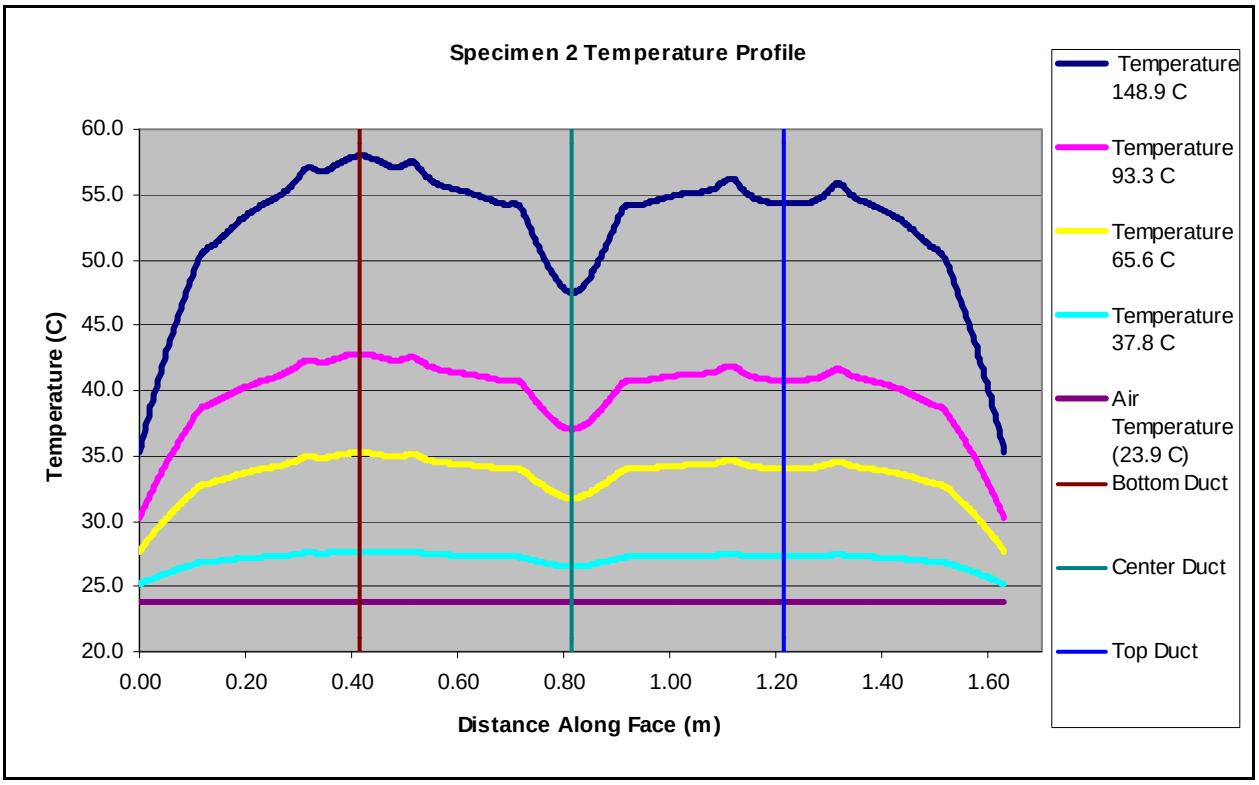


Figure 3.8 - Temperature profile along bottom surface
of Specimen 2 for various temperature loadings

Specimen 3 was 30 cm (12 in) thick was constructed with all steel ducts and did not contain any simulated voids inside the ducts. The main focus of this model was to distinguish the thermal differences achieved when the tendons were located at different depths of concrete cover in a 30 cm (12 in) thick concrete specimen. The top steel duct (located near the left edge of the specimen in Figure 3.9) contained 30 post-tensioning steel strands and had 10 cm (4 in) of concrete cover to the heated surface. The center steel duct contained 20 steel strands and had 7.5 cm (3 in) of concrete cover to the heated surface. The bottom steel duct (located near the right edge of the specimen in Figure 3.9) contained 30 steel strands and had 5 cm (2 in) of concrete cover. Figure 3.9 displays the temperature distribution throughout the cross-section of Specimen 3 for a 93.3°C (200°F) applied temperature loading.

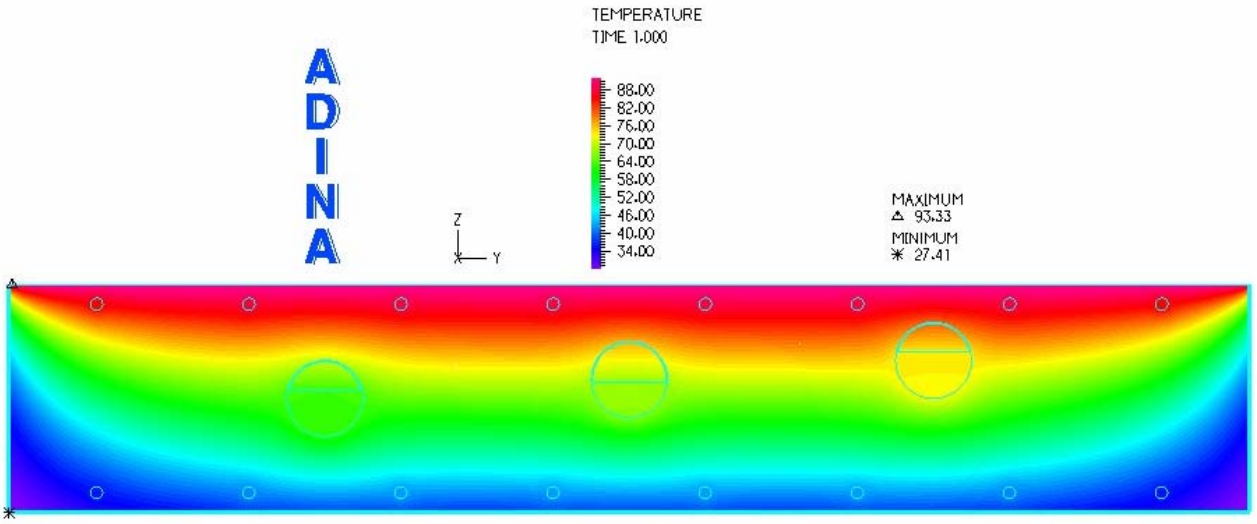


Figure 3.9 - Temperature distribution throughout Specimen 3
with a 93.3°C (200°F) temperature loading from ADINA

After analyzing the finite element model for Specimen 3, the thermal trends were similar to the 20 cm (8 in) thick specimens. It was ascertained that the top and bottom ducts that contained 30 post-tensioning steel strands were the most efficient in transferring heat through the cross-section of the specimen. The locations of the three tendons should appear warmer than the surrounding concrete on the unheated surface because each of the tendons were constructed with large amounts of post-tensioning steel and steel ducts.

The most obvious points obtained from the temperature profile of Specimen 3 is that cooling from the convection loading along the three edges has a larger impact on the temperature distribution throughout specimen than observed in the 20 cm (8 in) thick specimens. A temperature gradient through the thickness of the specimen greater than 70°C (126°F) is required to detect the locations of the tendons. Since the specimen was 10 cm (4 in) thicker than the two specimens discussed previously, the volume of concrete being heated is much larger. An applied temperature loading of 148.9°C (300°F) is required to obtain a 2°C (3.6°F) temperature difference at locations where the ducts were present. This temperature difference would be

sufficient to detect the locations of the tendons with the thermal camera. The depth of cover appears to play a role in transferring thermal energy through the specimen. The top and bottom tendons both contain the same amount of steel, but are located at different depths of cover in the specimen. The bottom tendon was located closer to the heated surface than the top tendon. Therefore, the bottom tendon should appear colder on the unheated surface than the top tendon located directly in the center of the specimen according to the finite element model. It was assumed that this was due to the larger amount of concrete the thermal energy dissipated into. Figure 3.10 is a temperature profile plot with respect to position along the bottom surface of the model for five different temperature loadings for Specimen 3.

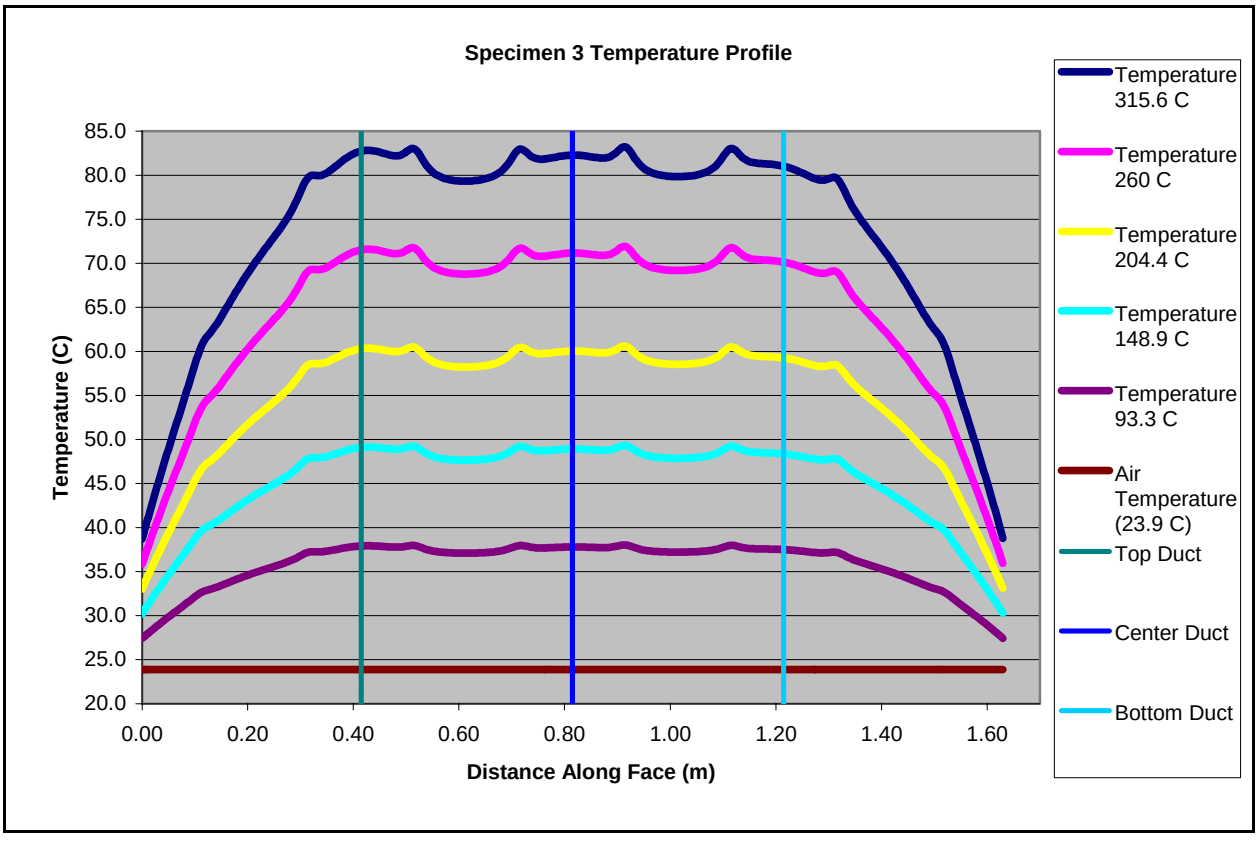


Figure 3.10 - Temperature profile along bottom surface of Specimen 3 for various temperature loadings

Specimen 4 was 30 cm (12 in) thick and contained both steel and HDPE ducts. The top tendon (located near the right edge of the specimen in Figure 3.11) was constructed with the steel duct containing four post-tensioning steel strands, was the only tendon containing a simulated void. The bottom duct (located near the left edge of the specimen in Figure 3.11) containing 30 steel strands and top duct containing four steel strands were placed at depth of concrete cover of 10 cm (4 in). The center duct contained 20 post-tensioning steel strands and was shifted so the depth of cover was 7.5 cm (3 in) to the heated surface and 12.5 cm (5 in) to the unheated surface. Figure 3.11 displays the temperature distribution throughout the cross-section of Specimen 4 for a 93.3°C (200°F) applied temperature loading.

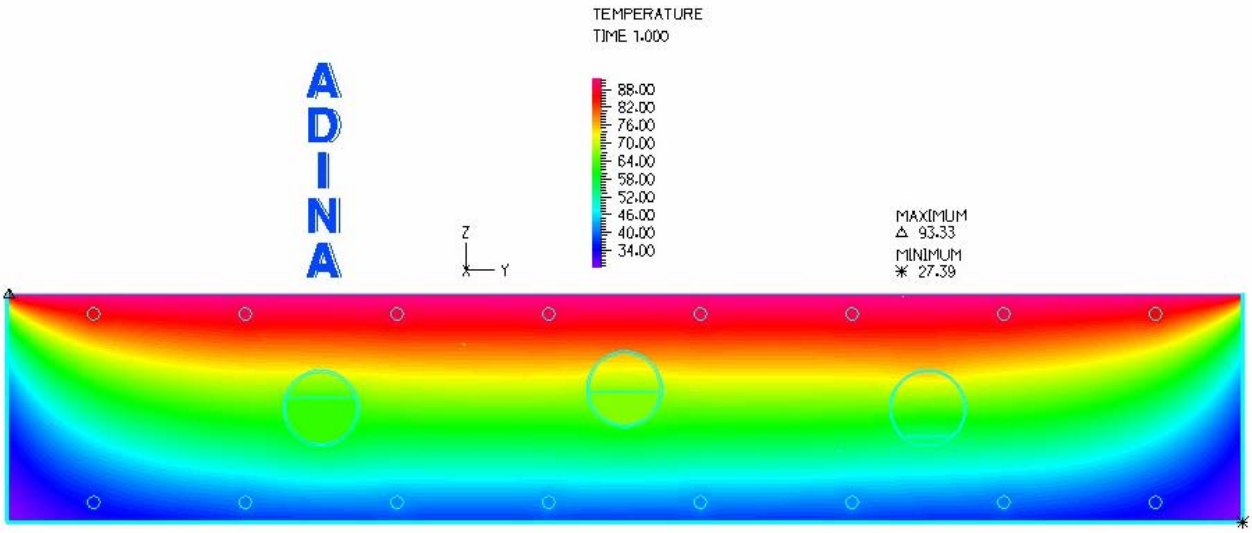


Figure 3.11 - Temperature distribution throughout Specimen 4
with a 93.3°C (200°F) temperature loading from ADINA

The bottom and center tendon were almost equal in transferring thermal energy through the cross-section even though the bottom duct contained 10 more steel strands than the center duct. This was due to convection cooling around the edges of the specimen reducing the

temperature of the bottom surface directly beneath the bottom tendon. The top tendon constructed with a steel duct containing four steel strands and a large simulated void should appear the coldest of the three tendons during experiment testing. The standard steel reinforcement would be visible using lower applied temperatures, but detecting the location of the tendons in Specimen 4 would require an applied temperature of at least 148.9°C (300°F). Figure 3.12 is a temperature profile plot with respect to position along the bottom surface of the model for five different temperature loadings for Specimen 4.

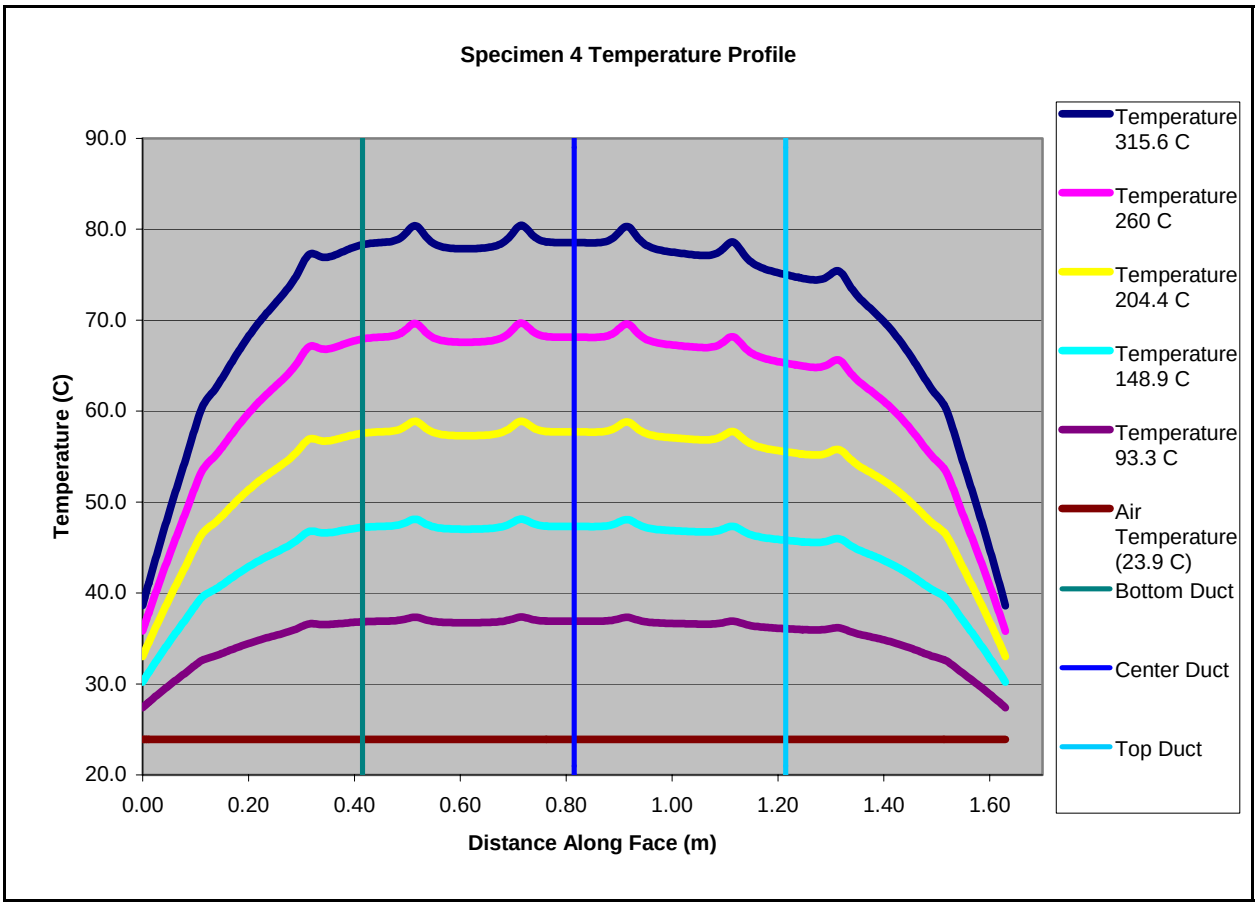


Figure 3.12 - Temperature profile along bottom surface
of Specimen 4 for various temperature loadings

Specimen 5 was also 40 cm (16 in) thick and was constructed with all steel ducts. The top tendon (located near the left edge of the specimen in Figure 3.13) contained 30 post-

tensioning steel strands. The bottom tendon (located near the right edge of the specimen in Figure 3.13) also contained 30 post-tensioning steel strands. The center tendon contained 20 steel strands. None of the ducts contained simulated voids. The focus of this model was to determine the effect varying concrete cover depths have on the temperature profile of a 40 cm (16 in) thick specimen. The top duct, center duct, and bottom duct had 15 cm (6 in), 12.5 cm (5 in), and 10 cm (4 in) of concrete cover to the heated surface, respectively. Figure 3.13 displays the temperature distribution throughout the cross-section of Specimen 5 for a 93.3°C (200°F) applied temperature loading.

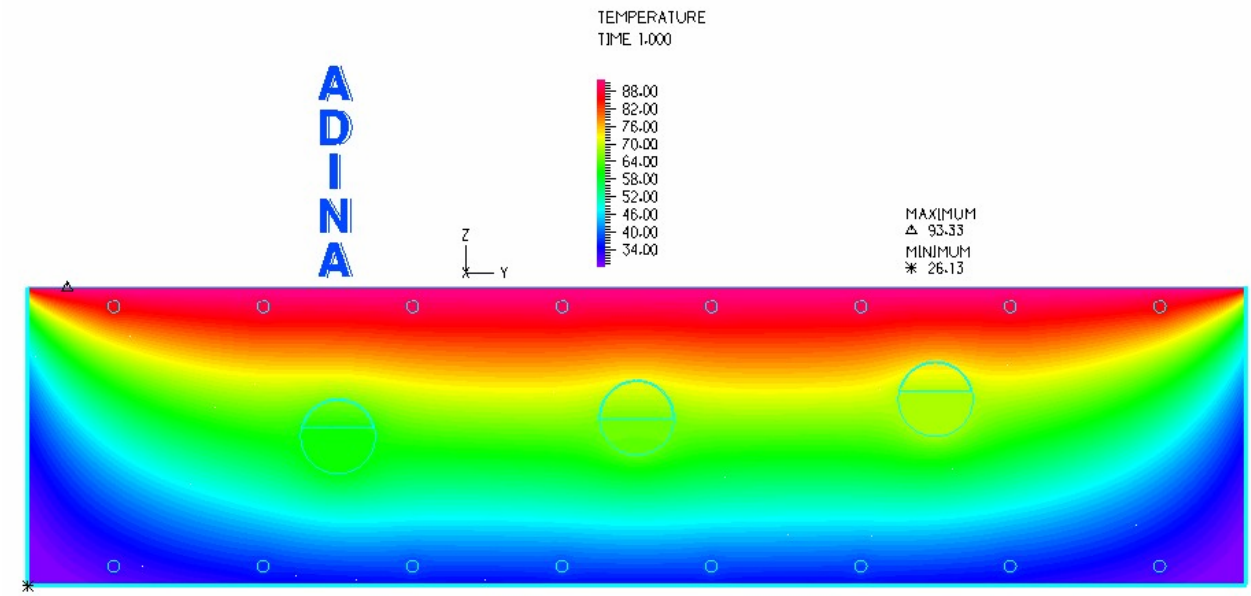


Figure 3.13 - Temperature distribution throughout Specimen 5
with a 93.3°C (200°F) temperature loading from ADINA

The results from the finite element model for Specimen 5 provided valuable results that helped determine which specimens to examine during the experimental testing phase of the research. The top and bottom tendons that contained 30 post-tensioning steel strands were predicted to appear the warmest, but were over 3°C (5.4°F) colder than the center tendon containing 20 steel strands. This was due to the large area of convection cooling occurring on

the unheated surfaces of the model. After viewing the temperature profile plot for Specimen 5, it can be seen that the convection loading dramatically alters the temperature along the bottom surface of the slab. There was approximately a 50°C (90°F) temperature difference between the left edge of the model and the location of the top tendon due to convection. This causes the temperature profile to be more parabolic than observed in the 20 cm (8 in) thick specimen temperature profiles. It was also determined that an applied temperature loading of 204.4°C (400°F) would be required to cause a temperature difference at the locations where the ducts were present to obtain meaningful results with the thermal camera.

The trends observed regarding depth of concrete cover in Specimen 3 were very similar to those observed in Specimen 5. The bottom tendon was located 5 cm (2 in) closer to the heated surface than the top, but each contains the same amount of post-tensioning steel. As seen in Specimen 3, the bottom tendon appeared the coldest because of the large concrete cover distance between the tendon and the unheated surface. This large volume of concrete allowed the thermal energy to dissipate throughout the cross-section as it flowed through the thickness of the specimen. Figure 3.14 is a temperature profile plot with respect to position along the bottom surface of the model for seven different temperature loadings for Specimen 5.

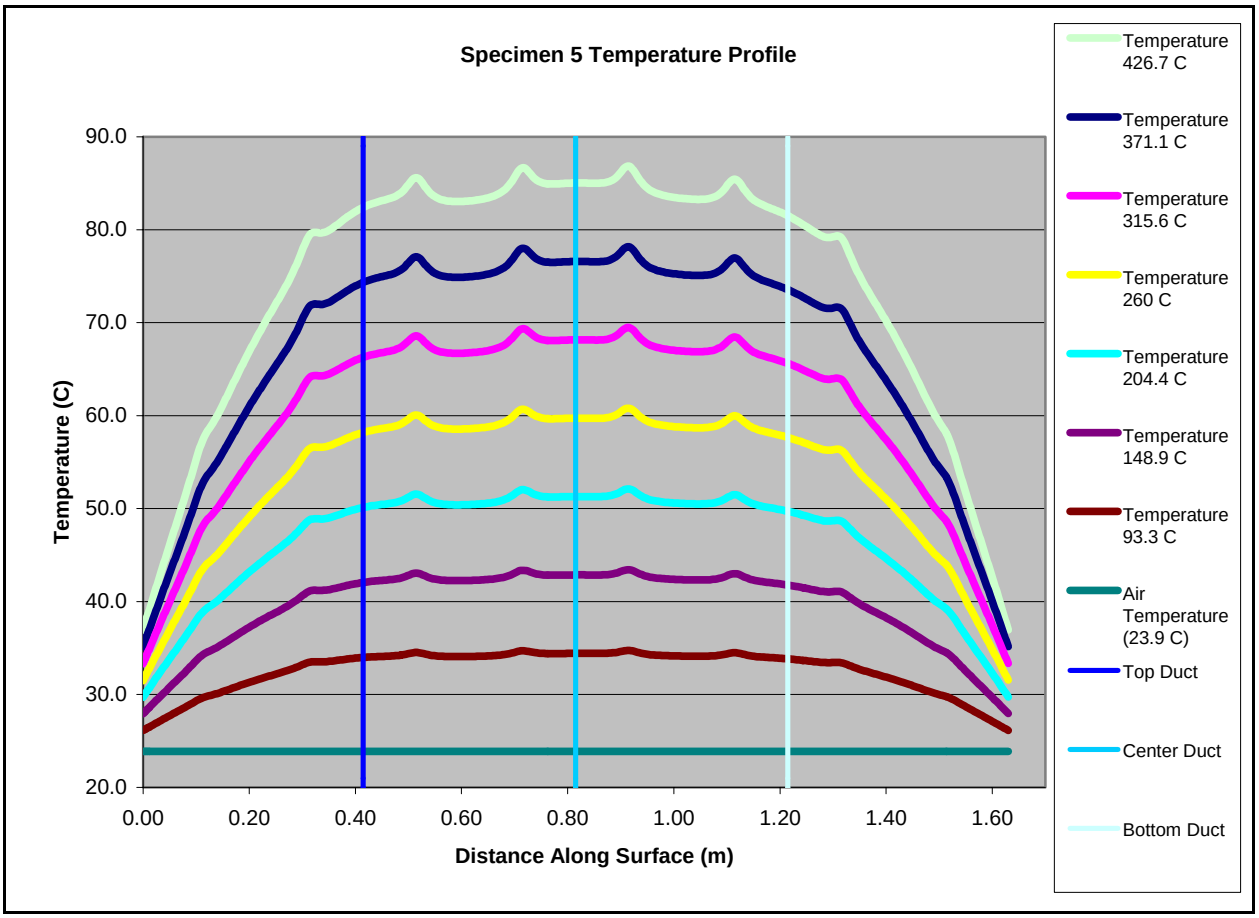


Figure 3.14 - Temperature profile along bottom surface
of Specimen 5 for various temperature loadings

Specimen 6 was 40 cm (16 in) thick and contained both steel and HDPE ducts. The bottom tendon (located near the right edge of the specimen in Figure 3.15) was constructed with a steel duct containing four post-tensioning steel strands, was the only tendon containing a simulated void. The top duct (located near the left edge of the specimen in Figure 3.15) contained 30 steel strands and bottom duct contained four steel strands placed at depth of concrete cover of 15 cm (6 in). The center duct containing 20 post-tensioning steel strands was shifted so the depth of cover was 12.5 cm (5 in) to the heated surface and 17.5 cm (7 in) to the unheated surface. Figure 3.15 displays the temperature distribution throughout the cross-section of Specimen 6 for a 93.3°C (200°F) applied temperature loading.

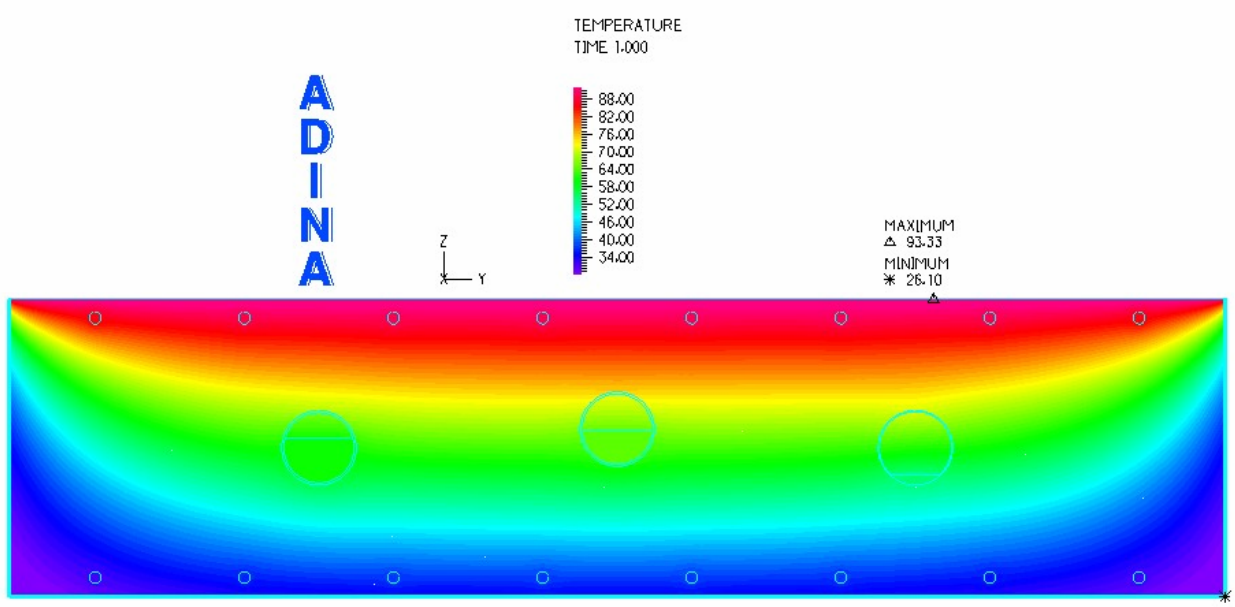


Figure 3.15 - Temperature distribution throughout Specimen 6
with a 93.3°C (200°F) temperature loading from ADINA

The results obtained from the finite element model of Specimen 6 indicated that the convection cooling around the edges of the specimen would make distinguishing locations of tendons and simulated voids near the unheated edges difficult at best. The top and bottom tendons appeared to transfer equal amounts of thermal energy through the cross-section even though the top duct contained 26 more steel strands than the bottom duct. The large change in temperature on the unheated surface near the edge of the specimen would mask any minute temperature changes caused by simulated voids embedded in the ducts. In a thermal image, it would be difficult to distinguish between the tendon containing 30 post-tensioning steel strands and the tendon containing just four strands with a 15 cm (6 in) long by 8.5 cm (3.3 in) thick simulated void. In the scenario modeled, the center tendon with only 20 steel strands appeared warmer than the top tendon containing 30 steel strands. These false temperature readings during inspection could be more detrimental than beneficial.

According to the finite element models, detecting the tendons in a 40 cm (16 in) thick specimen would require an applied temperature of at least 260.0°C (500°F) or a temperature gradient through the thickness of the specimen of 236°C (425°F). Figure 3.16 is a temperature profile plot with respect to position along the bottom surface of the model for seven different temperature loadings for Specimen 6.

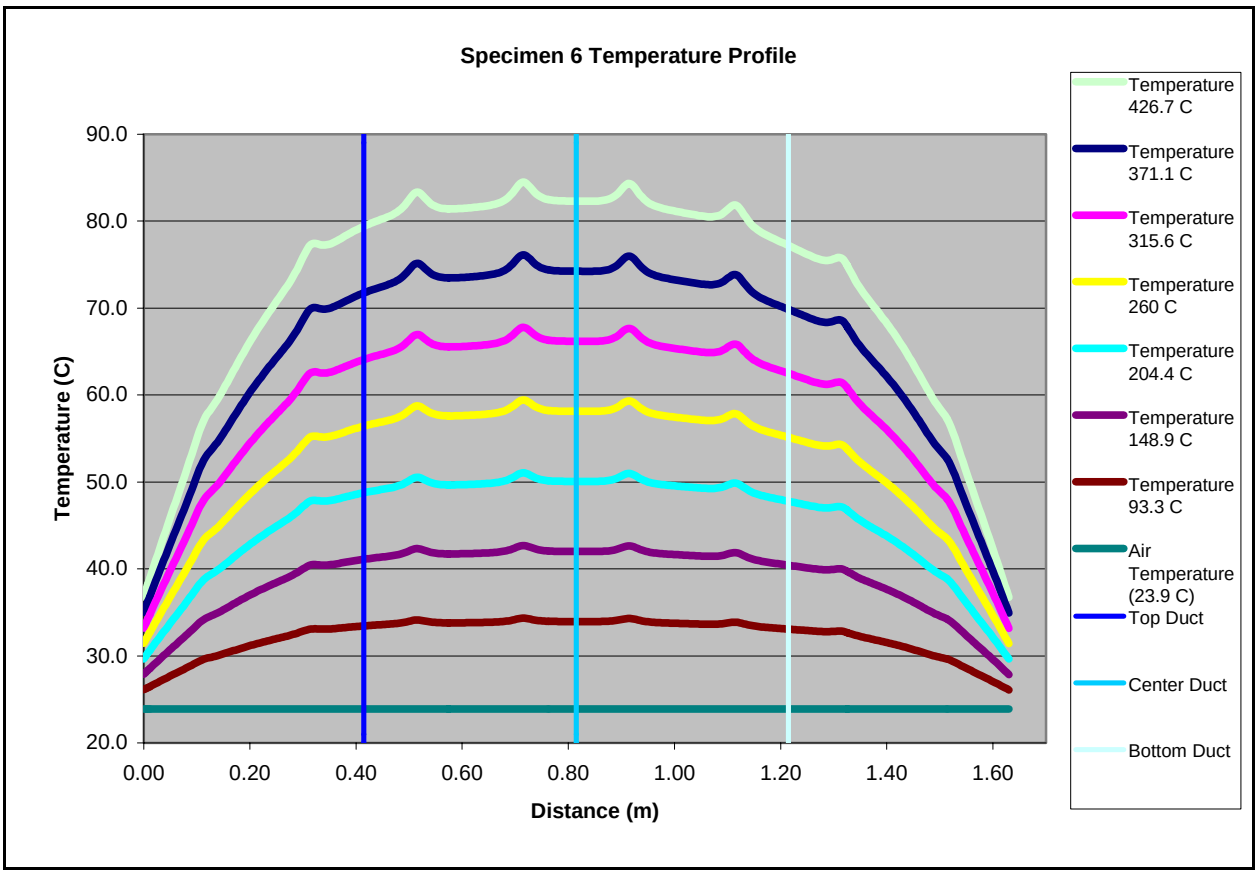


Figure 3.16 - Temperature profile along bottom surface
of Specimen 6 for various temperature loadings

Specimen 7 was 20 cm (8 in) thick and contained all HDPE ducts with only the center duct containing simulated voids. Each of the ducts contained 20 post-tensioning steel strands. One simulated void 5.2 cm (2.1 in) thick by 5 cm (2 in) long and another simulated void 5.2 cm (2.1 in) thick by 10 cm (4 in) long were placed over the post-tensioning steel strands in the center

duct. The simulated voids were located approximately 35 cm (14 in) from each end of the duct. Since the model is only two-dimensional, both voids could not be accounted for. Since a slice through the cross-section of the specimen was modeled, the model was developed slicing through the specimen at the location of one of the voids. This specimen also contained corroded post-tensioning steel in the bottom duct (located near the right edge of the specimen in Figure 3.17). Since thermal properties for corroded steel strands versus non-corroded steel strands were not available, the corrosion on the steel was not accounted for in the finite element model. The depth of concrete cover to each of the tendons was 5 cm (2 in). Figure 3.17 displays the temperature distribution throughout the cross-section of Specimen 7 for a 93.3°C (200°F) applied temperature loading.

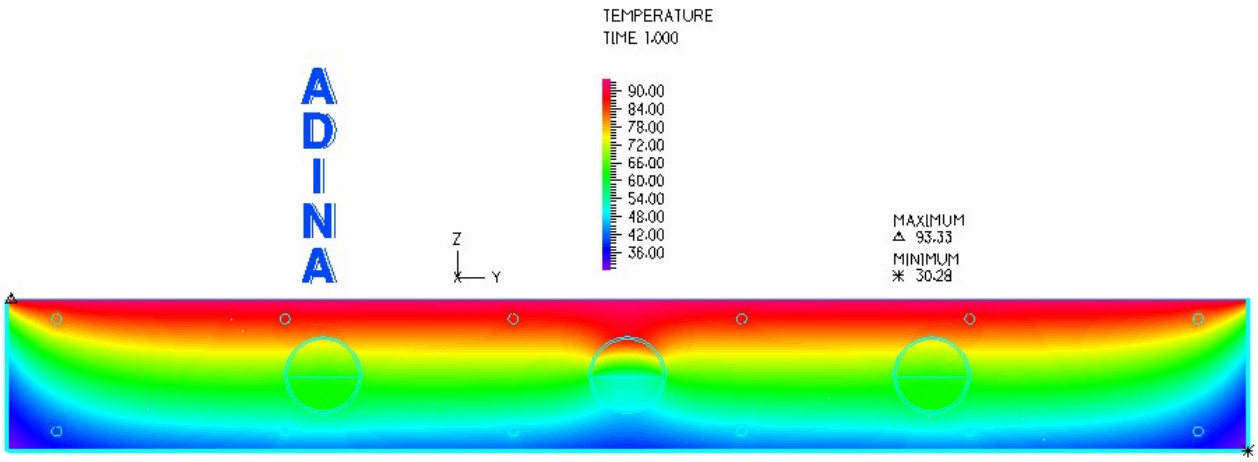


Figure 3.17 - Temperature distribution throughout Specimen 7
with a 93.3°C (200°F) temperature loading from ADINA

It was determined from the results obtained from the finite element model of Specimen 7, that the center tendon was the least efficient in transferring thermal energy through the cross-section of the specimen. This was because only the center tendon contained a simulated void. Therefore, the center tendon should appear the coldest when a thermal image is taken of the unheated surface. The temperature profile beneath the top tendon (located near the left edge of

the specimen in Figure 3.17) and bottom tendon (located near the right edge of the specimen in Figure 3.17) was the same since each tendon contained the same amount of steel and were located at the same concrete cover depth.

As seen in the previous two 20 cm (8 in) thick specimens, temperature gradients larger than 15°C (27°F) should produce detectable temperature differences with the thermal camera. From Figure 3.18, it can be seen that an applied temperature of 93.3°C (200°F) results in approximately a 5°C (9°F) temperature difference between the location of the center tendon with the simulated void and the top and bottom tendons.

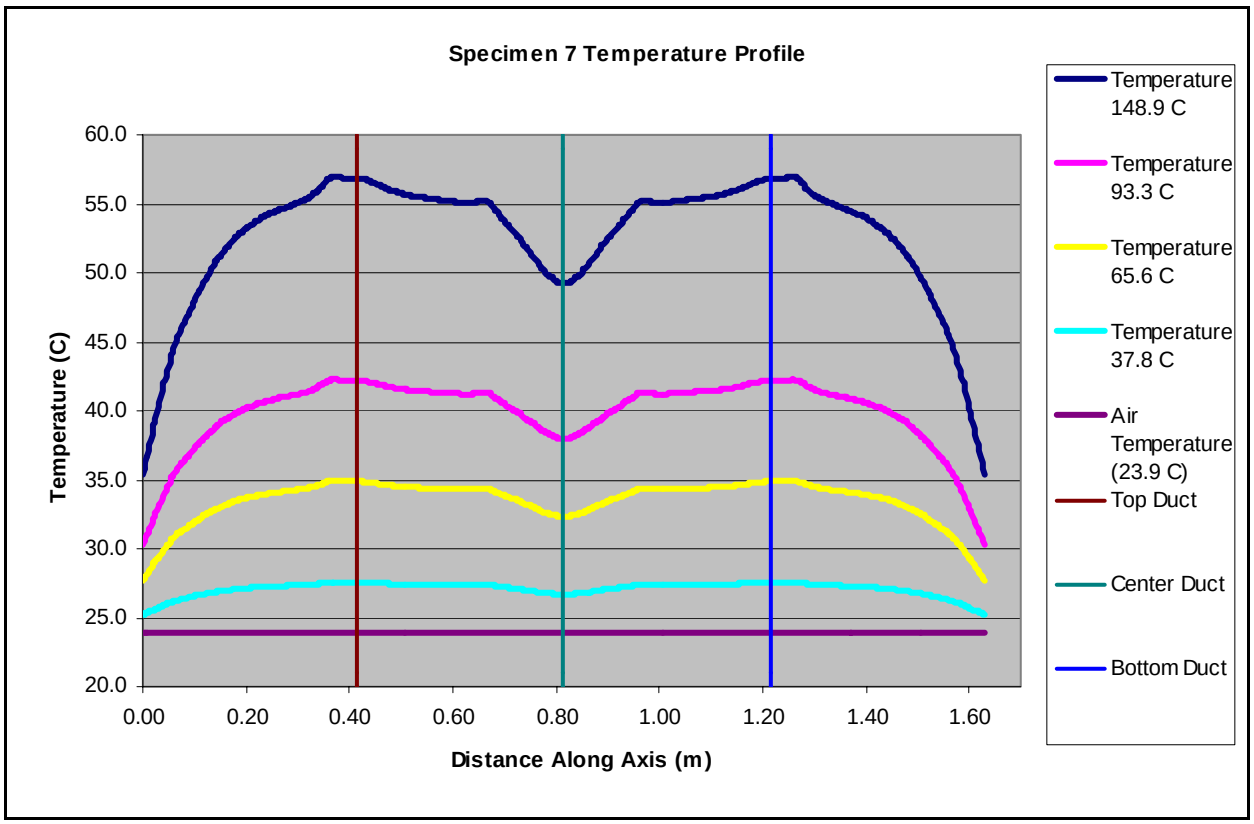


Figure 3.18 - Temperature profile along bottom surface
of Specimen 7 for various temperature loadings

Specimen 8 was 30 cm (12 in) thick and contained two tendons embedded with a 5.2 cm (2.1 in) thick by 5 cm (2 in) simulated void and another simulated void 5.2 cm (2.1 in) thick by

10 cm (4 in) long inside the HDPE ducts. The top duct (located near the left edge of the specimen in Figure 3.19) and the center duct each contained 20 post-tensioning steel strands and the bottom duct (located near the edge of the specimen in Figure 3.19) contained 30 steel strands. The center tendon with 20 steel strands and the bottom tendon with the 30 steel strands both contained the simulated voids. Each of the tendons were located directly at mid-depth in the specimen and had 10 cm (4 in) of concrete cover to each surface. Figure 3.19 displays the temperature distribution throughout the cross-section of Specimen 8 for a 93.3°C (200°F) applied temperature loading.

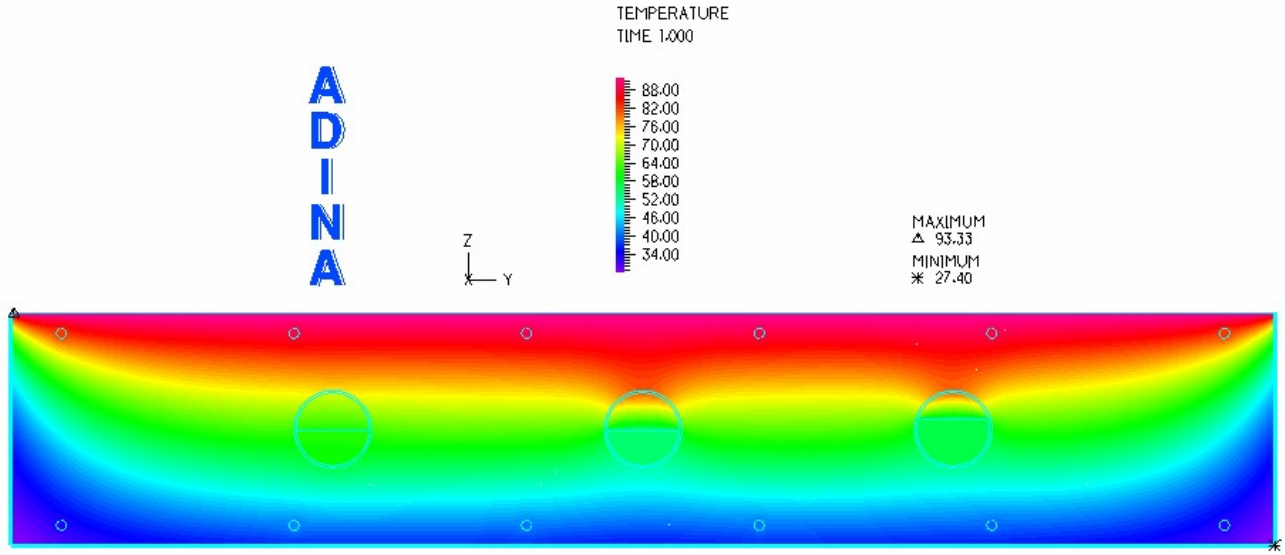


Figure 3.19 - Temperature distribution throughout Specimen 8
with a 93.3°C (200°F) temperature loading from ADINA

The results from the modeling showed the top tendon containing 20 post-tensioning steel strands without simulated voids was the most efficient in transferring thermal energy. The bottom tendon containing 30 steel strands and simulated voids actually appeared the coolest. Heat transfer theory would predict that the center tendon would appear the coldest of the three tendons, because of the low thermal conductivity of that tendon. This was not the case according to the finite element model. This can be attributed to the convection cooling occurring around

the edges of the specimen, thereby reducing the temperature of the bottom surface directly beneath the tendon.

The temperature profile for Specimen 8 also shows a temperature gradient larger than 125°C (225°F) would be required to achieve temperature differences detectable with the thermal camera on the unheated surface. The standard steel reinforcement would be visible using lower applied temperatures, but detecting the location of the tendons in the specimen would require an applied temperature of at least 148.9°C (300°F). Figure 3.20 is a temperature profile plot with respect to position along the bottom surface of the model for five different temperature loadings for Specimen 8.

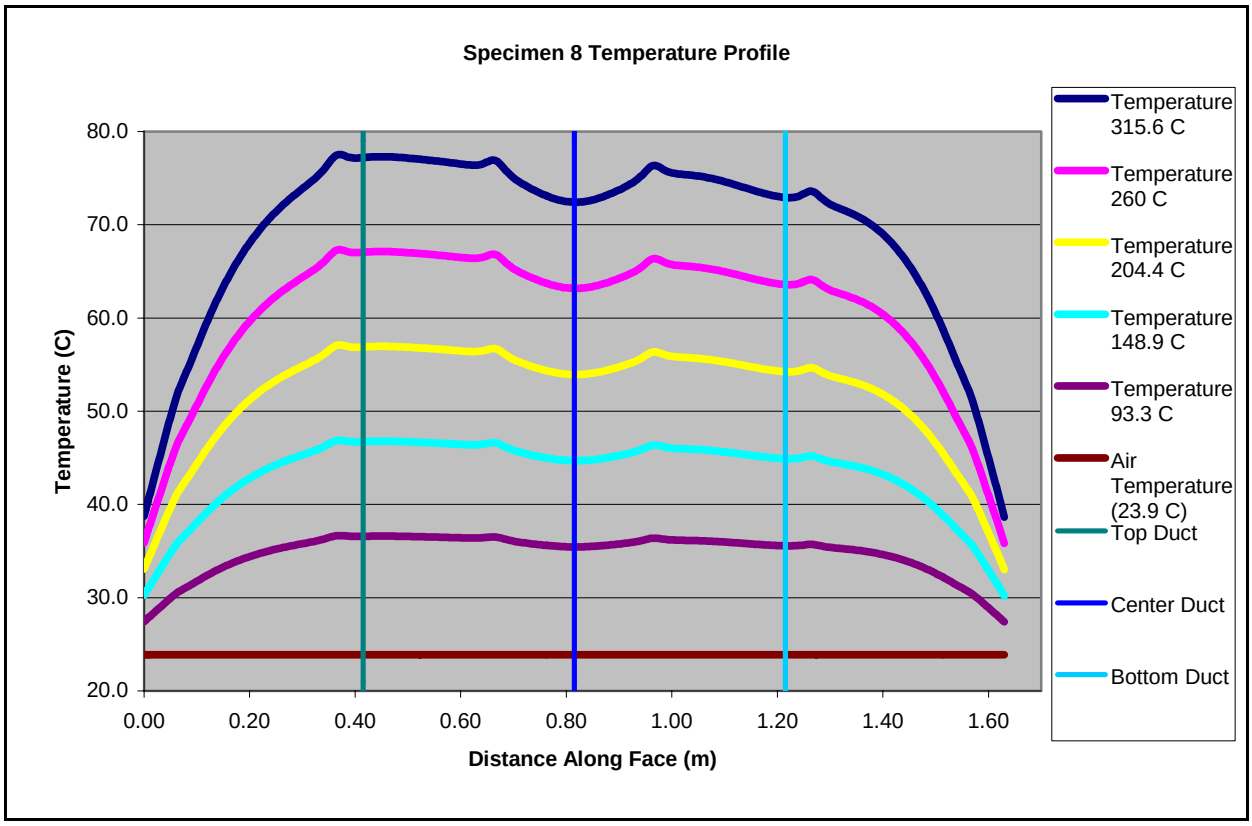


Figure 3.20 - Temperature profile along bottom surface of Specimen 8 for various temperature loadings

### 3.4 – Insulated Boundary Conditions

After the models without insulated boundary conditions were created and analyzed, it was quite obvious that the effects of convection cooling on the unheated edges of the specimen would be significant. Based on the temperature plots in Figures 3.14 and 3.16, it became quite obvious that the temperature variations on the specimen surface cause by simulated voids inside the HDPE or steel ducts would be masked by the large decreases in temperature near the edges of the specimens. Additionally, the slabs developed by Pearson (2003) and Conner (2004) did not exactly replicate a standard bridge wall. Bridge walls are continuous and would not have convection cooling at the specimen edge.

Therefore, the boundary elements along the narrow edges of the specimens were modeled as insulated boundary conditions without applied convection loadings. The unheated surface was still modeled with a convection loading. This insulated boundary edges would act similarly to a continuous wall in a box girder bridge. Only the results obtained for Specimen 4 and Specimen 6 were discussed and compared since the improvements gained from the insulated models were similar for all of the models developed. Additionally, the improvements from insulating the edges of the model were more significant on the thicker models. Specimen 4 was chosen because of the three different amounts of steel and two different duct materials used in just one specimen. One of the main points observed from the results of the uninsulated model of Specimen 4 was that the duct containing 30 post-tensioning steel strands exhibited approximately the same temperature as the center duct containing only 20 steel strands.

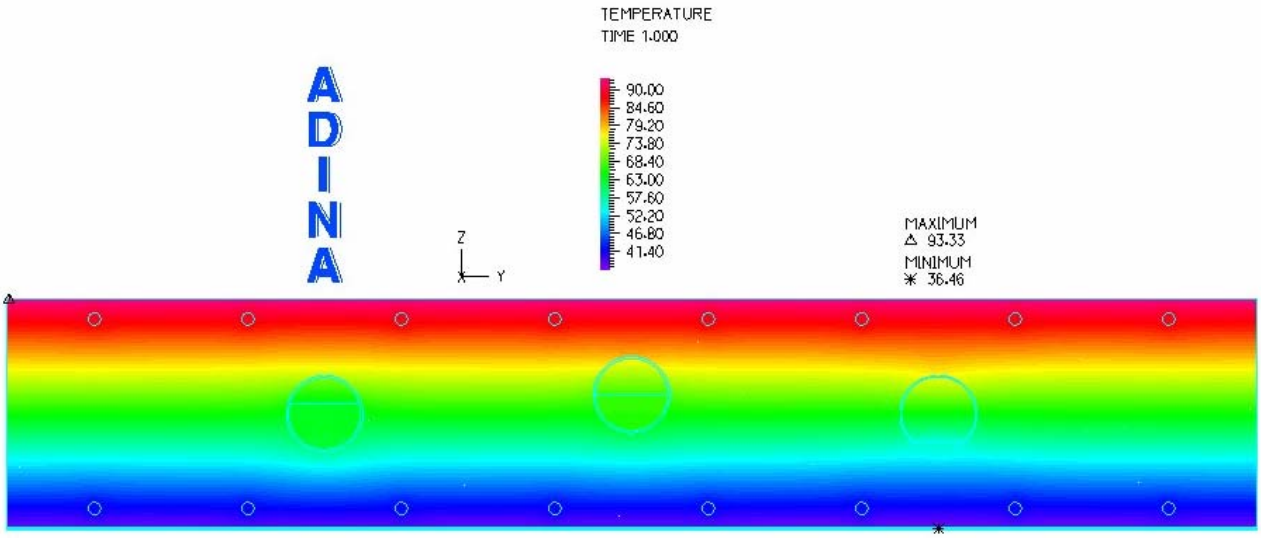


Figure 3.21 - Temperature distribution throughout Specimen 4 with a 93.3°C (200°F) temperature loading with insulated edge elements

Figure 3.21 is the resultant temperature distribution from ADINA for Specimen 4 modeled with insulated boundary edges and a 93.3°C (200°F) applied temperature loading. This model was analyzed with five different applied temperature loadings. After the results from each of these models were obtained, the temperature profiles along the unheated surface of the model were plotted. Additionally, the uninsulated temperature profile for Specimen 4 with the applied temperature loading of 93.3°C (200°F) was plotted as a comparison to the insulated results. Figure 3.22 displays the temperature profiles with respect to position along the bottom surface of the model for five different temperature loadings for Specimen 4.

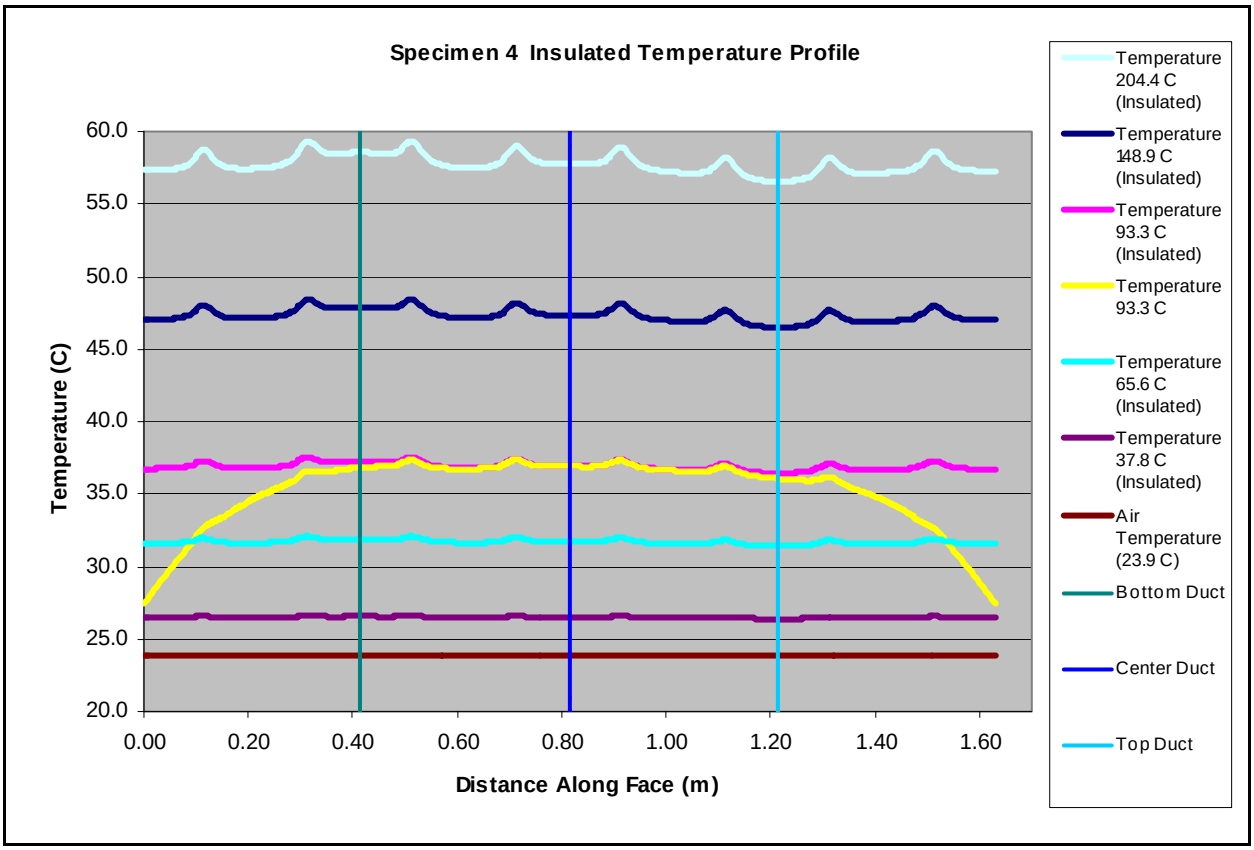


Figure 3.22 - Insulated temperature profile along bottom surface of Specimen 4 for various temperature loadings

From Figure 3.22, it can easily be seen that insulating the edges across the thickness of the model has a dramatic effect on the temperature profile for the tendons near the edges of the specimen. By insulating the boundary edges, the bottom tendon would appear warmer than the center tendon containing fewer steel strands. It was also noted that insulating the two edges did not have a noticeable effect on the temperature profile between the two outside ducts. Insulating the edges of the specimen raised the temperature along the bottom surface of the model to a more uniform value. This could be beneficial when using a thermal camera to detect temperature variations due to discontinuities in the ducts.

Specimen 6 was 10 cm (4 in) thicker than Specimen 4, providing 5 cm (2 in) more concrete cover to each tendon. This increased thickness had a substantial impact on the

temperature profile along the surface of the specimen. Figure 3.23 is the resultant temperature distribution from ADINA for Specimen 6 modeled with insulated boundary edges and a 93.3°C (200°F) applied temperature loading.

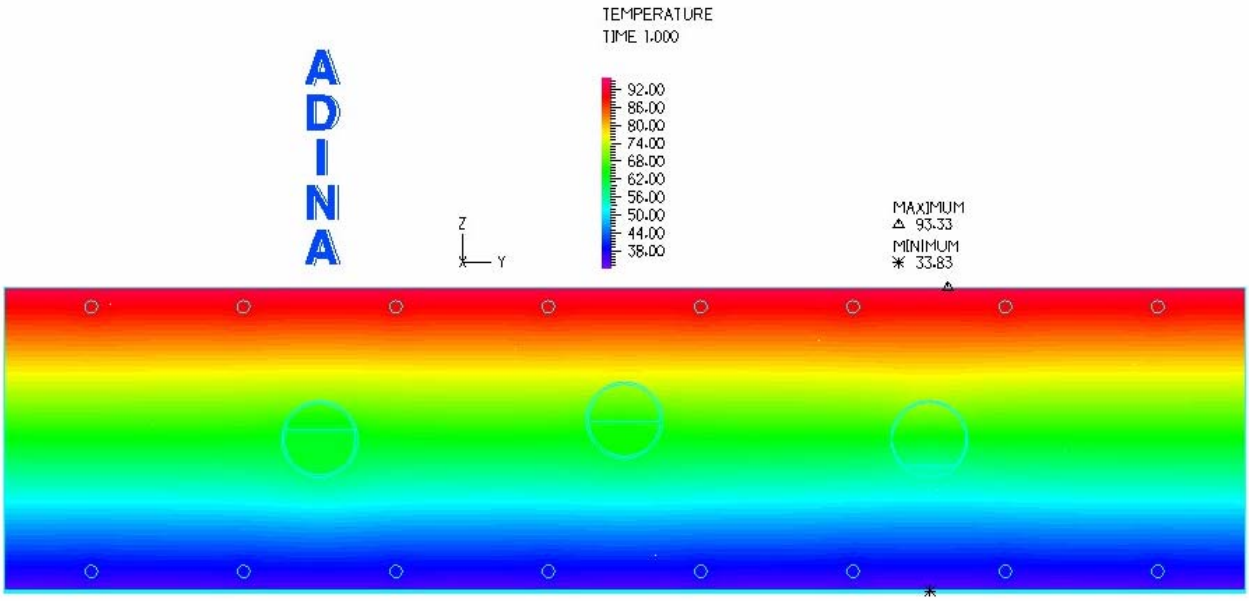


Figure 3.23 - Temperature distribution throughout Specimen 6 with a 93.3°C (200°F) temperature loading with insulated edge elements

Figure 3.24 displays the temperature profiles with respect to position along the unheated surface of the model for five different temperature loadings for Specimen 6. Insulating the edges across the thickness of the model helped create a more uniform temperature distribution. In Specimen 6, it was observed that the duct containing 30 post-tensioning steel strands appeared cooler than the center duct containing only 20 steel strands when modeled without insulated boundary conditions. Comparisons were conducted between the temperature profiles from the insulated and uninsulated finite element models. As expected, the top duct containing 30 steel strands in the insulated model appeared warmer than the center duct containing 20 steel strands. This was attributed to the larger amount of steel strands embedded in the top duct increasing the

flow of thermal energy through the specimen at that location, which increased the unheated surface temperature.

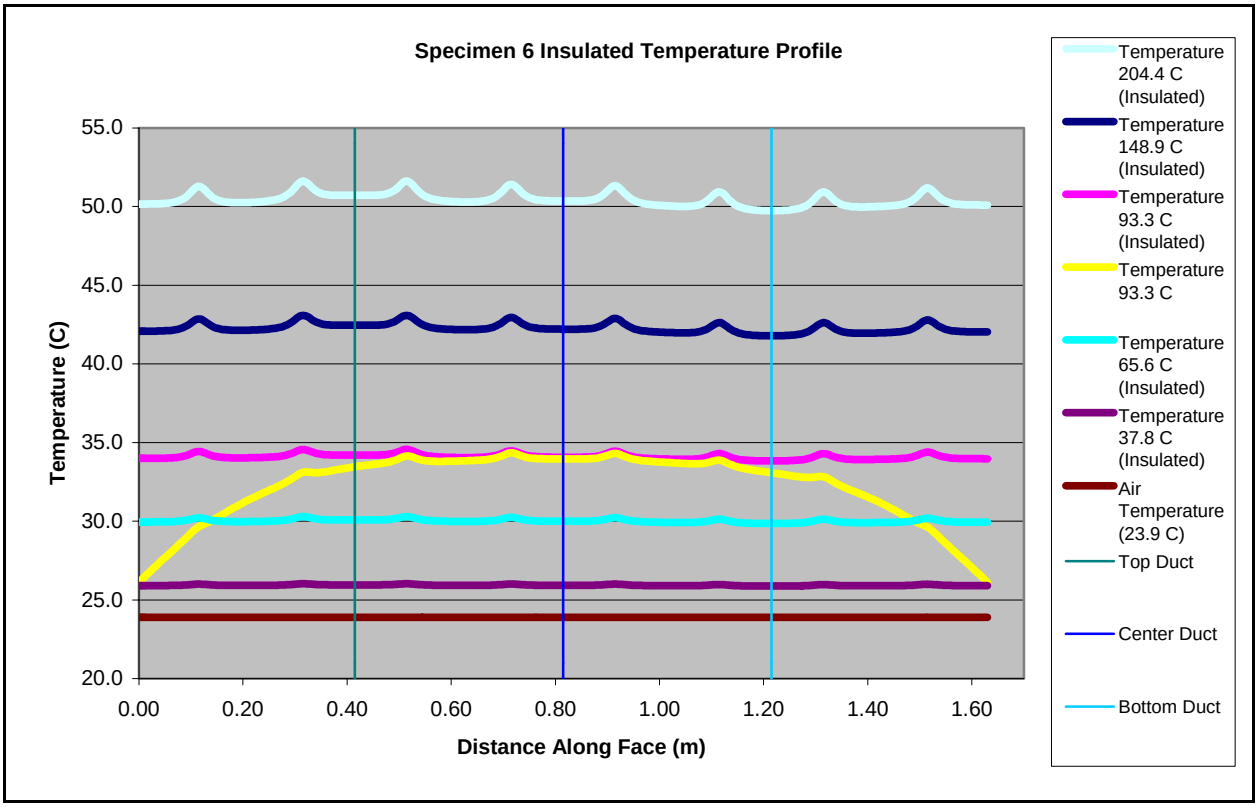


Figure 3.24 - Insulated temperature profile along bottom surface of Specimen 6 for various temperature loadings

### 3.5 – Baseline Comparisons

After completing the models for both insulated and uninsulated boundary conditions for each specimen, six additional baseline models were developed for the specimens containing simulated voids. The baseline models assumed no voids were present in any ducts and results were compared to the results obtained from the models containing voids. The resulting plots showed the temperature changes caused by the various simulated voids in each specimen. Each comparison was conducted using the 93.3°C (200°F) applied temperature loadings.

Specimen 1 contained one simulated void in the steel duct with 30 post-tensioning steel strands. Figure 3.25 is a baseline temperature comparison for Specimen 1 with an applied temperature loading of 93.3°C (200°F). The simulated void reduced the temperature profile by approximately 2°C (3.6°F). This difference in temperature would be substantial enough to be detected with a thermal camera.

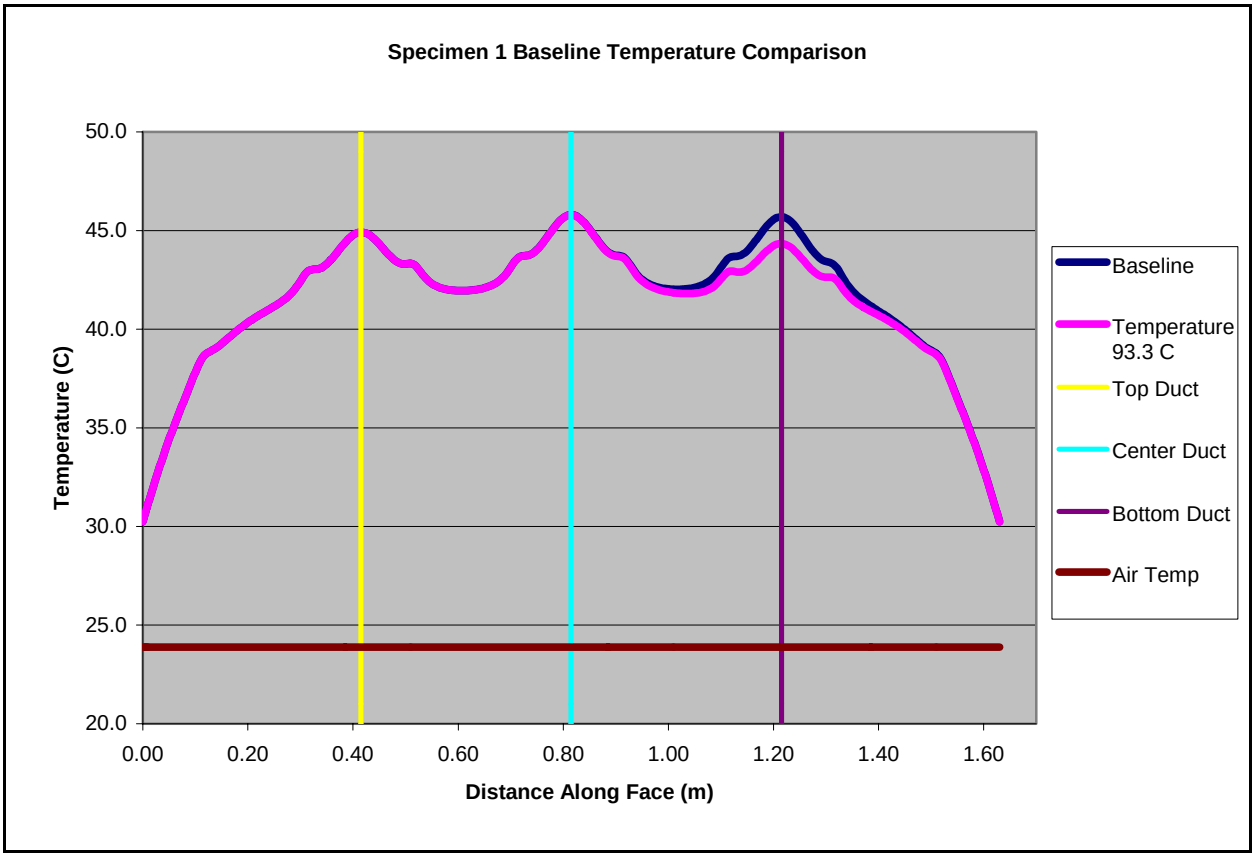


Figure 3.25 – Baseline temperature comparison for Specimen 1

Specimen 2 contained two simulated voids, one located in the center HDPE duct and the other in the top steel duct. Both ducts contained only four post-tensioning steel strands with a large simulated void. Figure 3.26 is a baseline temperature comparison for Specimen 2 with an applied temperature loading of 93.3°C (200°F). The simulated void in the top duct reduced the

temperature profile beneath the tendon by approximately 3°C (5.4°F). The simulated void in the center HDPE duct caused a 4°C (7.2°F) reduction in the temperature profile. This larger difference in temperature observed at the location of the center HDPE duct compared to the steel duct is due to the lower thermal conductivity of the HDPE duct.

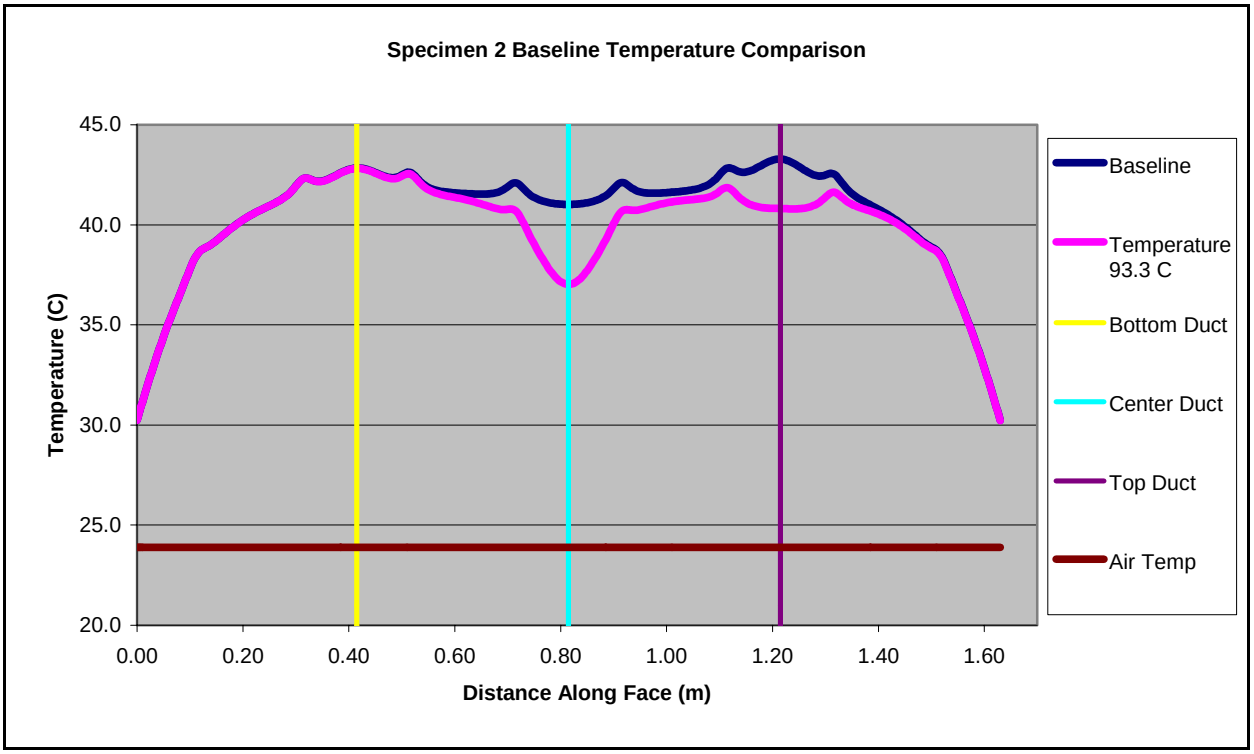


Figure 3.26 – Baseline temperature comparison for Specimen 2

Specimen 4 was 30 cm (12 in) thick and contained one simulated void located in the top steel duct, with only four post-tensioning steel strands. Figure 3.27 is a baseline temperature comparison for Specimen 4 with an applied temperature loading of 93.3°C (200°F). Specimen 4 was 10 cm (4 in) thicker than Specimen 2, and thus had a different baseline temperature profile. The simulated void in the top steel duct reduced the temperature profile beneath the tendon by only 1°C (1.8°F). Thus, the effect the simulated void on the temperature profile for the 30 cm

(12 in) thick specimen is less than the effect of an identical simulated void in a 20 cm (8 in) thick specimen.

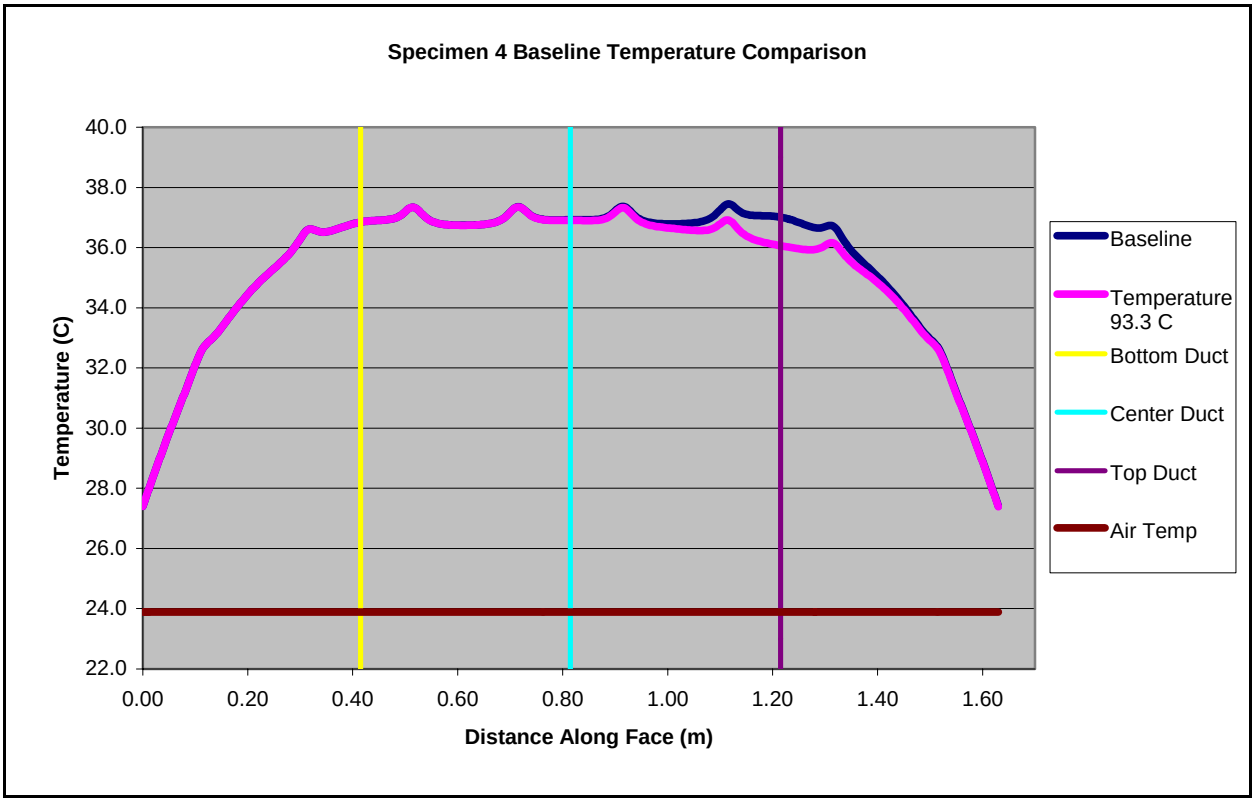


Figure 3.27 – Baseline temperature comparison for Specimen 4

Specimen 6 was 40 cm (16 in) thick and had an internal tendon layout identical to the tendon layout in Specimen 4. The main reason for analyzing this model was to determine the effect of an additional concrete thickness of 10 cm (4 in) on the temperature profile. Figure 3.28 is a baseline temperature comparison for Specimen 6 with an applied temperature loading of 93.3°C (200°F). The simulated void in the bottom steel duct altered the temperature profile beneath the tendon only 0.5°C (0.9°F) in Specimen 6. Based on comparisons of temperature profiles from Specimen 2, Specimen 4, and Specimen 6, it is apparent that greater concrete thickness reduced the change in surface temperature caused by a simulated void.

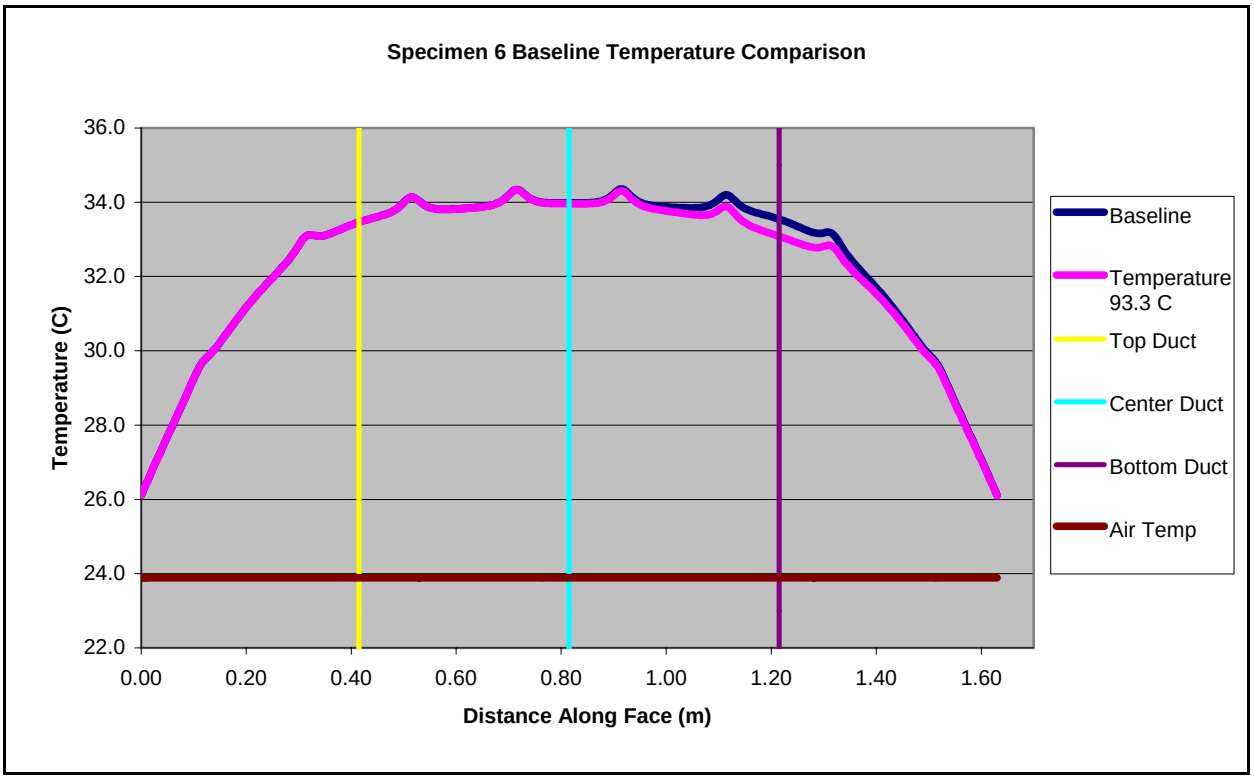


Figure 3.28 – Baseline temperature comparison for Specimen 6

Specimen 7 was 20 cm (8 in) thick and contained two simulated voids located in the center HDPE duct. The difference between this model and the other 20 cm (8 in) thick specimens is that the center HDPE duct contained 20 post-tensioning steel strands with a simulated void instead of four steel strands. The simulated void in the center HDPE duct altered the temperature profile beneath the tendon by approximately 2°C (3.6°F). This is smaller than the change in temperature profile for Specimen 2 with the center HDPE duct containing four steel strands and a simulated void. Figure 3.29 is a baseline temperature comparison for Specimen 7 with an applied temperature loading of 93.3°C (200°F).

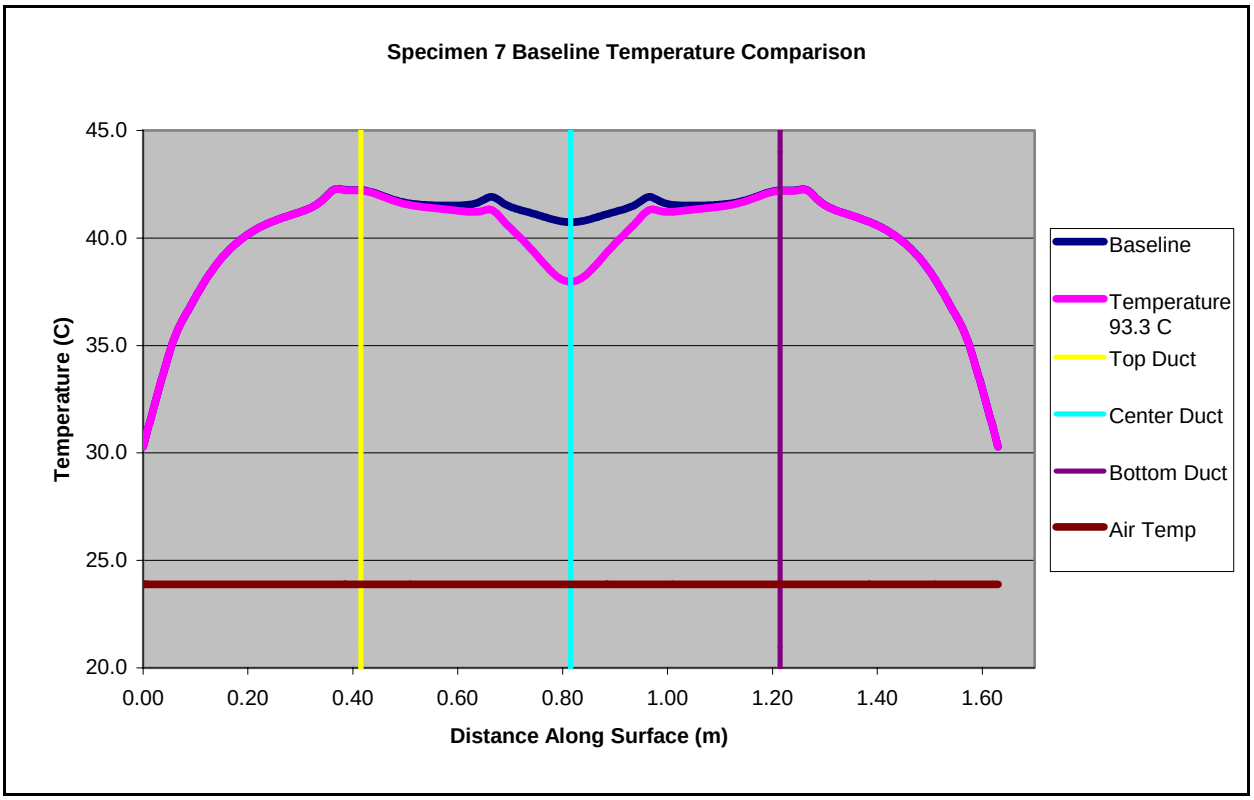


Figure 3.29 – Baseline temperature comparison for Specimen 7

Specimen 8 was constructed with two simulated voids, one located in the center HDPE duct and the other in the bottom HDPE duct. The center duct and the bottom duct each contained two simulated voids. The center duct contained 20 post-tensioning steel strands and the bottom duct contained 30 steel strands. Figure 3.30 is a baseline temperature comparison for Specimen 8 with an applied temperature loading of 93.3°C (200°F). The simulated void in the center duct altered the temperature profile beneath the tendon by approximately 1.6°C (2.9°F). This is a smaller temperature difference than observed in the 20 cm (8 in) thick Specimen 7. The simulated void in the bottom HDPE duct caused a 1.3°C (2.4°F) temperature change in the profile.

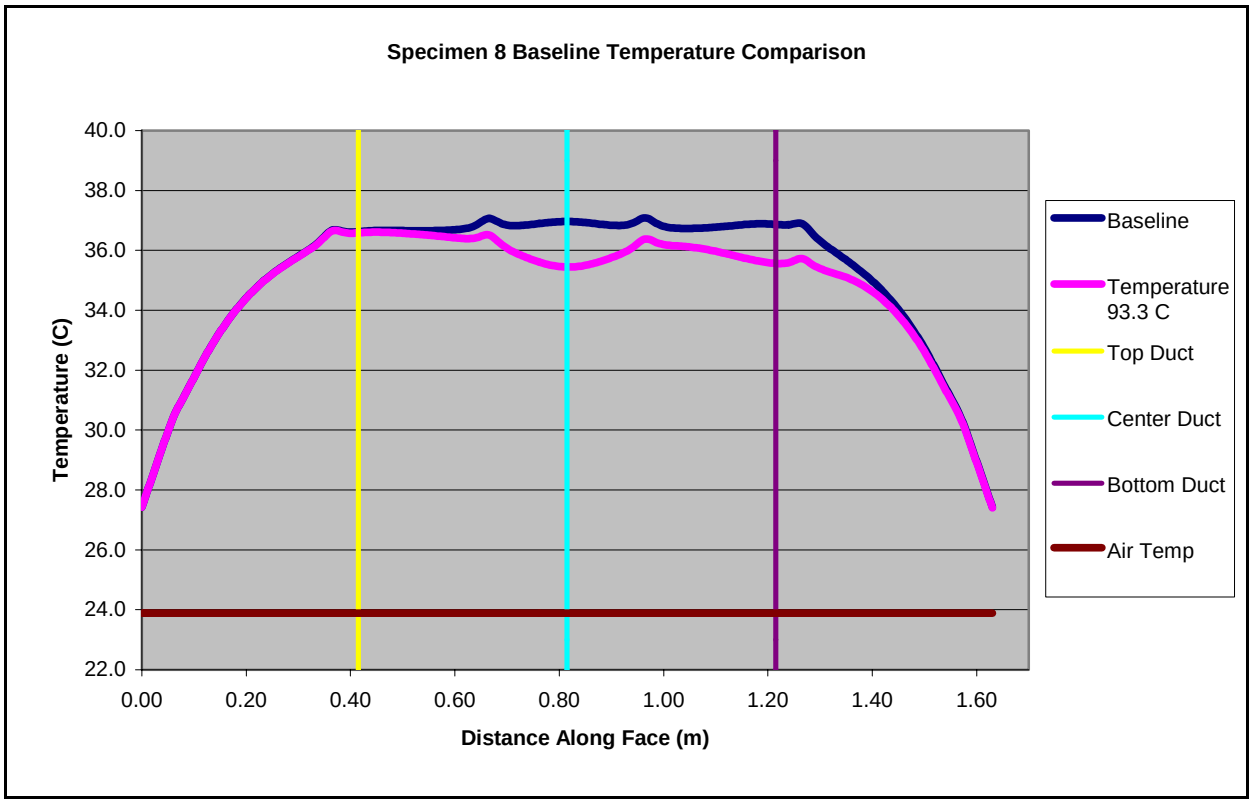


Figure 3.30 – Baseline temperature comparison for Specimen 8

## 3.6 – Trend Comparisons with Previous Research

The results attained from the finite element modeling were compared to the thermal images obtained by Pearson (2003) for Specimen 1 and Specimen 2. For Specimen 1, the uninsulated model predicted that the location of all three tendons should appear warmer than the surrounding concrete on the unheated face of the specimen. Therefore, the location of the tendons should appear cooler than the surrounding concrete on the heated face of the specimen. This can be attributed to high thermal conductivity of post-tensioning steel strands embedded inside steel ducts, increasing the amount of thermal energy flowing through the specimen at that location. The thermal images obtained by Pearson (2003) for Specimen 1 illustrated the basic trends predicted by the finite element model. Figure 3.31 is an exterior image showing the

heated surfaces of Specimen 3 and Specimen 1. The dark temperature regions that appear on the surface of Specimen 1 indicate the location of each tendon.

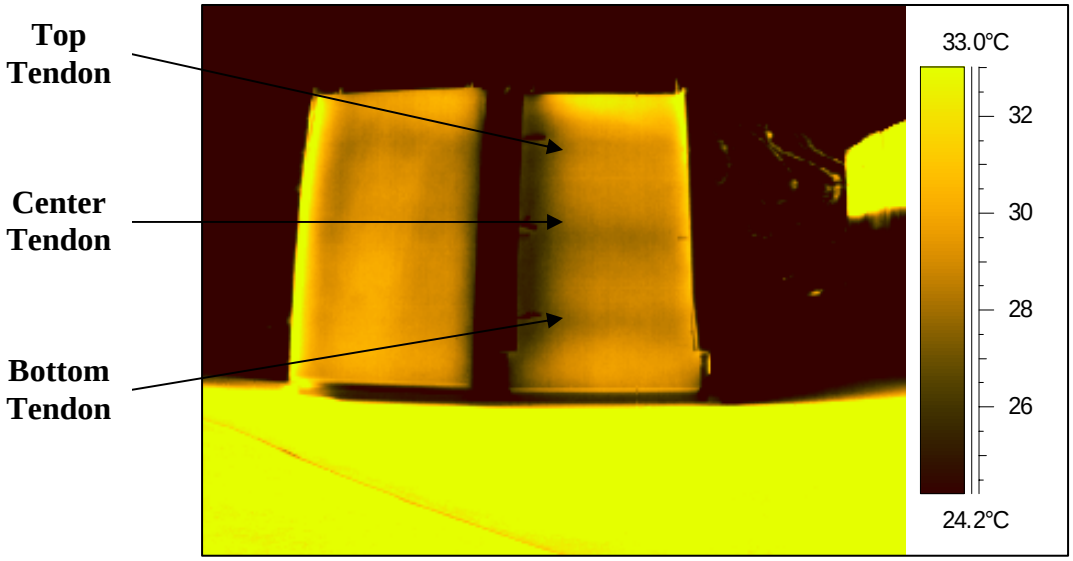


Figure 3.31 - Exterior image of Specimen 3 (left) and Specimen 1 (right) (Pearson, 2003)

Each of the tendons in Specimen 1 was visible and all appeared cooler than the surrounding concrete. The center tendon containing 30 post-tensioning steel strands appeared the coolest of the three tendons. The top duct contained only 20 steel strands, so it should appear warmer than the center duct, which it did. Additionally, the bottom duct contained 30 steel strands and a small simulated void. From the baseline temperature profile shown in Figure 3.25, the finite element model predicted that the bottom tendon should be approximately the same temperature as the top duct containing 20 steel strands. As can be seen, the top and bottom ducts were approximately the same temperature as predicted.

The location of the center tendon of Specimen 2 should appear colder than the surrounding concrete on the unheated surface due to the large simulated void embedded in the HDPE duct containing only four post-tensioning steel strands. When thermal images were taken

on the heated surface, the location of the center tendon should appear warmer than the surrounding concrete. This was attributed to the low thermal conductivities of the HDPE duct and the simulated void. Thermal images of Specimen 2 illustrated the basic trends predicted by the finite element model. Figure 3.32 is a thermal image of the heated surface of Specimen 2.

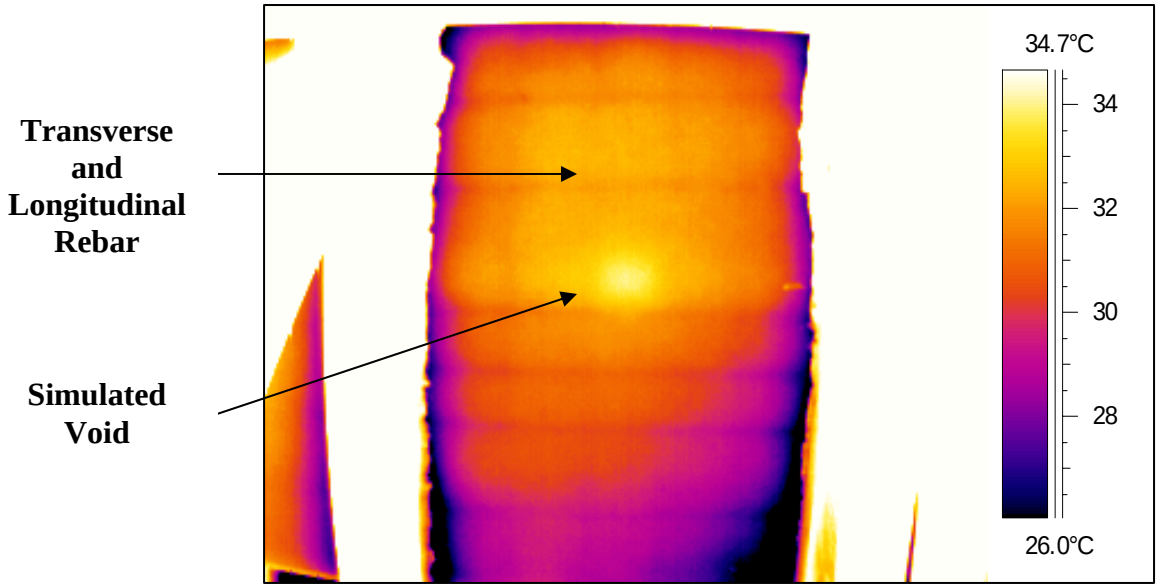


Figure 3.32 - Interior image of Specimen 2 (Pearson, 2003)

In Figure 3.32, the center tendon containing the large simulated void has a distinct warm spot located directly in the center of the specimen, as predicted by the finite element model. The top tendon can be faintly seen, but it is not completely distinguishable and the location would be difficult to state with any certainty without prior knowledge of the locations of the tendons. The bottom duct was hard to distinguish in all of the thermal images taken by Pearson (2003). This can be attributed to convection cooling occurring on the boundary edges of the specimen. This cooling causes large temperature variation on the surface of the specimens and makes tendon and void detection more difficult with the thermal camera.

After comparing the results of the finite element models with the thermal images obtained by Pearson (2003), it was concluded that the finite element models were effective in predicting the surface temperature profiles for each specimen. Temperature trends observed in each of the thermal images correlated well with the finite element model predictions.

# Chapter 4 – Experimental Methods

## 4.1 – Overview

Thermal imaging tests were conducted at Washington State University to investigate the necessary thermal parameters for inspections of post-tensioned box girder bridge walls. A total of eight different rectangular concrete specimens of varying thickness were previously constructed. Each specimen contained three grouted post-tensioning tendons. Each tendon was constructed with either a HDPE or steel duct. Additionally, varying quantities of post-tensioning steel strands were placed inside each duct. Six of the eight specimens contained simulated voids to represent an air void located within the grouted ducts.

Testing of the specimens was conducted in three phases. During the summer months, the specimens were supported by three-sided wooden sheds to expose one specimen face to solar radiation while simultaneously cooling the opposite face of the specimen. After the weather turned colder, testing switched to electric silicone rubber flexible heating blankets or an electric infrared heater as the applied heat source on one face of the specimens.

## 4.2 – Testing Setup

Initial tests employed solar energy to heat one face of the specimens while the opposite face was cooled with air conditioning. Three sheds were constructed to support the specimens. Design and construction details for the sheds are described by Pearson (2003). Figure 4.1 shows one of the test sheds before being loaded with a specimen.

Figure 4.1 – One empty testing shed
(Pearson, 2003)

Subsequent testing involved heating one face of a specimen using electric silicone rubber flexible heating blankets or an electric infrared heater. A wood frame stand was constructed to support the specimens. Before the wood frame stand was built, ignition temperatures of the wood were researched because of the potential that the heating blanket could come in contact with the wood support frame. Research indicated that the wood would start to discolor, strength degradation would begin, and the wood would begin to char at temperatures between 100°C (212°F) and 250°C (482°F) and ignition could occur at temperatures above 250°C (482°F) (Forest Products Laboratory, 1987). Since these temperatures were higher than the 87.8°C (190°F) maximum temperature the heating blanket would reach, the use of a wooden frame was acceptable.

The frame was constructed with 38 mm x 140 mm (2 x 6) sawn lumber and was 2.4 m (8.0 ft) long, 1.2 m (45.5 in) wide, and 1.8 m (6 ft) tall. The support frame was designed to

prevent the 40 cm (16 in) thick concrete specimens from falling forward off the stand. The support frame was also designed to resist wind loading on the specimen if used outdoors. The frame was also designed to be picked up by a forklift while supporting a specimen. Figure 4.2 is an image of the wood stand supporting Specimen 8.

Figure 4.2 – Wood support frame supporting Specimen 8

**4.3 – Testing Procedure**

Initial tests utilized solar energy on warm, sunny days to heat one surface of the specimens, while the interior of the test sheds and the opposite face of the specimens were cooled using wall-mounted air conditioners. These tests were conducted primarily when the outside temperature was above 32°C (90°F) since this provided large temperature differentials between the heated surface and the air conditioned surface of the specimens. Figure 4.3 shows the test setup with four of the specimens leaning against the test sheds. The black electrical tape

shown on each of the specimens in Figure 4.3 indicates the locations of the ends of the tendons in each specimen. Due to the high emissivity of the electrical tape, each strip of tape appeared in the thermal images, indicating the locations of the tendons.

Figure 4.3 – Solar heating test setup

During initial solar heating tests, a large variance in temperatures across the face of each specimen was observed. This was also observed during the testing conducted by Pearson (2003). These large temperature differences made it difficult to detect the top and bottom tendons and the standard steel reinforcement near the edges of each specimen. The most noticeable temperature difference was caused by the sun shining directly on the edges of the specimens. The smaller the temperature variation on the face of the specimen the easier it is to detect small changes in temperatures from underlying discontinuities using the thermal camera.

It was decided that an insulating barrier around the perimeter of each specimen would be beneficial in reducing these temperature variations caused by uneven heating. The insulating barriers were constructed from 38 mm x 140 mm (2 x 6) sawn lumber, 1.1 cm (7/16 in) thick oriented strand board (OSB) sheathing, and fiberglass insulation. The barriers were constructed in three pieces to allow easy removal when the concrete specimens were removed from the test sheds. Figure 4.4 shows the insulating barriers installed on the specimens.

Figure 4.4 – Insulating barriers installed on the specimens

The air conditioners were started very early in the mornings when the ambient outdoor temperature was the lowest in order to keep the interior of the sheds as cool as possible. Interior and exterior air temperatures were measured with an ExTech EA-15 temperature datalogger with an accuracy of 1%. A separate temperature probe was used on the EA-15 to record surface temperatures of the concrete specimens.

The thermal camera used to take the thermal images of the specimens was a FLIR Systems ThermaCAM P60 with a built-in 24° lens and a 45° wide angle lens attachment (see Figure 4.5). The thermal camera had a resolution of 320 x 240 pixels and a thermal sensitivity of 0.06°C (0.1°F) at 30°C (54°F). Thermal images were taken of both faces of the specimens during testing. The best time determined by Pearson (2003) to take thermal images was just after the sun was shining directly on the surface of the specimens. Therefore, images were taken around 6:00 P.M. when the sun was low enough on the horizon that the sunlight was not shining directly on the specimens.


Figure 4.5 – FLIR Systems ThermaCAM P60 (FLIR Systems, 2005)

Additional tests were conducted using electric silicone rubber flexible heating blankets manufactured by Michaels Enterprises, Inc. to heat one face of the specimens. The blankets were designed to completely cover one face of the concrete specimens to ensure an even heat distribution. Since the silicone rubber material was limited to a width of 94 cm (37in), two heating blankets were designed to be used side by side on a single concrete specimen. The

blankets were powered by a 240 volt 3-Phase electrical outlet. The internal heating element density was designed to provide a heat output of 3.0 W/in$^2$. Each blanket was equipped with two 87.8°C (190°F) thermostats to regulate the output temperature of the blanket. Additionally, each blanket was equipped with grommets on one end to allow the blankets to be draped over one of the vertical surfaces of the concrete specimens when placed on the wooden support frame. Figure 4.6 shows the thermal blankets on one face of Specimen 4 in the support frame.

Figure 4.6 – Silicone rubber flexible heating blankets applied to Specimen 4

A 2.0 cm (3/4 in) thick CDX plywood insulating shield was constructed to lay on the surface of the blankets to direct most of the thermal energy into the concrete specimens. It was determined that the plywood would also be safe when in direct contact with the thermal blanket. The shield was bolted onto the support frame to allow for easy installation and removal when

switching specimens. After the insulating shield was bolted onto the support frame, two elastic straps were used to hold the plywood against the blankets and the specimen. Figure 4.7 shows the plywood insulating shield in place.

Figure 4.7 – Plywood insulating shield

The heating blankets were used to heat the specimens for a minimum of four hours. Images were taken periodically throughout the day to monitor any noticeable changes in temperatures on the unheated face of the specimen. When tendon or void locations were detected during inspection, temperature readings of each surface of the specimen were taken using the EA-15 temperature datalogger.

Finally, a Fostoria 4900 kJ (46,000 BTU) electric infrared heater was used to heat one face of the specimens. The infrared heater required a 240 volt 3-phase electrical outlet. There were not any thermostats installed on the heater to regulate the heat output of the heater or to shut it off at a prescribed temperature. Since the infrared heater was smaller than the concrete specimens, the heater was centered over the specimens to provide the most even heat distribution possible. Similarly to the testing conducted using the heating blankets, the heater was started in the morning and ran for approximately seven hours heating the specimens. Thermal images and temperature readings of both faces were taken at periodic time intervals to monitor heat flow through the specimens. Figure 4.8 shows the infrared heater setup with Specimen 8.

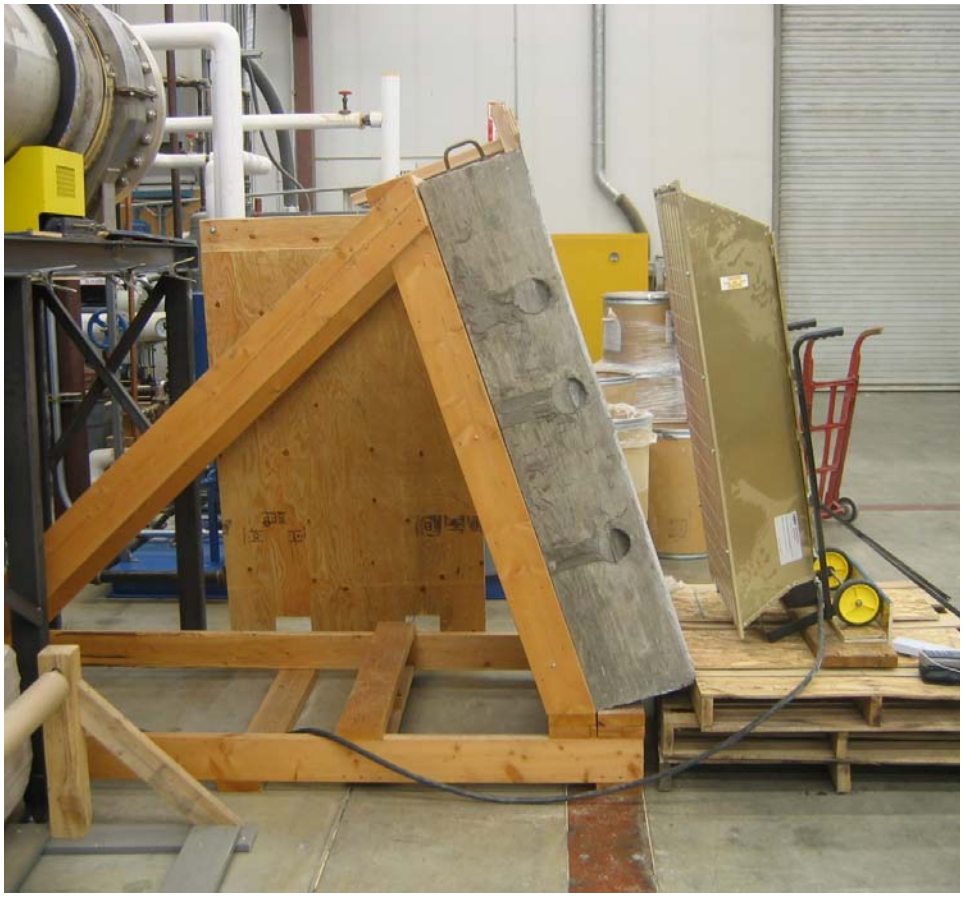

Figure 4.8 – Infrared heating setup

# Chapter 5 – Test Results

## 5.1 – Introduction

Testing was conducted in three phases to investigate the feasibility of heating post-tensioned concrete sections using solar energy, electric silicone rubber flexible heating blankets, and an infrared heater. The purpose of the thermal imaging tests was to expand on the results obtained by Pearson (2003) and determine the necessary thermal parameters to utilize thermal imaging on post-tensioned concrete box girder bridge walls. A total of 17 tests were conducted utilizing the three different heating methods. Five tests were conducted using solar heating while air conditioning the test sheds, 10 tests utilized the silicone rubber heating blankets, and two tests were conducted using the infrared heater. Multiple thermal images were obtained during each test, only the images that provided key results are presented in this report.

The test results are organized by method. Tests using solar heating and air conditioning were conducted first, followed by the silicone rubber heating blankets, and finishing with the infrared heater. The results are discussed in the same order. Testing using solar heating was only conducted on Specimen 1, Specimen 2, Specimen 3, and Specimen 7. Specimen 1, Specimen 2, and Specimen 7 were 20 cm (8 in) thick and Specimen 3 was 30 cm (12 in) thick. Testing was not conducted using any of the 40 cm (16 in) specimens since the results from finite element modeling showed that an applied temperature of at least 260.0°C (500°F) would be required to detect the locations of the tendons or voids. This temperature could not be achieved using the silicone rubber heating blankets or the infrared heater. Figure 5.1 shows the specimens on the test sheds during the solar heating portion of the research. The sheds were oriented so the

exterior faces of the specimens were facing south to obtain full exposure to the sun throughout the day.

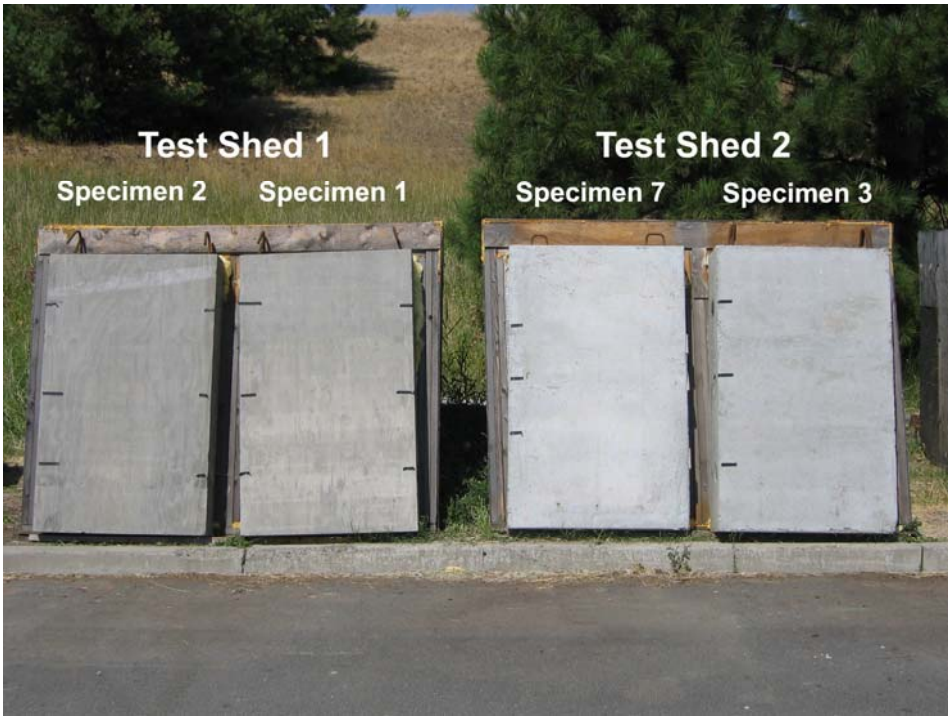


Figure 5.1 – Test setup for solar heating

When thermal images were taken, an even heat distribution throughout the specimens made the location of voids and tendons easier to detect. When the specimens were heated unevenly, large temperature variations on the faces of the specimens made void and tendon detection difficult. The thermal camera would only differentiate between small temperature variations on the surface of the specimens caused by embedded voids when the range of temperatures on the surface being viewed was small.

Varying the color palettes used in the thermal camera also helped in distinguishing 1°C (1.8°F) and smaller temperature differences. After the thermal radiation emitted from the objects has been converted into an image by the thermal camera, a color palette is a range of colors that the thermal camera uses to provide a color representation of the temperature distribution

throughout the surface of the object being viewed. During the research, it was found that the Rainbow HC color palette was most effective in distinguishing small temperature variations. The Rainbow HC color palette provides a large contrast between the various colors.

### 5.2 – Solar Heating and Air Conditioning Results

The first test involving solar heating was conducted on August 16, 2005. The maximum outside air temperature was approximately 31°C (87°F). The interior air temperatures for Shed 1 and Shed 2 were 18.3°C (65°F) and 19.4°C (67°F), respectively. The average surface temperature differential though the thickness of the three 20 cm (8 in) thick specimens was 4.8°C (8.7°F). The surface temperature differential through the thickness of the 30 cm (12 in) thick specimen was 6.6°C (12°F). The air conditioners were started early on the morning of August 16$^{th}$ and continued to run throughout the day. Observations noted by Pearson (2003) stated that the best time to obtain thermal images was in the late afternoon after the direct sunlight was not shining on the specimens. Therefore, thermal images were obtained for the specimens starting at 4:30 P.M. During each of the days the solar heating was conducted, the wind was calm and skies were clear.

Figure 5.2 shows the first interior thermal image of the air conditioned surface of Specimen 2 taken on the 16$^{th}$ of August at 6:30 P.M. Specimen 2 provided the most distinguishable results. The dark blue areas surrounding the specimen were the cooler wood framing inside Shed 1. The warm temperature region near the edges of the specimen was attributed to the sun heating the edges of the specimens throughout the day. In the center of the specimen, the transverse rebar with 2.5 cm (1 in) of concrete cover was clearly visible. The longitudinal rebar had 1.6 cm (5/8 in) more concrete cover than the transverse rebar and was not

visible in Specimen 2. Directly in the center of the specimen, a definite cool spot was visible indicating the location of the large simulated void embedded in the HDPE duct containing four post-tensioning steel strands. The center of the cool spot was approximately 1.5°C (2.7°F) cooler than the surrounding concrete.

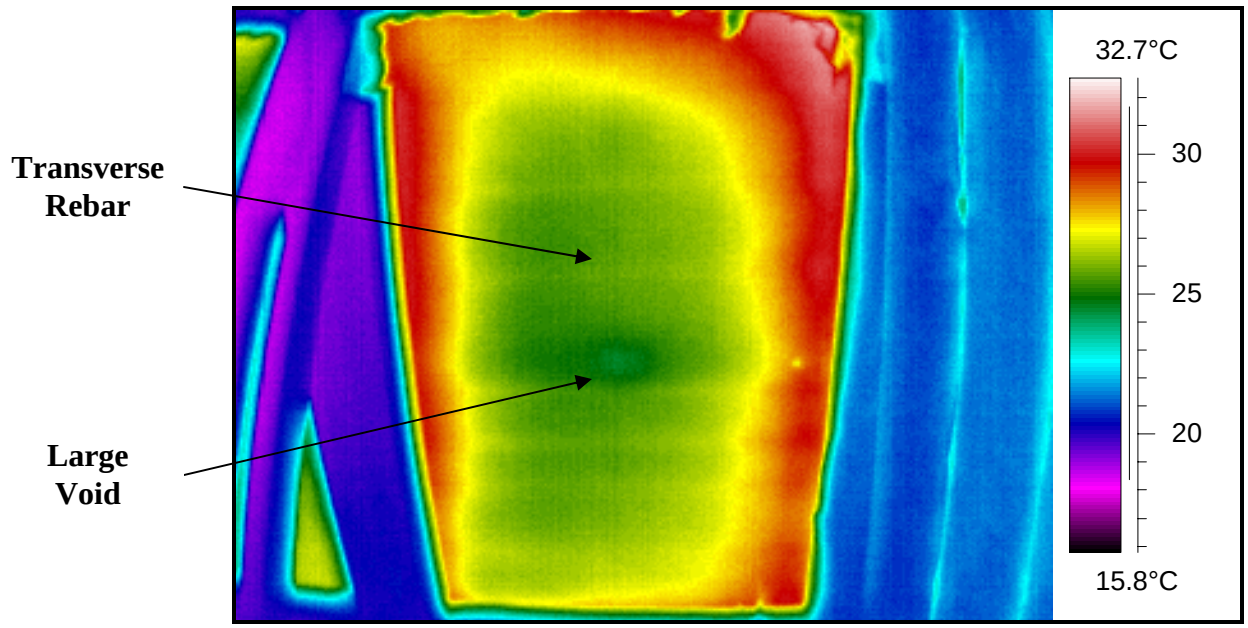


Figure 5.2 – Interior thermal image of Specimen 2 taken on August 16, 2005 at 6:30 P.M.

An interior thermal image of the air conditioned surface of Specimen 1 taken at 6:30 P.M. on August 16th is shown in Figure 5.3. The results obtained for Specimen 1 were not as clear as those for Specimen 2. As indicated in Figure 5.3, the center tendon was visible, but not across the entire width of the specimen. Where distinguishable, the center tendon was approximately 1.0°C (1.8°F) warmer than the surrounding concrete. Near the bottom of the specimen was a small cold spot indicated in Figure 5.3. The bottom tendon contained a small simulated void that was embedded inside a steel post-tensioning duct containing 30 steel strands. Since the entire length of the bottom tendon was not visible due to the heating along the edges of the specimen, the cool spot could not be definitely confirmed as the simulated void. As in

Specimen 2, the transverse rebar in Specimen was clearly visible, but the longitudinal rebar was not. The high temperature on the left edge of the specimen was due to the sun shining on the edge of the specimen throughout most of the day since the left edge of the specimen has an easterly exposure. Since the right edge of Specimen 1 was very close to the left edge of Specimen 2, it was not exposed to direct sunlight and heated like the left edge.

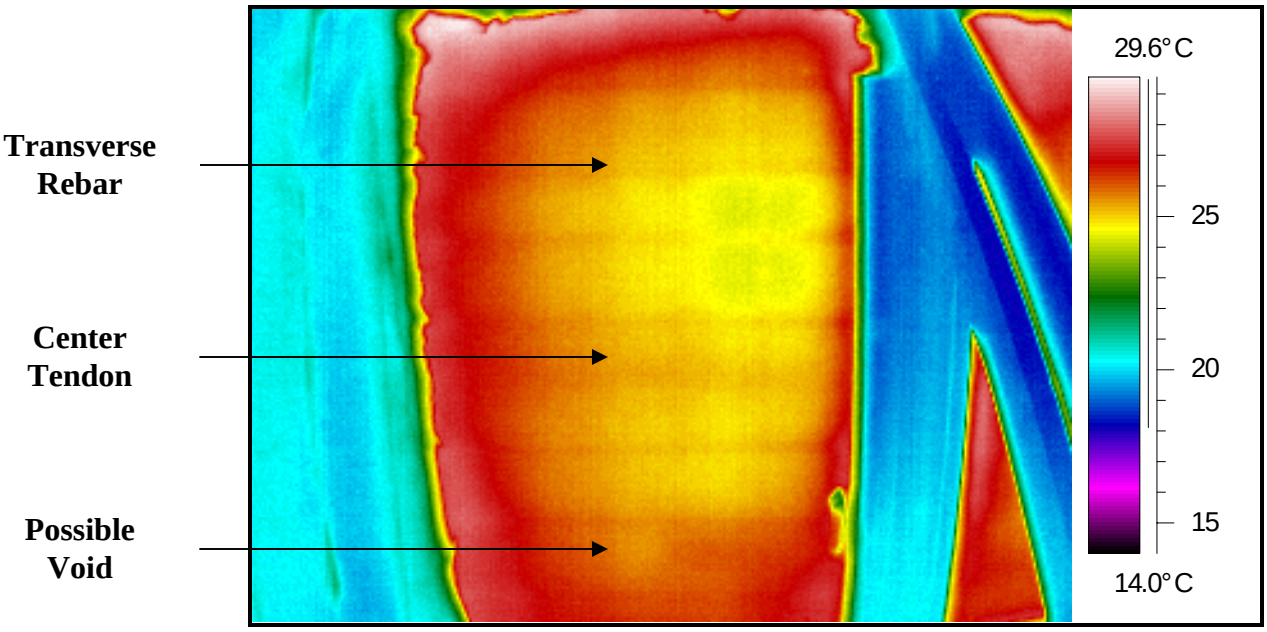


Figure 5.3 – Interior thermal image of Specimen 1 taken on August 16, 2005 at 6:30 P.M.

Notable results from the interior thermal images were not obtained for Specimen 7 and Specimen 3. Exterior thermal images of the heated surfaces were also taken for each of the specimens, but the exterior images were not as useful as the interior images for detecting tendons and voids inside the specimens.

The next solar heating tests were conducted on August 21, 2005 and began at approximately 5:30 P.M. The maximum outside air temperature during the day was approximately 36°C (97°F). The interior air temperatures for Shed 1 and Shed 2 at the time of testing were 20°C (68°F) and 21.1°C (70°F), respectively. The averaged surface temperature

differential through the thickness of the three 20 cm (8 in) thick specimens was 10°C (18°F). The surface temperature differential through the thickness of the 30 cm (12 in) thick specimen was 12.2°C (22°F). The air conditioners were started at approximately 3:00 A.M. on the morning of August 21st and continued to run throughout the day to keep the interior of the test sheds as cool as possible.

Figure 5.4 is an internal thermal image of the air conditioned surface of Specimen 2 taken at 5:30 P.M. on the 21st of August. Once again, the large simulated void in the center duct appears as a cool spot directly in the center of the specimen. The center of the cool spot was approximately 2.0°C (3.6°F) cooler than the surrounding concrete. The transverse rebar appeared more clearly than in the results obtained on August 16th, but the longitudinal rebar was still not visible. As seen in the previous images, the heating along the edges of the specimens had a large impact on the thermal images. In Figure 5.4, there was a 13°C (23°F) temperature difference between the upper right corner of the specimen and the cool spot directly in the center of the specimen surface. This large difference in temperatures across the surface makes detection of small temperature changes caused by subsurface discontinuities difficult with the thermal camera. The warm areas around the edges of the specimen mask the rebar and tendons in those locations of the specimen. The top tendon was also not visible in Specimen 2 due to the edge heating.

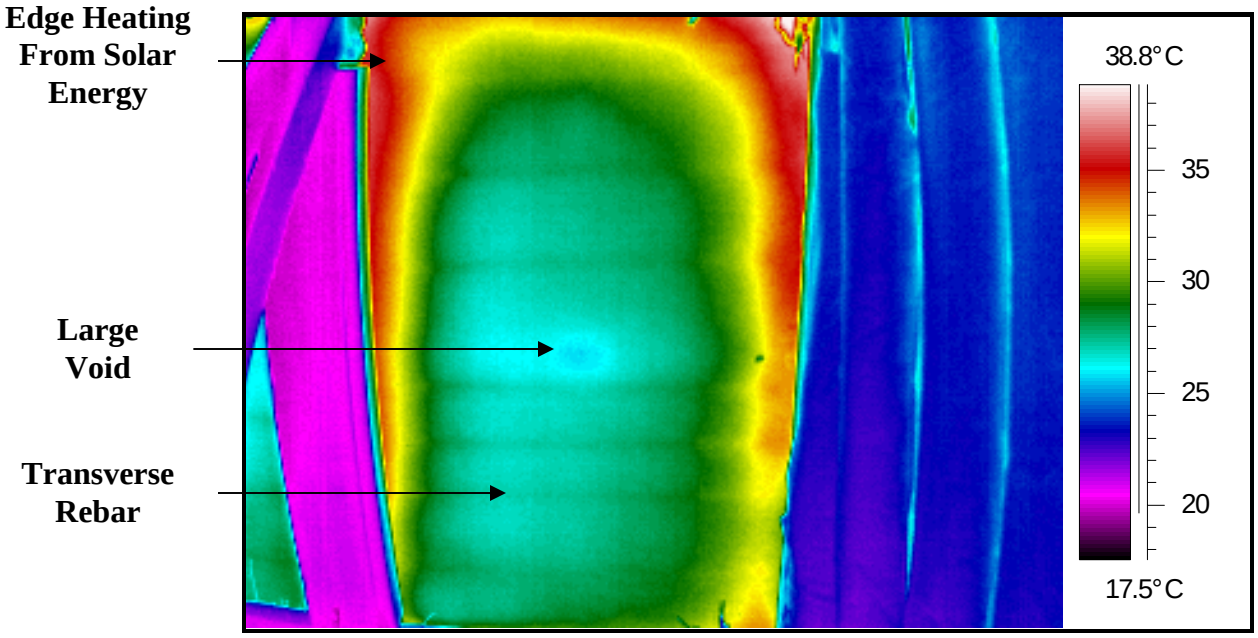


Figure 5.4 – Interior thermal image of Specimen 2 taken on August 21, 2005 at 5:30 P.M.

An interior thermal image of the air conditioned surface of Specimen 1 is shown in Figure 5.5. The center tendon appeared much more clearly than in Figure 5.3. There was a 1.3°C (2.3°F) temperature difference between the center duct and the surrounding concrete. The transverse rebar also appeared more clearly than it did on August 16th. It can be noted that the rebar and center tendon are detectable across most of the width of the specimen. This is also an improvement over the images obtained on the 21st of August. In several locations, the longitudinal rebar is also noticeable in Figure 5.5. The cold spot located near the bottom of the specimen that was observed in Figure 5.3 is once again visible in Figure 5.5. Since the location of the cool spot is the same in both Figure 5.3 and Figure 5.5, it can be concluded that this is most likely the small simulated void embedded in the steel duct containing 30 post-tensioning steel strands. The top tendon in Specimen 1 was not visible during testing on August 21st. Once again, tendons, rebar, and simulated voids could not be detected in Specimen 3 and Specimen 7.

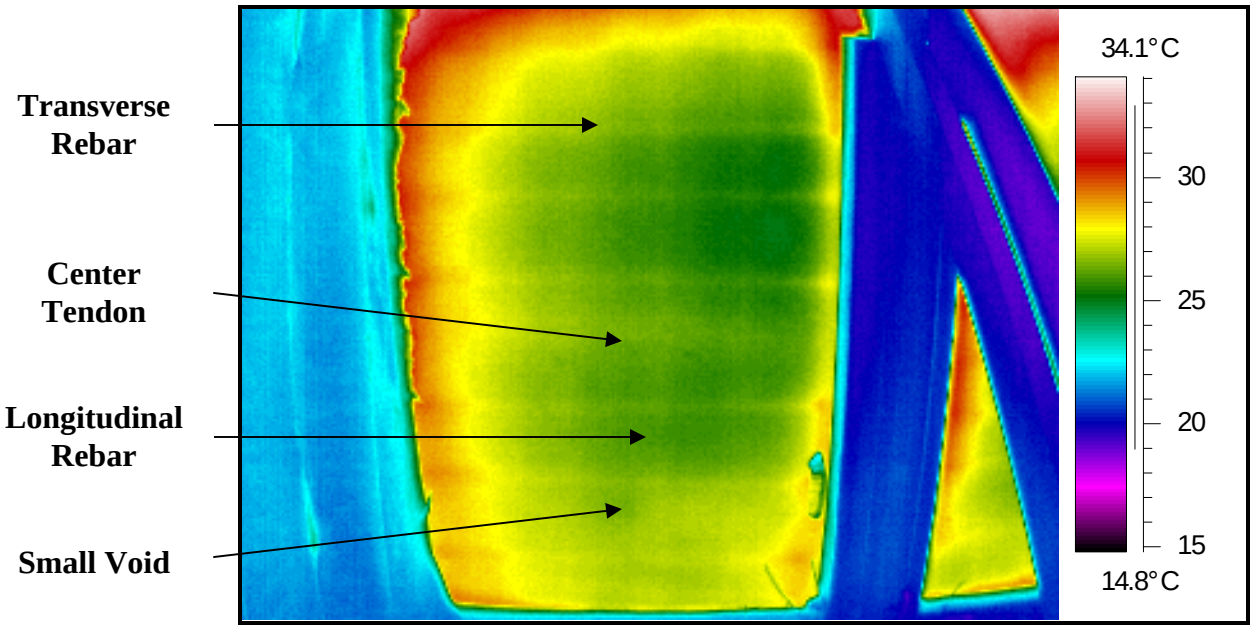


Figure 5.5 – Interior thermal image of Specimen 1 taken on August 21, 2005 at 5:30 P.M.

Solar energy heating the edges of the specimens was seen in Figures 5.3 and 5.5, was also mentioned by Pearson (2003) as a problem affecting the quality of the thermal images. Therefore, as mentioned in Chapter 4, an insulating border was constructed around each specimen to help minimize this edge heating. The insulating border was placed on the sides and the top of the specimens and can be seen in Figure 4.6.

After the insulating border was constructed, testing continued on August 28, 2005, beginning at 5:30 P.M. The maximum outside air temperature during the day was approximately 33°C (91°F). The interior air temperatures for Shed 1 and Shed 2 at the time of testing were 18.3°C (65°F) and 19.4°C (67°F), respectively. The averaged surface temperature differential through the thickness of the three 20 cm (8 in) thick specimens was 7.2°C (13°F). The surface temperature differential through the thickness of the 30 cm (12 in) thick specimen was 10°C (18°F). The air conditioners were started at approximately 2:30 A.M. on the morning of August 28$^{th}$.

Figure 5.6 shows an exterior thermal image of the heated surface of Specimen 2 and Specimen 1 taken at 5:30 P.M. Comparisons with Figures 5.3 and 5.5 show that the insulating boundaries made significant improvements in reducing the temperature variations across the surface of the specimens. In Figure 5.6, the maximum temperature variation across the surface of either specimen was 2.4°C (4.3°F). All three of the tendons were detected in Specimen 1 as shown in Figure 5.6. The center steel duct appeared the coldest, which was expected since it contained 30 post-tensioning steel strands and transferred the thermal energy the most efficiently because of the high thermal conductivity of the steel. The simulated void in the center duct of Specimen 2 was also apparent as a hot spot on the surface of the specimen. The simulated void appeared as a hot spot on the exterior image because of the low thermal conductivity of the HDPE duct and the large simulated void causing the thermal energy to be transferred less efficiently compared to the surrounding concrete. The simulated void in the bottom duct of Specimen 1 was not visible in the exterior images like it was in the interior images observed in previous tests. The transverse and longitudinal rebar were not visible in either of the specimens.

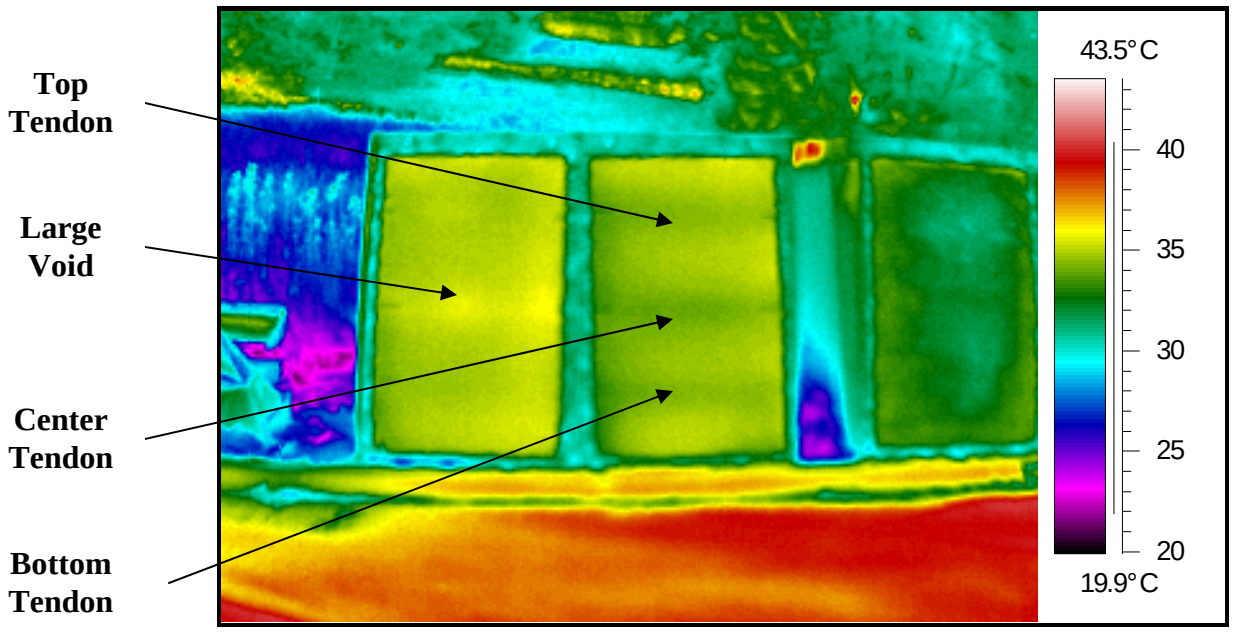


Figure 5.6 – Exterior thermal image of Specimen 2 (left) and Specimen 1 (right) taken on August 28, 2005 at 5:30 P.M.

The interior thermal image shown in Figure 5.7 displays the air conditioned surface of Specimen 2. Comparing Figure 5.7 taken on August 28th to Figure 5.4 taken on August 21st, it can be clearly seen that the insulating border helped reduce edge heating on the specimens. By reducing edge heating, thermal images showing more of the subsurface features of the specimens were obtained. The transverse rebar was distinctly shown across the entire width of the specimen. The large simulated void in the center duct was again detected. The top and bottom tendons in Specimen 2 were not visible during the testing conducted on the 28th of August. The location of the center tendon on either side of the large simulated void was not clear, but there was a slightly cooler region on the right side of the void as indicated in Figure 5.7. The detection of the simulated void would seem probable since the center duct contained only four post-tensioning steel strands.

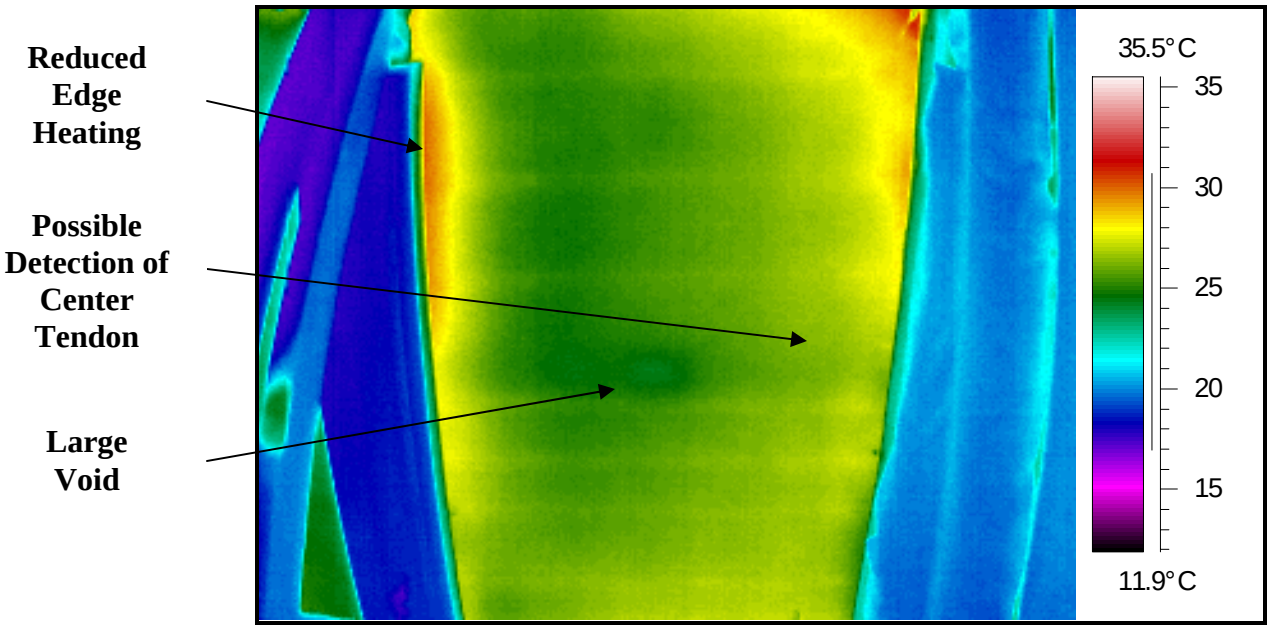


Figure 5.7 – Interior thermal image of Specimen 2 taken on August 28, 2005 at 5:30 P.M.

Figure 5.8 is an exterior thermal image taken of the bottom half of Specimen 3 at 6:30 P.M. Specimen 3 did not contain simulated voids, but included different concrete cover depths to each tendon. From the heated exterior surface, the bottom tendon was only 5 cm (2 in) beneath the surface of the concrete. As indicated in Figure 5.8, electrical tape placed on the surface of the specimen appears as a blue line in the thermal images. The electrical tape was used as a marker to indicate the centerline of the tendon. Since the bottom tendon was constructed with steel ducts and 30 post-tensioning steel strands, the location of the tendon should appear cooler when viewed from the heated surface because of the high thermal conductivity of the steel duct and strands. The location of the bottom tendon was indicated in Figure 5.8. This was the first time in this research project that a tendon in a 30 cm (12 in) thick specimen was detected.

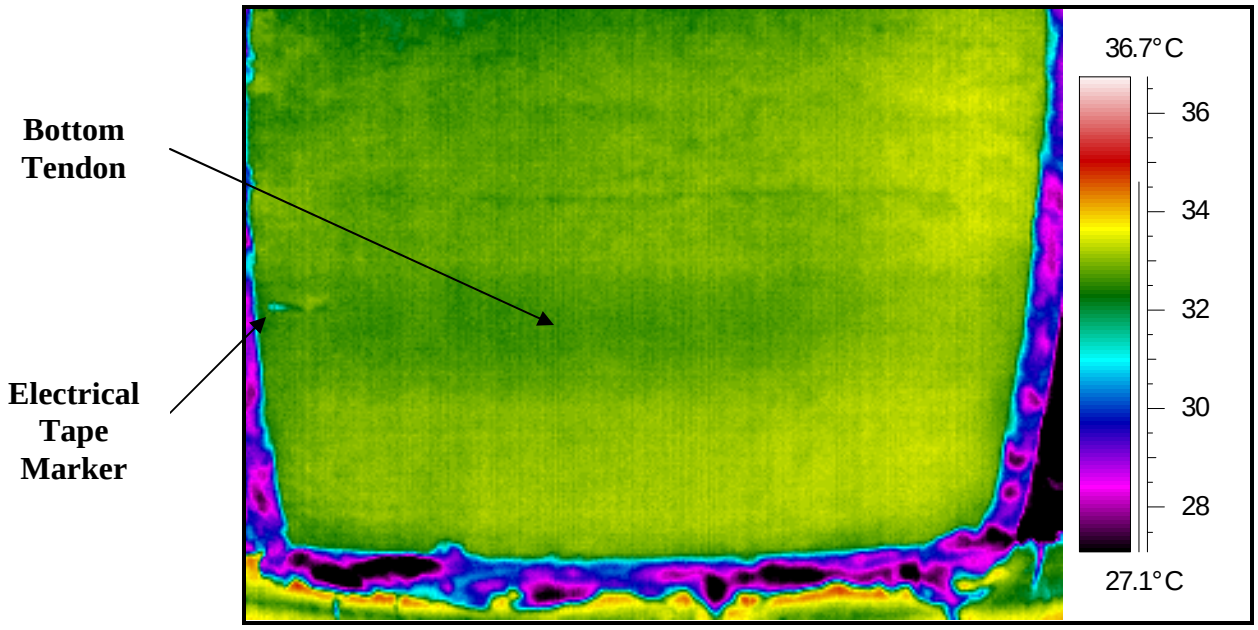


Figure 5.8 – Exterior thermal image of Specimen 3 taken on August 28, 2005 at 6:30 P.M.

Testing involving solar heating continued on September 7, 2005. The maximum outside air temperature was approximately 29.4°C (85°F). The interior air temperatures for Shed 1 and Shed 2 were 19.4°C (67°F) and 20°C (68°F), respectively. The averaged surface temperature differential through the thickness of the three 20 cm (8 in) thick specimens was 6.1°C (11°F). The surface temperature differential through the thickness of the 30 cm (12 in) thick specimen was 9.9°C (16°F). The air conditioners were started at 3:30 A.M. on the morning of September 7$^{th}$. The only specimen that provided different results from those discussed earlier was Specimen 7.

The thermal image shown in Figure 5.9 is an exterior view of the heated surface of Specimen 7 taken at 5:00 P.M. The thickness of Specimen 7 was not constant across the cross section and caused areas of the surface to have an uneven temperature distribution. The center duct of Specimen 7 contained two simulated voids located approximately at the third points across the width of the specimen. As indicated in Figure 5.9, the two warm spots located at the

specimen mid-height were believed to be the two simulated voids. Since one simulated void was larger than the other and would transfer less thermal energy, one appeared warmer than the other. The concrete surface temperature at the location of the left simulated void was approximately 1.5°C (2.7°F) warmer than the surrounding concrete. The right simulated void was approximately 1.0°C (1.8°F) warmer than the surrounding concrete. The locations of the top and bottom tendons were visible on the left half of the specimen. Near the bottom of the specimen, a distinct warm region on the surface of the specimen was present in the location of the bottom tendon. Also indicated in Figure 5.9, a warm area possibly caused by the top tendon was detected, but could not be definitely confirmed as the top tendon. The longitudinal and transverse rebar were not visible in any of the exterior thermal images taken of Specimen 7.

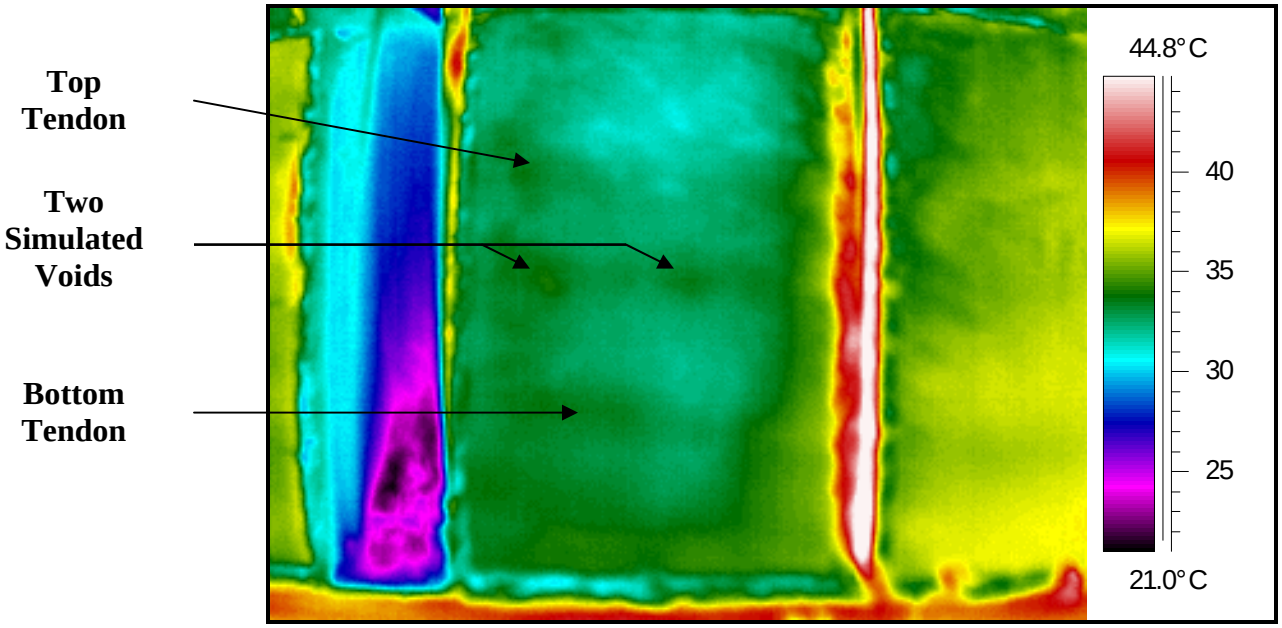


Figure 5.9 – Exterior thermal image of Specimen 7 taken on September 7, 2005 at 5:00 P.M.

The final test involving solar heating was conducted on September 8, 2005. The maximum outside air temperature was approximately 30.6°C (87°F). The interior air temperatures for Shed 1 and Shed 2 were 18.9°C (66°F) and 21.1°C (70°F), respectively. The

averaged surface temperature differential through the thickness of the three 20 cm (8 in) thick specimens was 7.8°C (14°F). The surface temperature differential through the thickness of the 30 cm (12 in) thick specimen was 10°C (18°F). Most of the thermal images provided results similar to those discussed earlier. The only specimen with improved results was Specimen 1.

Figure 5.10 is an interior view of the air conditioned surface of Specimen 1 taken at 4:30 P.M. Comparing Figure 5.5 to Figure 5.10, it can be seen that the insulating border significantly improved the quality of the thermal images for Specimen 1. There was only a 2.5°C (4.5°F) difference in temperature across the interior surface of the specimen. This small variation in temperatures allowed the thermal camera to detect smaller changes in temperatures. As indicated in Figure 5.10, the center duct was clearly visible along with the simulated void in the center of the bottom duct. Both the longitudinal and transverse rebar were also clearly visible in Figure 5.10. The main improvement seen by utilizing the insulating border was that the rebar and tendons were not masked by the edge heating and were visible across most of the width of the specimen.

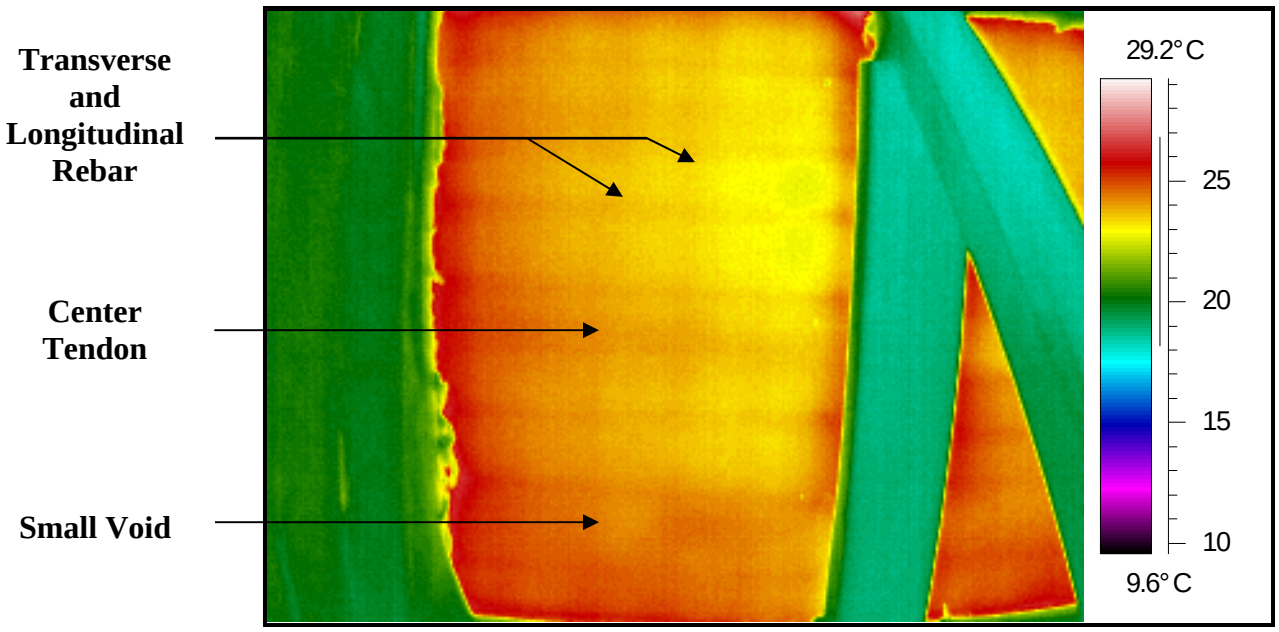


Figure 5.10 – Interior thermal image of Specimen 1 taken on September 8, 2005 at 4:30 P.M.

### 5.3 –Silicone Rubber Flexible Heating Blanket Results

Testing involving the electric silicone rubber flexible heating blankets was first conducted in October 2005. Since the manufacturer of the heating blankets recommended that they not become wet while in operation, all of the tests was conducted inside of the Wood Materials and Engineering Laboratory (WMEL) in Pullman, Washington. On October 4, 2005, the heating blankets were used to heat the specimen for approximately seven hours. The average air temperature inside the WMEL on the 4$^{th}$ of October was approximately 18.3°C (65°F). Since a wood support frame was used in the laboratory instead of the test sheds, all surfaces of the specimens were exposed to the ambient air conditions. Testing using the heating blankets began on Specimen 2. After the specimen was heated with the heating blankets for seven hours, the approximate temperature differential between the heated and unheated surfaces of the specimen was 25°C (45°F).

Figure 5.11 is a thermal image of the unheated surface of Specimen 2. As indicated in Figure 5.11, a large cool region appeared directly in the center of the specimen. This is the location of the large simulated void embedded in the center HDPE post-tensioning duct. This simulated void was also detected during the tests using solar heating and air conditioning. The transverse rebar was also clearly visible across the entire width of the specimen. The two hot spots located near the top of the specimen were from the different sections of the blanket cycling on and off at different times. The blanket was constructed with four thermostats designed to each shut off a section of the blanket after the preset temperature was reached. The accuracy between the thermostats varied, resulting in different sections of the blanket operating longer than others. The top and bottom tendons were not visible during the testing conducted on October 4th.

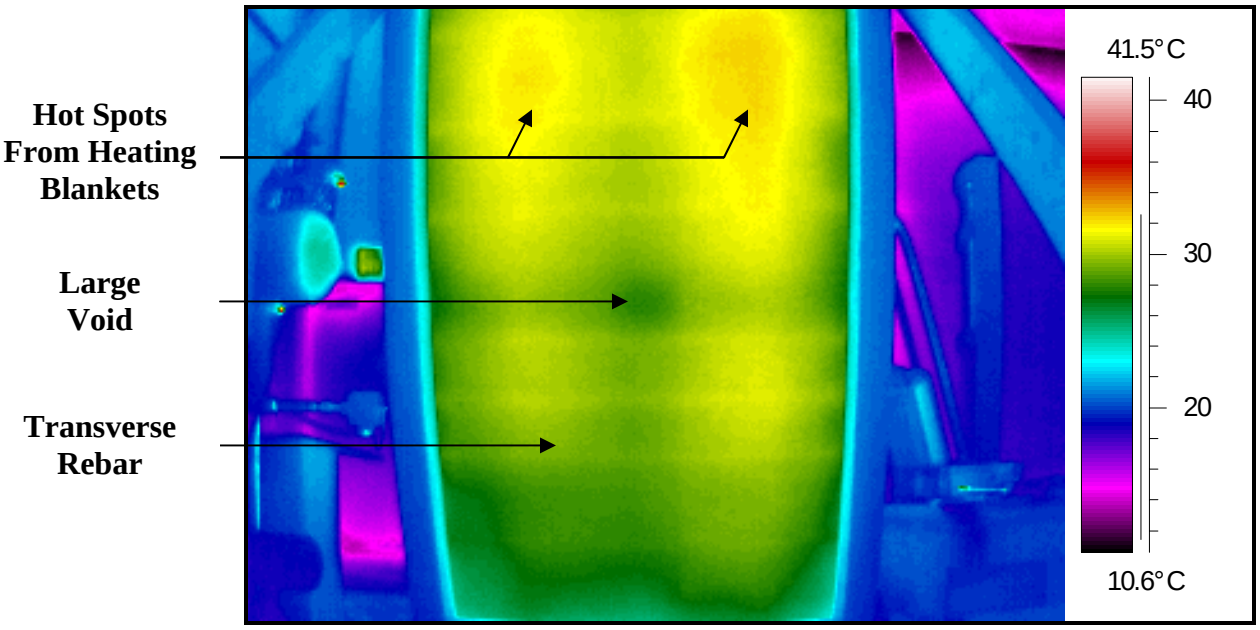


Figure 5.11 – Thermal image of Specimen 2 taken on October 4, 2005 at 4:30 P.M.

After the results from the testing conducted on October 4th were compiled, it was noticed that the temperature differential through the thickness of the specimen was not as large as

anticipated. The heated surface was only 54.4°C (130°F) after seven hours of heating when the thermostats were set to turn off at 87.8°C (190°F). It was determined that since heat was transmitted from both faces of the blankets, an insulating shield placed on the other surface of the blanket would direct more of the heat into the specimen instead of into the surrounding air. As discussed in Chapter 4, an insulating shield constructed from 2.0 cm (3/4 in) thick CDX plywood was placed over the blanket and mounted to the support frame.

After the plywood insulating shield was constructed, testing resumed on October 6, 2005. Specimen 2 was investigated again to observe the improvement the insulating shield provided. The average air temperature in the WMEL was 21.7°C (71°F) throughout the day. The maximum temperature differential across the thickness of the specimen was 38.9°C (70°F) after six hours of heating. The heated surface of the specimen reached a maximum temperature of 65.6°C (150°F). From these temperature readings, it can be seen that the insulating shield increased the temperature differential through the thickness of the specimen by approximately 19.4°C (35°F) and the heated surface temperature by 11.1°C (20°F).

The thermal image in Figure 5.12 is of Specimen 2 after six hours of heating with the silicone rubber flexible heating blankets. Comparing Figure 5.11 to Figure 5.12, it can be seen that the subsurface features appear more clearly in Figure 5.12 after the insulating shield was installed. The location of the large simulated void in the center of the specimen was approximately 2.5°C (4.5°F) cooler than the surrounding concrete. This was the largest observed difference in temperature between the large simulated void in Specimen 2 and the surrounding concrete. The transverse rebar was clearly visible throughout the specimen, but the longitudinal rebar was not detected. As indicated in Figure 5.12, the location of the entire tendon was also visible because of the low thermal conductivity of the HDPE duct and the four post-tensioning

steel strands. The hot spots from the heating blankets near the top of the specimen were again present. The top tendon containing four steel strands and a large simulated void enclosed in a steel post-tensioning duct was not visible. The bottom tendon containing 30 steel strands was also not visible.

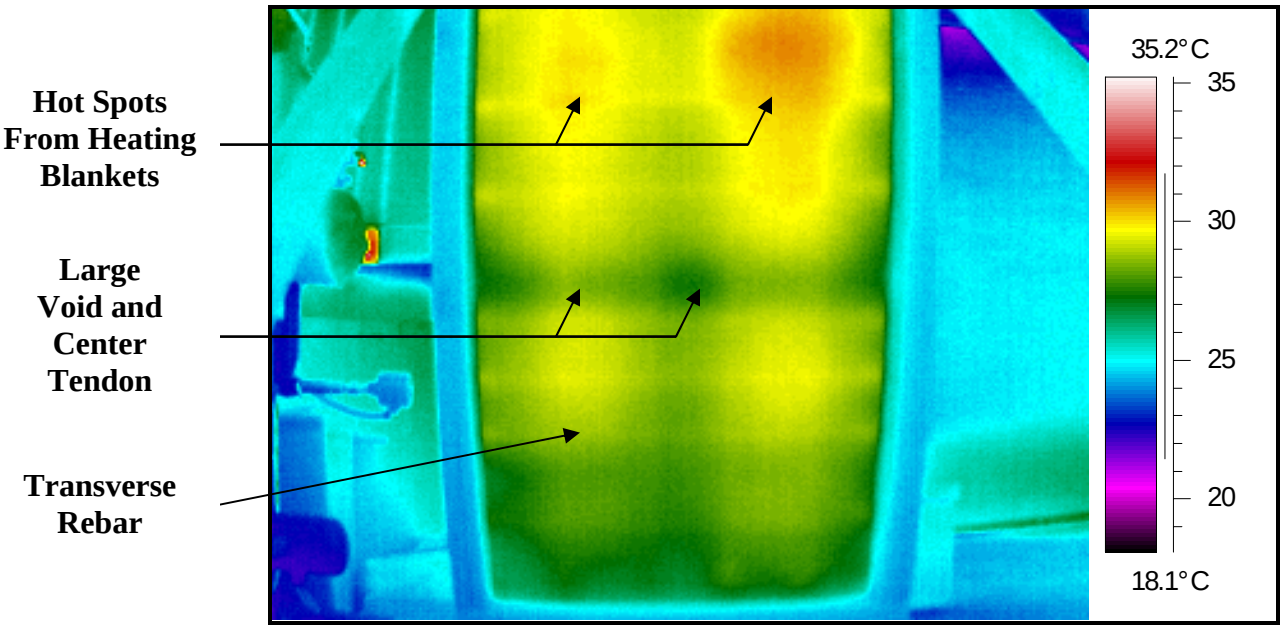


Figure 5.12 – Thermal image of Specimen 2 taken on October 6, 2005 at 6:30 P.M.

On October 10, 2005, Specimen 2 was removed from the support frame and Specimen 1 was set up for testing. The average air temperature in the WMEL during the testing was approximately 22.2°C (72°F). The maximum temperature differential through the thickness of the Specimen 1 was 36.1°C (65°F) after eight hours of heating with the heating blankets. The heated surface of the specimen reached a maximum temperature of 71.1°C (160°F).

In Figure 5.13, Specimen 1 can be seen after being heated with the silicone rubber heating blankets for approximately eight hours. The transverse rebar was clearly visible across the width of the specimen, but the location of the longitudinal rebar was not clear. As indicated in Figure 5.12, warm regions across the middle and top of the specimen were at the locations of

the top and center tendon. The turquoise blue cold area near the bottom of the specimen was a result of cold air blowing on the specimen. This cold air was from the large bay doors in the WMEL being open for shipping, allowing the cool outside air to enter the laboratory and cool the bottom of the specimen. Again, the two warm regions extending vertically over the surface of the specimen were from sections of the heating blanket not shutting down at the same time, causing uneven heating. This caused a cool line to appear vertically down the center of the specimen. If the locations of the tendons were not previously known, this region would appear similar to a tendon with voids running vertically through the specimen.

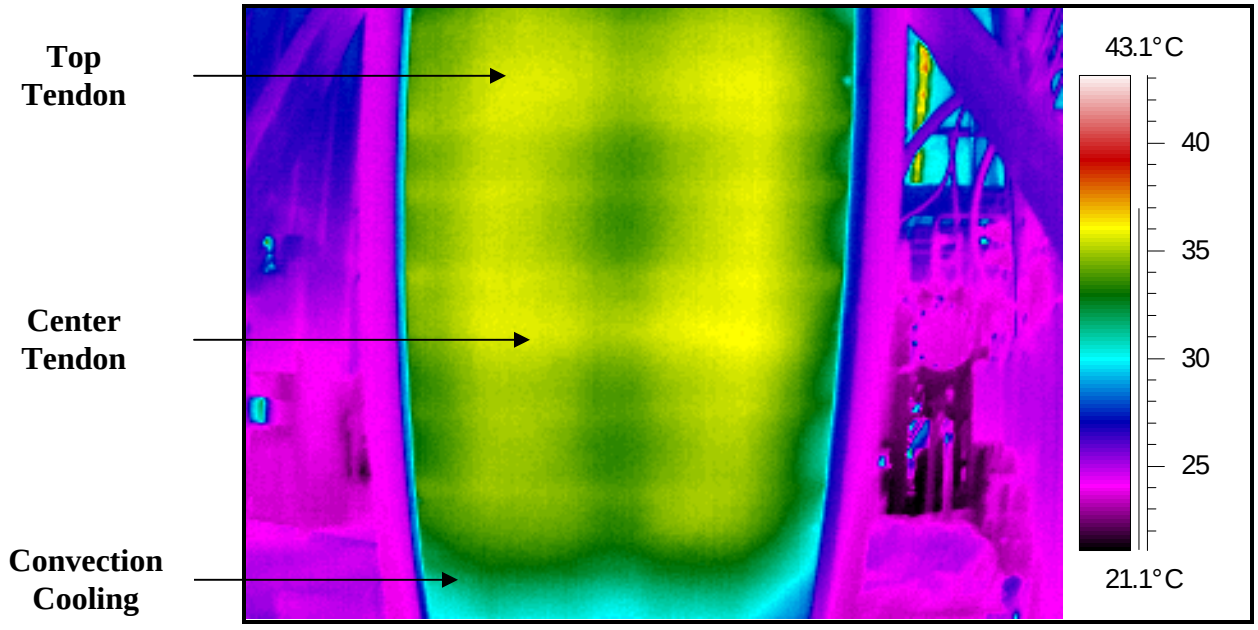


Figure 5.13 – Thermal image of Specimen 1 taken on October 10, 2005 at 4:30 P.M.

Testing continued on Specimen 1 on the 11th of October to observe the effects after the heating blanket was removed for a period of time. After the specimen was heated for eight hours, the blanket was removed to allow the specimen to begin cooling. The purpose was to observe the specimen as it cooled to see if uneven heating on the surface of the specimen would dissipate, providing clearer thermal images. During a two hour cooling period, thermal images

were taken every fifteen minutes to monitor the changes as the specimen cooled. As the specimen cooled, the details in the thermal image faded and none of the subsurface details became clearer than they were during the heating process. Figure 5.14 shows a thermal image of the unheated surface of Specimen 1 after the heating blankets had been removed for two hours. The temperature differential through the thickness of the Specimen 1 after the heat source was removed was approximately 19.4°C (35°F).

Comparing Figure 5.14 to Figure 5.13, it can be seen that the subsurface details in the specimen were clearer while the blankets were still heating the specimen. As the specimen cooled, the temperature differential across the thickness of the specimen decreased causing the rebar and tendons to appear more faint in the thermal image. The center tendon was still visible, but the location of the top tendon was not clear. Some of the transverse rebar was visible, but the clarity of the rebar in the thermal image was diminished after the cooling had occurred. From the thermal images taken during the cooling process, the conclusion was made that allowing the specimens to cool did not provided an improvement in the quality of the thermal images.

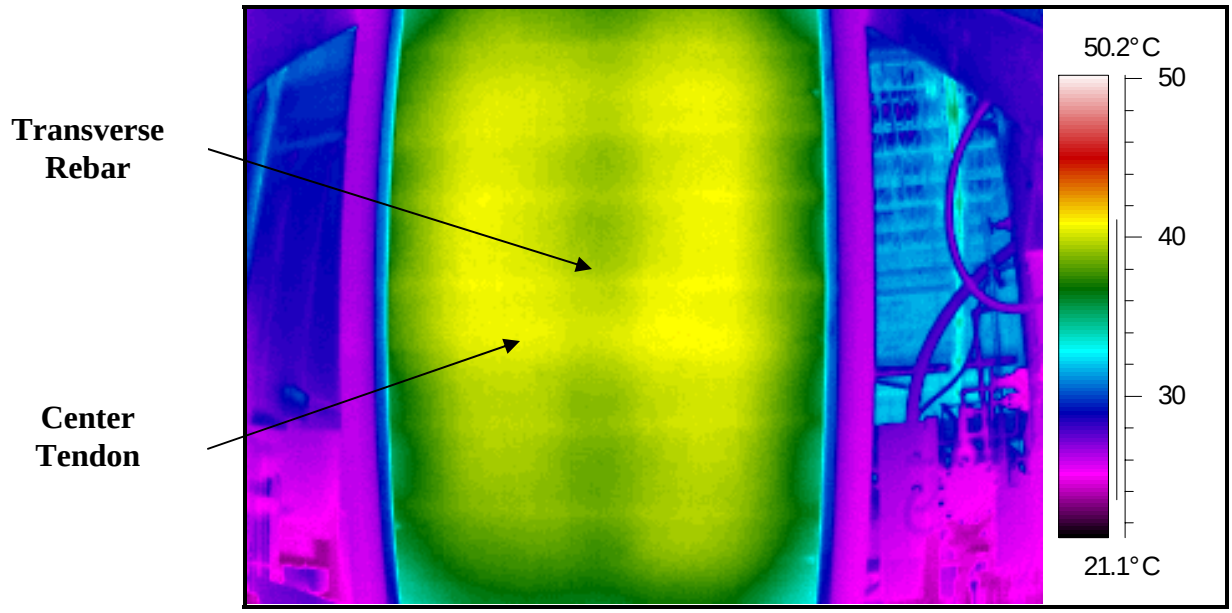


Figure 5.14 – Thermal image of Specimen 1 taken on October 11, 2005 at 6:00 P.M.

Testing resumed on October 14, 2005 with Specimen 7. Specimen 7 contained three HDPE ducts filled with 20 post-tensioning steel strands. Only the center duct included simulated voids located at the approximate third points across the width of the specimen. One simulated void was 5 cm (2 in) long and the other was 10 cm (4 in) long. The average air temperature in the WMEL during the testing was approximately 20°C (68°F). The maximum temperature differential through the thickness of the Specimen 7 was approximately 33.3°C (60°F) after six hours of heating with the heating blankets. The heated surface of the specimen reached a maximum temperature of 62.8°C (145°F).

The unheated surface of Specimen 7 is shown in Figure 5.15. All three of the tendons embedded in Specimen 7 were clearly visible. The tendons were 1°C (1.8°F) cooler than the surrounding concrete because of the low thermal conductivity of the HDPE ducts. The movement of the tendons during construction reported by Conner (2004) was clearly visible, since the tendons were not oriented parallel to each other. As indicated in Figure 5.15, the larger of the two simulated voids was visible in the thermal image. The large simulated void was approximately 2°C (3.6°F) cooler than the surrounding concrete, making the simulated void easy to distinguish compared to the rest of the subsurface features in the thermal image. The small simulated void was not distinguishable during testing of Specimen 7 using the silicone rubber heating blankets. The longitudinal rebar was visible, but the transverse rebar did not alter the surface temperature enough to be detected with the thermal camera.

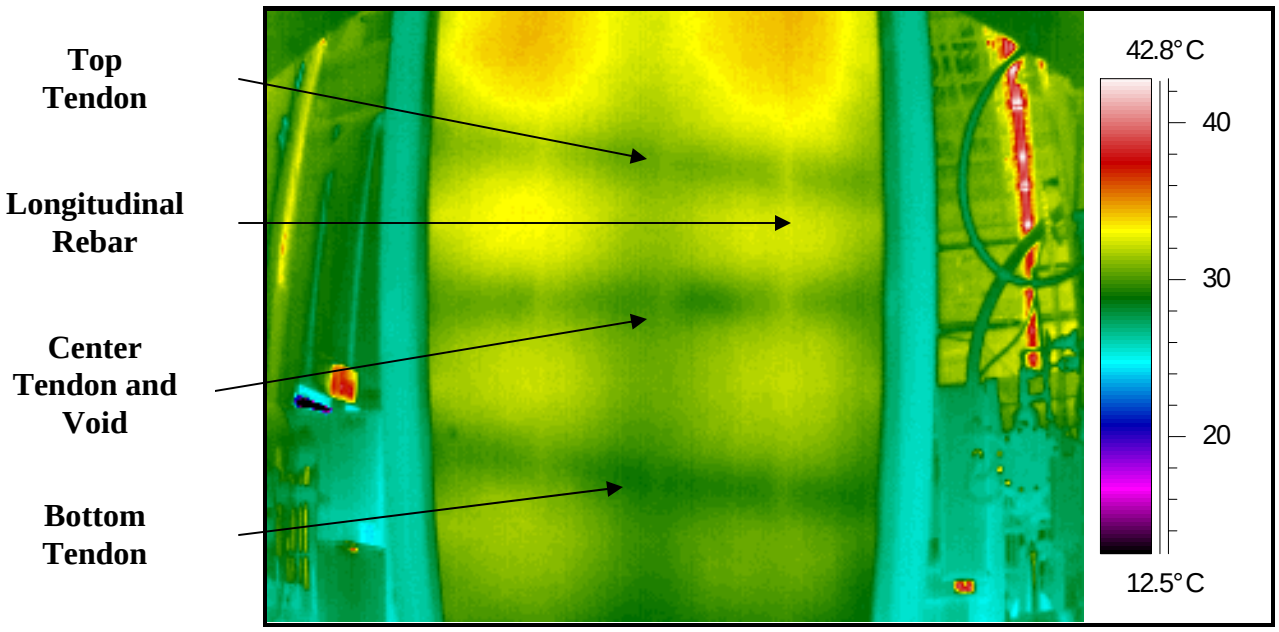


Figure 5.15 – Thermal image of Specimen 7 taken on October 14, 2005 at 2:00 P.M.

Testing resumed on Specimen 2 on October 17, 2005. Specimen 2 was tested with the heating blankets applied to the opposite surface heated during tests conducted on October 4th and October 6th. This test was conducted to see whether the results would be different when the simulated voids were located closer to the heated surface. The air temperature in the WMEL was an average of 24.4°C (76°F) throughout the day. The maximum temperature differential through the thickness of Specimen 2 was 30.5°C (55°F) after seven hours of heating. The heated surface of the specimen reached a maximum temperature of approximately 62.8°C (145°F).

Figure 5.16 is a thermal image showing Specimen 2 after being heated for seven hours with the silicone rubber flexible heating blankets. It can be seen that Figure 5.16 is similar to Figure 5.11. In both images, the large simulated void in the center of the specimen was clearly visible. The large simulated void in the center of the specimen was approximately 1.5°C (2.7°F) cooler than the surrounding concrete. The transverse rebar in Figure 5.16 was not as clear as in Figure 5.12, but was visible as indicated in the figure. The longitudinal rebar was not detected

during the tests conducted on October 17th. Also indicated in Figure 5.16, the location of the entire tendon was visible. As before, this was attributed to the low thermal conductivity of the HDPE duct and the four post-tensioning steel strands. As seen in previous images, the hot areas near the top of the specimen were visible due to uneven heating from the heating blankets. Neither the top nor bottom tendon was visible during this test.

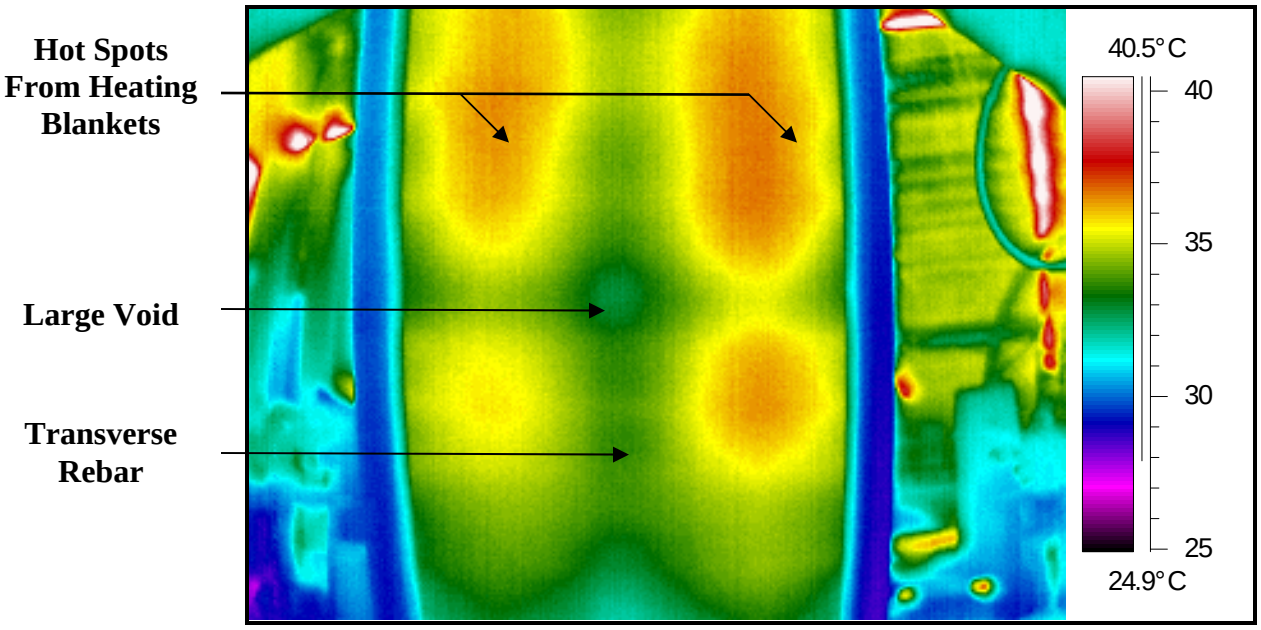


Figure 5.16 – Thermal image of Specimen 2 taken on October 17, 2005 at 4:00 P.M.

After the testing was concluded on Specimen 2 on October 17th, testing switched to the 30 cm (12 in) thick specimens. Specimen 4 was chosen because it contained the largest simulated void embedded in a 30 cm (12 in) thick specimen. On October 20th, the final testing using the silicone rubber heating blankets was conducted on Specimen 4. During the testing, the average air temperature inside the WMEL was 26.1°C (79°F). The maximum temperature differential through the thickness of the specimen was approximately 36.1°C (65°F) after ten hours of heating. The heated surface of the specimen reached a maximum temperature of approximately 65.6°C (150°F) at the end of the heating process.

Figure 5.17 is a thermal image taken of the unheated surface of Specimen 4 after the specimen was heated for approximately seven hours. Since the specimen is 10 cm (4 in) thicker than the 20 cm (8 in) thick specimens, a much larger temperature gradient was required to detect subsurface discontinuities. Since the applied temperature loading was the same magnitude as used on the 20 cm (8 in) thick specimens, the tendons and rebar did not appear as clearly. From the unheated surface, the smallest depth of concrete cover to a tendon was 10 cm (4 in). As indicated in Figure 5.17, the center tendon which only contained 20 post-tensioning steel strands appeared in the thermal image. As seen in Figure 5.17, there was a very faint distinction between the center tendon and the surrounding concrete. The location of the tendon appears approximately 0.6°C (1.1°F) cooler than the surrounding concrete. The top tendon with the four post-tensioning steel strands and a large simulated void embedded in a steel duct was not visible. The bottom tendon containing 30 steel strands embedded in a HDPE duct was also not detected. As indicated in the figure, the transverse rebar was detected on the surface in the top half of the specimen, but the longitudinal rebar was not detected. The cool region near the bottom of the specimen was attributed to the large bay door in the WMEL being open periodically, allowing the much cooler outside air to enter the laboratory and cool the specimen.

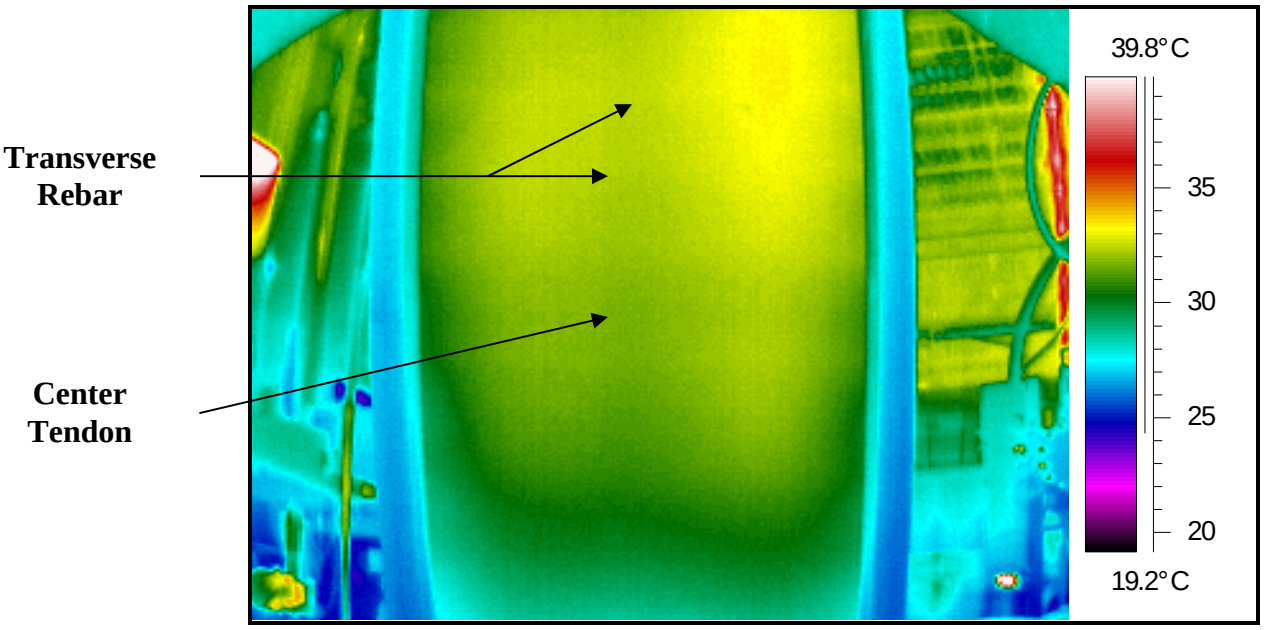


Figure 5.17 – Thermal image of Specimen 4 taken on October 20, 2005 at 5:30 P.M.

The thermal image in Figure 5.18 was taken approximately one hour and thirty minutes after the image in Figure 5.17 was taken. It can been seen in Figure 5.18 that the transverse rebar is much clearer in the center of the specimen, but near the edges of the specimen, warm spots masked the subsurface features. The longer the heating blanket was left in operation, the more pronounced the two warm vertical regions located on the left and right side of the specimen surface became. As previously mentioned, the mechanical thermostats were not precisely calibrated and allowed sections of the blanket to heat for longer periods of time. Since less heating occurred at the center of the specimen, cool regions as indicated in the figure appear and could be incorrectly construed as possible voids. As the warm spots on the surface became more pronounced, the center tendon observed earlier became less visible.

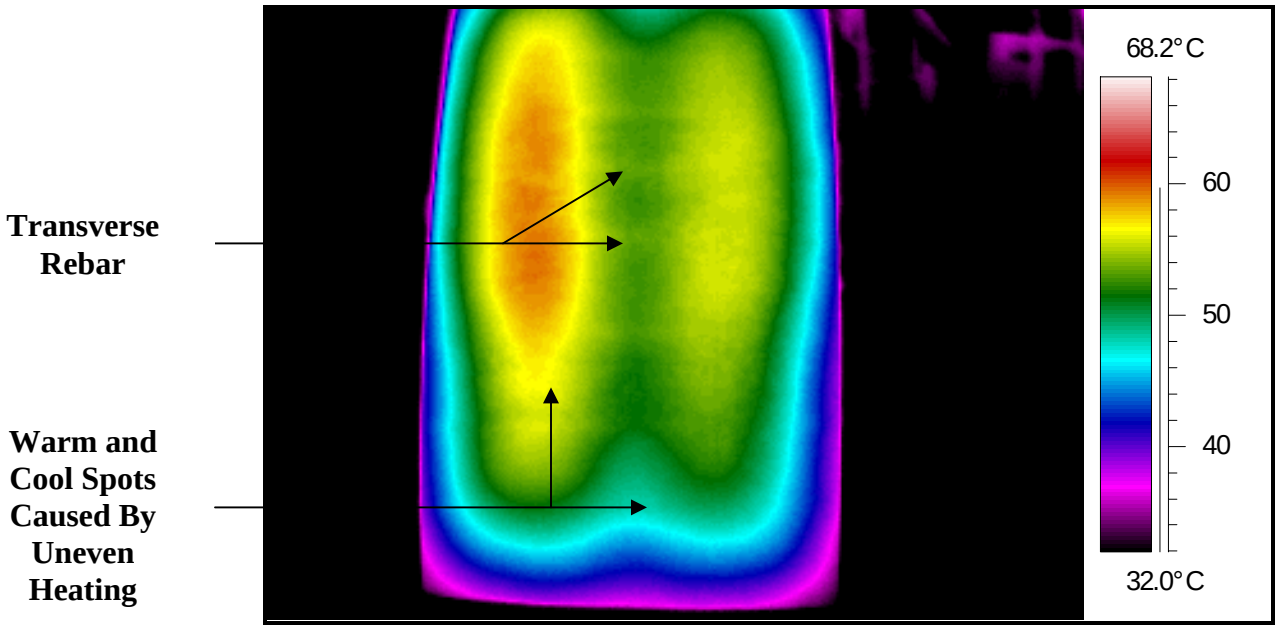


Figure 5.18 – Thermal image of Specimen 4 taken on October 20, 2005 at 7:00 P.M.

### 5.4 – Infrared Heater Results

After the testing involving the silicone rubber flexible heating blankets was completed, an infrared heater was used to heat one surface of the specimens to achieve the desired temperature differential. Tests using the infrared heater were also conducted inside the WMEL. Specimen 8 was chosen for the tests with the infrared heater since thermal testing had not been conducted on that specimen and it contained three HDPE post-tensioning ducts. Specimen 8 was also the only specimen constructed with a simulated void embedded in a HDPE duct in a 30 cm (12 in) thick specimen. Specimen 8 was the only specimen tested using the infrared heater.

On October 20, 2005, testing began on Specimen 8 using the infrared heater. The average air temperature inside the WMEL during the testing was 17.2°C (63°F). The maximum temperature differential through the thickness of the specimen was 75°C (135°F) after five hours of heating. The heated surface of the specimen reached a maximum temperature of 115.6°C

(240°F). Unfortunately, the infrared heater did not cover the entire specimen. Therefore, only the bottom 2/3 of the specimen was directly exposed to the infrared heater.

Figure 5.19 is a thermal image of Specimen 8 taken after approximately five hours of heating with the infrared heater. As indicated in Figure 5.19, the bottom and center tendons both appeared in the thermal image. Both tendons contained two simulated voids located at approximately the third points across the width of the specimen, but none of the simulated voids were detected. The concrete surface at the location of the tendons was approximately 0.5°C (0.9°F) cooler than the surrounding concrete. The tendons were not clearly seen in the thermal image because of the small temperature differences across the surface, but they were detected. Neither the transverse nor longitudinal rebar were visible in any of the thermal images. The top tendon was not visible during the testing conducted on October 26th.

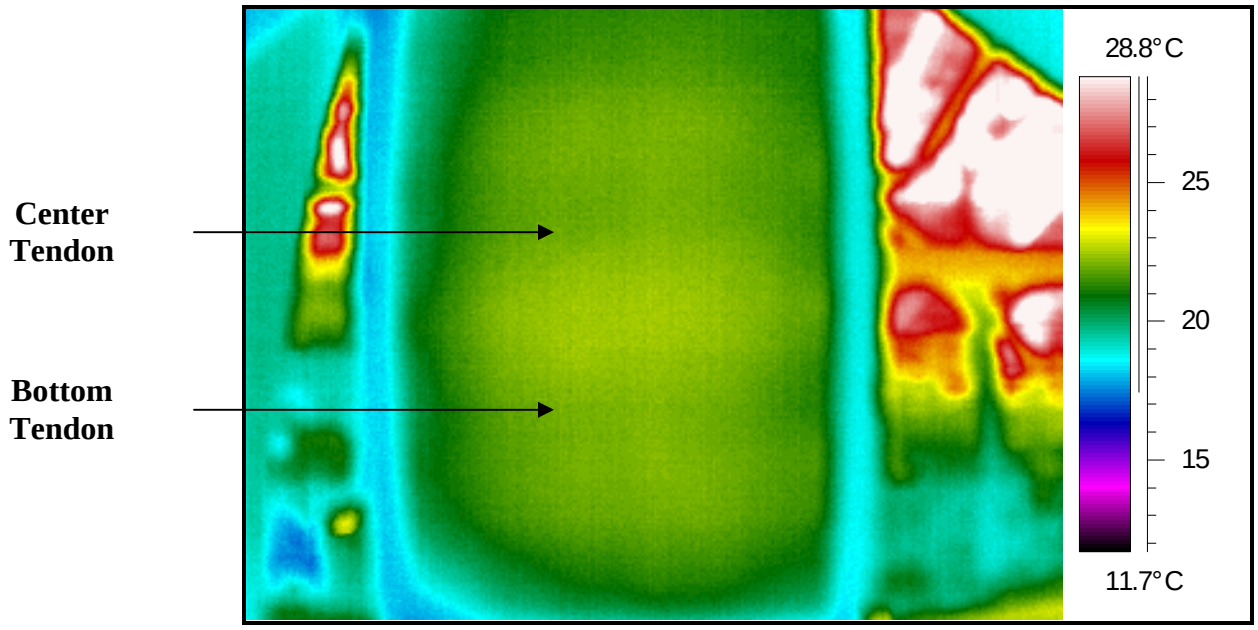


Figure 5.19 – Thermal image of Specimen 8 taken on October 26, 2005 at 1:00 P.M.

For the following test, Specimen 8 was orientated so the infrared heater was facing the opposite surface heated during tests conducted on October 26th. Specimen 8 was intended to

have equal amounts of concrete cover to each tendon, but the tendons shifted during construction. Instead of having 10 cm (4 in) of cover to each surface, the specimen actually had approximately 5 cm (2 in) of cover to one surface and 15 cm (6 in) of cover to the opposite surface for all three tendons. During testing conducted on October 26th, the specimen was situated so that the heat source was closest to the surface with the small depth of cover. The initial thermal image seen in Figure 5.19 was taken of the surface with 15 cm (6 in) of concrete cover. When the specimen was re-oriented on the wooden support frame, the thermal image was taken of the surface with 5 cm (2 in) of concrete cover and the heat source was applied to the surface with the 15 cm (6 in) depth of concrete cover.

On October 28th, the final test involving the infrared heater was conducted on Specimen 8. During the testing, the average air temperature inside the WMEL was 21.1°C (70°F). The maximum temperature differential through the thickness of the specimen was approximately 80.6°C (145°F) after approximately five hours of heating. The heated surface of the specimen reached a maximum temperature of 115.6°C (240°F). After the maximum temperature differential was achieved using the infrared heater after approximately five hours of heating, the temperature differential through the thickness stayed approximately the same. As the heated surface temperature rose, the opposite surface temperature rose at approximately the same rate.

In Figure 5.20, a thermal image of the unheated surface of Specimen 8 is shown after being heated for approximately five hours with the infrared heater. As indicated in Figure 5.20, the bottom and center tendons both appear clearly in the thermal image. Both the bottom and center tendons contained two simulated voids located approximately at the third points across the width of the specimen. Three of the four total simulated voids were detected as indicated in the figure. The location of the simulated voids were approximately 1.0°C (1.8°F) cooler than the

surrounding concrete. Neither the transverse nor longitudinal rebar were visible in any of the thermal images. During testing, the bottom half of the top tendon was visible, but the entire tendon was not because the heat source was not directed toward the top 1/3 of the specimen.

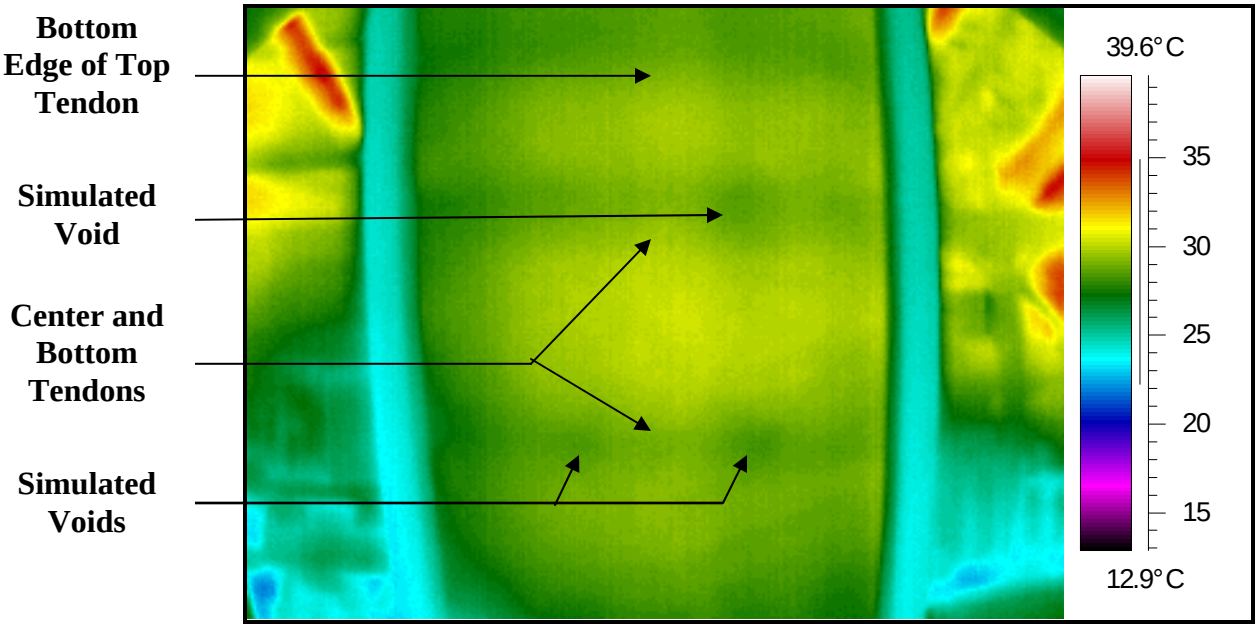


Figure 5.20 – Thermal image of Specimen 8 taken on October 28, 2005 at 12:00 P.M.

### 5.5 – Thermal Lag Measurements

Thermal lag is the amount of time for thermal energy to transfer through the entire thickness of a specimen. The thermal lag time for a 20 cm (8 in) thick specimen was determined by Pearson (2003) to be approximately 2.7 hours. From this information, the rate at which normal weight concrete conducts thermal energy was determined to be 7.5 cm/hour (3.0 in/hour) (Pearson, 2003).

During testing involving the various heating methods, internal features inside the 20 cm (8 in) thick specimens began to appear after approximately 2.5 hours. This was very close to the results obtained by Pearson (2003). Using the heat transfer rate for normal weight concrete determined by Pearson (2003), the time for thermal energy to travel through a 30 cm (12 in)

thick specimen was estimated at approximately four hours. During testing, the rebar and tendons in the 30 cm (12 in) thick specimens began to appear after approximately 3.5 hours. A thermal lag time of 3.5 hours for a 30 cm (12 in) thick specimen provides a rate of approximately 8.5 cm/hour (3.3 in/hour) for conducting thermal energy through normal weight concrete. This provided good correlation with Pearson's thermal lag predictions.

# Chapter 6 – Discussion of Results

## 6.1 – Analysis of Solar Heating and Air Conditioning Thermal Images

During the testing using solar heating and air conditioning, Specimen 1, Specimen 2, Specimen 3, and Specimen 7 were investigated. Each specimen will be discussed in numerical order in terms of their specimen designation number. When the description top, center, or bottom is used for the location of the tendons, this refers to the standing position as the specimens leaned against the test sheds.

Specimen 1 was 20 cm (8 in) thick and contained three steel post tensioning tendons. The top tendon contained 20 steel strands without a simulated void. The center tendon contained 30 steel post-tensioning strands without a simulated void. The tendon on the bottom of the specimen contained a 15 cm (6 in) long by 3.7 cm (1.5 in) thick simulated void and 30 steel strands. Since steel ducts and strands have a much higher value of thermal conductivity than normal weight concrete, it was expected that each tendon would increase the heat transfer through the specimen. The bottom tendon containing the simulated void should appear cooler than the other tendons because of the low thermal conductivity of the Styrofoam. Since the thermal energy should flow more readily through these regions of the specimen, each tendon should appear as cool line on the surface being heated. A warmer line should appear at the tendon locations on the unheated surface of the specimen.

Interior thermal images of the unheated surface of Specimen 1 are provided in Figure 5.3 taken on August 16$^{th}$, Figure 5.5 taken on August 21$^{st}$, and Figure 5.10 taken on September 8$^{th}$. In each of these images, the center tendon was visible and appeared at least 1.0°C (1.8°F) warmer than the surrounding concrete. Since the center tendon in Specimen 1 contained the

largest amount of steel, this was the result expected and predicted by the finite element models created for Specimen 1 seen in Figure 3.5. In each of the figures near the bottom of the specimen, a cool spot was observed at the location of the small simulated void in the bottom tendon. The entire length of the tendon was difficult to detect across the width of the specimen, but the cool spot was visible in each thermal image. This was expected since the Styrofoam would reduce the flow of thermal energy through the specimen in this location. The top tendon was not visible in any of the thermal images of the unheated surface taken from inside the test sheds. Warm areas near the top of the specimen near the location of the top tendon were observed, but were believed to be from uneven heating across the specimen. This was attributed to the edge heating that occurred from the solar energy along the top and sides of the specimen. This effect was minimized with the insulating borders that were created for each specimen, but was not reduced completely (see Figure 4.4).

The largest surface temperature difference obtained through the thickness of Specimen 1 was approximately 11.1°C (20°F) on August 21$^{st}$. The transverse rebar, and in some cases the longitudinal rebar, were visible with this temperature gradient. In the interior images of the unheated surface, the rebar produced faint lines 0.5°C (0.9°F) warmer than the surrounding concrete on the surface of the specimen. The increased temperature on the specimen surface caused by the rebar did not mask the thermal images of the tendons. Additionally, during construction of the specimens, the transverse rebar was placed along side the tendons rather than directly above or below the tendons. This construction practice helped minimize any masking effects caused by the rebar in the specimens.

Figure 5.6 taken on August 28$^{th}$ is an exterior thermal image of the heated surface of both Specimen 1 and Specimen 2. Specimen 2 was on the right in Figure 5.6. Three lines

approximately 1.0°C (1.8°F) cooler than the surrounding concrete were clearly seen spanning across the width of the Specimen 1. This was exactly what was predicted since the three tendons were more efficient in transferring thermal energy through the specimen than the surrounding concrete. The center tendon appeared colder than the other two tendons since the center tendon contained the most steel, and was the most efficient in transferring thermal energy. The top and bottom tendons appeared approximately the same temperature even though one contains more steel than the other. This was attributed to the edge heating increasing the temperature of the concrete near the top tendon making the top tendon appear warmer than expected. Since the steel strands inside the ducts were closer to the exterior heated surface (see Figure 6.1A), the locations of the tendons were slightly more distinct than the interior images of the unheated surfaces seen in Figures 5.3 and 5.10. Additionally, thermal energy in the steel strand would propagate along the length of the strands, reducing the overall thermal energy flowing through the thickness of the specimen. The longitudinal and transverse rebar were not visible in the exterior thermal images of the heated surface of Specimen 1. Additionally, the small simulated void in the bottom tendon was not visible in Figure 5.6. However, the camera was located farther from Specimen 2 in Figure 5.6 and the focus of the picture was over two specimens. If the thermal image had been solely of Specimen 1, the small simulated void would possibly be apparent because the large variation in the temperature of the surrounding would not be present as seen in Figure 5.6, which made small temperature variations hard to detect.

Specimen 2 was 20 cm (8 in) thick and contained two HDPE post tensioning ducts and one steel duct. The top steel duct contained four steel strands with a 15 cm (6 in) long by 8.5 cm (3.3 in) thick simulated void. The center tendon contained four steel post-tensioning strands also containing a 15 cm (6 in) long by 8.5 cm (3.3 in) thick simulated void. The tendon on the

bottom of the specimen was constructed with a HDPE duct and 30 steel strands with no simulated voids. Since the HDPE ducts have a much lower value of thermal conductivity than normal weight concrete, it was expected that each tendon containing a HDPE duct would decrease the heat transfer through the specimen at the tendon locations. The center and top tendons containing the simulated voids were expected to appear cooler than the other tendons because of the low thermal conductivity of the Styrofoam in both tendons and the HDPE duct in the center tendon. Since thermal energy should transmit less efficiently through these regions of the specimen, each tendon should appear as a warm line on the heated surface. A cooler line should appear on the unheated surface.

Figure 5.2 taken on August 16th, Figure 5.4 taken on August 21st, and Figure 5.7 taken on August 28th are interior thermal images of the unheated surface of Specimen 2. In all of these images, part of the center tendon and the simulated void embedded in the center duct were detected and appeared cooler than the surrounding concrete. In each image, the location of the simulated void was much cooler than surrounding concrete, indicating the Styrofoam reduced the heat flow through that location of the specimen as expected. The entire length of the center tendon was difficult to detect across the width of the specimen, but the cool spot was clearly visible in each thermal image. In Figure 5.7 near the top of the specimen, a faint cool spot was observed. This was probably the large simulated void embedded in the steel duct since the simulated void should reduce the transmission of thermal energy through the specimen. Since this cool spot was not visible during any other period of testing, there was no confirmation that the cool spot was indeed the large simulated void. The top tendon was not visible in any of the testing conducted on Specimen 2. It is likely that the small increase in heat transfer provided by only four steel strands placed in the duct was not significant enough to cause a distinguishable

temperature change on the surface of the specimen. The temperature profile plot seen in Figure 3.8 shows that for a 13.9°C (25°F) temperature differential through the thickness of the specimen, the top tendon should only appear 0.3°C (0.5°F) cooler than the surrounding concrete. Therefore, the results obtained from the experimental testing correlated well with the results obtained from the finite element model of Specimen 2.

The bottom tendon was also not clearly visible in any of the interior thermal images of the unheated surface of Specimen 2. Even though this tendon contained 30 post-tensioning steel strands, the strands were housed in a HDPE duct. The minimal overall temperature change was attributed to the reduction in heat transfer caused by the HDPE duct counter-balancing some of the increased heat transfer due to the large number of steel strands. Additionally, since the steel strands are not a continuous object inside the duct, small air pockets between each of the steel strands would reduce the heat transfer for the tendon. Furthermore, solar energy flowing through the edges of the specimen toward the cooler unheated surface helped mask any small temperature differences that might have appeared otherwise.

The largest surface temperature difference through the thickness of Specimen 2 was approximately 10.6°C (19°F) on August 21$^{st}$. With this temperature gradient through the thickness of the specimen, the simulated void inside the HDPE duct was easily detected. The transverse rebar was visible with this temperature gradient, but the longitudinal rebar was never detected. Since the longitudinal rebar had 1.6 cm (5/8 in) more concrete cover than the transverse rebar there was a greater distance for dissipation of thermal energy into the surrounding concrete, making the locations of the longitudinal bars undetectable.

Figure 5.6 taken on August 28$^{th}$ is an exterior thermal image of the heated surfaces of both Specimen 1 and Specimen 2. Specimen 2 was on the right in Figure 5.6. The large

simulated void in the center of Specimen 2 is clearly visible. The simulated void appears much warmer than the surrounding concrete. This was exactly what was predicted since the simulated void embedded in a HDPE duct did not transfer thermal energy as efficiently as the surrounding concrete. Warm regions next to the simulated void indicating the location of the center tendon were also visible. The center tendon was constructed with a HDPE duct and only four steel strands. The small amount of steel and the HDPE duct reduced the heat transfer through the specimen in this location because of the overall low thermal conductivity of the tendon. The top and bottom tendons were not visible in the exterior thermal image of the heated surface of Specimen 2. This trend was predicted by the finite element modeling for Specimen 2. According to Figure 3.8, the top tendon should appear 0.8°C (1.4°F) cooler and the bottom tendon should 1.5°C (2.7°F) warmer than the surrounding concrete according to the 93.3°C (200°F) applied temperature loading plot. Looking at the 37.8°C (100°F) applied temperature loading plot in Figure 3.8, the only tendon that should be detectable should be the center tendon. The top and bottom tendons were predicted to make less than a 0.2°C (0.4°F) change in the surface temperatures.

Specimen 3 was 30 cm (12 in) thick and contained three steel post tensioning ducts without any embedded simulated voids. The top and bottom tendons each contained 30 steel post-tensioning strands, and the center tendon contained 20 steel post-tensioning strands. The depth of cover varied for each tendon with the top tendon having 10 cm (4 in) of concrete cover, the center tendon having 7.5 cm (3 in), and the bottom tendon having 5 cm (2 in) of cover to the heated surface. Since steel ducts and strands have a much higher value of thermal conductivity than normal weight concrete, it was expected that each tendon would increase the heat transfer through the specimen according to Figure 3.10. In exterior thermal images of the heated surface

of Specimen 3, it was shown in Figure 3.10 that the bottom tendon should appear the coldest of the three tendons since it was closest to the heated surface. Since the center tendon contained on 20 steel strands, it was predicted from the finite element model of Specimen 2 that the center tendon would cause the smallest temperature changes on the specimen surfaces. In images of the unheated surface, the top tendon should appear the warmest since it contained 30 steel strands and was closest to the unheated surface. Since the tendon had the smallest concrete cover to the unheated surface, there was less cool concrete for thermal energy dissipation.

Figure 5.8 taken on August 28$^{th}$ is a thermal image of the heated surface of the bottom half of Specimen 3. The bottom tendon was visible in the thermal image. This was the only tendon detected in the exterior images taken of Specimen 3. This was expected according to the temperature profile of Specimen 3 in Figure 3.10. The results of the finite element model of Specimen 3 indicate the tendon with the smallest concrete cover should have the largest temperature variation between the location of the tendon and the surrounding concrete. The bottom tendon had the smallest concrete cover to the heated surface and was the only tendon detected. As predicted, this tendon appeared cooler than all of the other tendons. In all of the exterior thermal images, the longitudinal and transverse rebar were not detected in Specimen 3. This could be attributed to the rebar cage shifting during construction, causing greater concrete cover to the rebar than anticipated.

None of the rebar or tendons were visible in interior images of the unheated surface of Specimen 3 with the temperature differential achieved across the thickness of the specimen. The largest surface temperature differential through the thickness of Specimen 3 obtained was approximately 12.2°C (22°F) on August 21$^{st}$. With the large concrete cover from the tendons to the unheated surface, the temperature differential was not sufficient to detect the subsurface

conditions. The only tendon visible was the bottom tendon in the exterior image of the heated surface because the bottom tendon had only 5 cm (2 in) of concrete cover to the heated surface.

Specimen 7 contained three HDPE post tensioning ducts. Each of the HDPE ducts contained 20 post-tensioning steel strands. The top tendon contained 20 post-tensioning steel strands without a simulated void. The center duct contained two simulated voids located at approximately the third points across the width of the specimen. The tendon on the bottom of the specimen contained 20 corroded post-tensioning steel strands and no simulated voids. The temperature profile for Specimen 7 seen in Figure 3.18 indicated the center tendon would transfer less thermal energy because of the simulated voids. The top and bottom tendons were predicted to transfer more thermal energy than the surrounding concrete and thus appear cooler on the heated surface. Therefore, on the heated surface, the top and bottom tendons should appear as cool lines and the center tendon should appear as a warm line with two warmer spots due to the simulated voids.

Figure 5.9 taken on September 7$^{th}$ is an exterior thermal image of the heated surface of Specimen 7. Near the bottom of the specimen there was a warm line spanning the width of the specimen at the location of the bottom tendon. As seen in Specimen 2, the HDPE ducts reduced the transmission of thermal energy through the specimen. The finite element models predicted that the bottom tendon would be approximately 0.8°C (1.4°F) cooler than the surrounding concrete with a 13.9°C (25°F) temperature differential through the thickness of the specimen. One explanation for this discrepancy is that the steel strands in the specimens were modeled as solid sections of steel rather than individual strands. Thus, the small air voids and grout between each steel strand were not addressed in the model. The air voids in particular would reduce the

transfer of thermal energy through the specimen because of the lower value of thermal conductivity for air.

Near the center of Specimen 7, a warm line spanning across the specimen with two warmer spots was shown in Figure 5.9. These two warm spots were in the locations of the simulated voids in the center tendon. These warm spots appeared as predicted since they were less efficient in transferring thermal energy through the specimen than the surrounding concrete. In most of the exterior thermal images of the heated surface of Specimen 7, the temperature variations across the surface of the specimen made obtaining high-quality thermal images difficult. This was due to reflection of sunlight from the specimen surface due to the varying surface texture and emissivity of the concrete. The same difficulty was observed by Pearson (2003).

Near the top of Specimen 7, a warm line extending approximately half way across the width of the specimen was detected at the location of the top tendon. Specimen 7 did not have a uniform cross-sectional thickness and was thinner in the location where the warm line disappeared. This was probable since the thermal image shows the region near the top specimen to be cooler than in other areas on the surface of the specimen. These cooler temperatures made the entire location of the top tendon difficult to detect. Additionally, during each day of testing the average unheated surface temperatures of Specimen 7 were approximately 0.8°C (1.5°F) warmer than the unheated surface of the other 20 cm (8 in) thick specimens. This would indicate that the thermal energy was flowing more efficiently through Specimen 7 than the other 20 cm (8 in) thick specimens.

The largest surface temperature difference through Specimen 7 was approximately 7.8°C (14°F) on August 21$^{st}$. The longitudinal and transverse rebar were not visible with this

temperature gradient. This could be attributed to the rebar cage shifting during construction causing the actual concrete cover to be larger than expected. Also, the rebar used in Specimen 7 and Specimen 8 had a 0.32 cm (1/8 in) smaller diameter than the rebar used in the other six previously constructed specimens. These smaller steel bars had less effect on heat flow through the specimen.

### 6.2 – Analysis of Silicone Rubber Heating Blanket Thermal Images

During the testing using the electric silicone rubber flexible heating blankets, Specimen 1, Specimen 2, Specimen 4, and Specimen 7 were investigated. Each specimen will be discussed in numerical order in terms of their specimen designation number.

As discussed in Section 6.1, the center tendon of Specimen 1 should appear as a warm line on the unheated surface of the specimen because of the 30 post-tensioning steel strands located inside a steel duct. The bottom tendon was expected to also appear as a warm line on the unheated surface except at the location of a small simulated void. This simulated void should reduce the flow of thermal energy through the specimen resulting in a cool spot appearing on the unheated surface. The top tendon should appear cooler than the other two tendons because of the smaller number of steel strands inside the duct. Thermal images of the unheated surface of Specimen 1 are shown in Figure 5.13 taken on October 10$^{th}$ and Figure 5.14 taken on October 11$^{th}$. As predicted, the center tendon appears at least 1.5°C (2.7°F) warmer than the surrounding concrete. Comparing these temperature values with those obtained from tests conducted using solar heating on Specimen 1, the heating blankets increased the temperature difference between the location of the center tendon and the surrounding concrete by approximately 0.5°C (0.9°F).

The top tendon in Specimen 1 appears approximately 0.5°C (0.9°F) cooler than the center tendon in the thermal images. This was expected since the top tendon contains ten fewer steel strands than the center tendon. Heat transfer though the top tendon was not as efficient as in the center tendon, resulting in the top tendon appearing cooler than the center tendon from the unheated surface of the specimen. The top tendon was not detected on the unheated surface of Specimen 1 during any tests conducted using solar heating and air conditioning due to edge heating along the top edge of the specimen.

In the thermal images obtained from heating Specimen 1 with the heating blankets (see Figures 5.13 and 5.14), the simulated void in the bottom tendon was not visible, although it was detectable in the previous solar heating tests (see Figures 5.3 and 5.5). A cool line extending vertically down the center of the specimen can be seen in Figures 5.13 and 5.14. This was caused by uneven heating from the heating blankets due to the independent thermostat controls for individual sections of the blankets. The sections of the blanket near the center of the specimen shut down earlier than the other sections of the blanket. This resulted in the center strip of the specimen being cooler than the rest of the specimen. This cooler temperature propagated through the specimen causing a cool strip on the unheated surface of the specimen. This cool strip was in the exact location of the small simulated void in the bottom tendon. Since the small simulated void caused a small temperature difference on the surface, it was masked by the cool strip caused by the heating blankets.

The largest surface temperature difference obtained through the thickness of Specimen 1 using the silicone rubber heating blankets was approximately 33.3°C (60°F) on October 10$^{th}$. The transverse rebar was visible with this temperature gradient but the longitudinal rebar was not. This result was also observed in the solar heating tests (see Figures 5.3, 5.5, and 5.10).

Previous results for Specimen 2 during solar heating tests showed that the center tendon containing the large simulated void embedded in the HDPE duct caused a 2°C (3.6°F) decrease in the surface temperature of the concrete, due to reduced flow of thermal energy through the specimen. The top and bottom tendons were not detected during the testing using solar heating. As seen in Figure 3.8, it was expected that the bottom tendon would appear slightly warmer than the surrounding concrete on the unheated surface while the top tendon should appear slightly cooler than the surrounding concrete because it contained a small simulated void.

Thermal images of the unheated surface of Specimen 2 are provided in Figure 5.11 taken on October 4$^{th}$ and Figure 5.12 taken on October 6$^{th}$. The low thermal conductivity of the large simulated void and HDPE duct reduced the flow of thermal energy through the thickness of the specimen, making the center tendon and simulated void clearly visible. In both thermal images, the bottom tendon containing the HDPE duct and 30 post-tensioning steel strands was not visible. The insulating characteristics of the HDPE ducts counteracted the high thermal conductivity of the steel strands causing very little change in surface temperatures.

The top tendon in Specimen 2 was also not visible during the testing using the heating blankets. Part of the problem detecting the tendon was because of hot spots near the top of the specimen caused by uneven heating from the heating blankets. These hot spots on the unheated surface of the specimen were in the same location across the width of the specimen as the sections of the heating blankets that stayed in operation longer. The hot spots made it difficult to detect the small temperature changes with the thermal camera because of the large temperature variation over the width of the specimen.

The largest surface temperature difference through the thickness of Specimen 2 obtained using the silicone rubber heating blankets was approximately 38.9°C (70°F) on October 6th. The transverse rebar was visible with this temperature gradient but the longitudinal rebar was not.

To investigate the effects of heating the specimen from either surface, Specimen 2 was rotated so the heating blankets were applied on the surface closest to the simulated voids in the tendons (see Figure 3.2). This orientation mimicked the orientation used in finite element modeling (see Figure 3.4). In this orientation, the simulated voids were closer to the heat source, so the thermal energy encountered the simulated voids before the steel strands. In either orientation, the center tendon with the large simulated void should appear as a cool region with a colder spot directly in the center of the specimen. However, the unheated surface temperatures could vary due to the difference in concrete cover to the post-tensioning steel strands and simulated voids for the two orientations.

Figure 5.16 taken on October 17th was a thermal image taken of the unheated surface of Specimen 2 orientated so the simulated voids were closer to the heated surface. Comparing Figure 5.16 to Figure 5.11, the large simulated void in the center of the specimen was clearly visible because of the reduced flow of thermal energy through the simulated void. In both orientations, the large simulated void reduced the surface temperature of the specimen by approximately 2°C (3.6°F). The location of the center tendon was visible across the majority of the width of the specimen in both thermal images. This was due to the low thermal conductivity of the HDPE duct and the four post-tensioning steel strands reducing the amount of heat conducted through the specimen. Once again, the hot areas near the top of the specimen were visible from uneven heating caused by the heating blankets. These hot spots made it difficult to detect the top tendon.

The largest surface temperature difference obtained through the thickness of Specimen 2 was approximately 33.3°C (60°F) during testing conducted on October 17th. The transverse rebar embedded in Specimen 2 seen in Figure 5.16 caused a 0.3°C (0.5°F) smaller temperature difference between the location of the rebar and the surrounding concrete compared to Figure 5.11, but was visible as indicated in the figure. The longitudinal rebar was not detected.

Specimen 4 was 30 cm (12 in) thick and contained two HDPE post tensioning ducts and one steel duct. The top steel duct contained a large simulated void and four post-tensioning steel strands. The center HDPE duct contained 20 steel strands and no simulated voids. The tendon on the bottom of the specimen was constructed with a HDPE duct and 30 steel strands. It was expected that the top tendon should appear as a cool line with a small cold spot near the center of the specimen designating the location of the large simulated void on the unheated surface of the specimen. The center tendon was expected to appear cooler than the bottom tendon because it only contained 20 steel strands and was 2.5 cm (1 in) farther from the unheated surface than the bottom tendon containing 30 steel strands.

Figures 5.17 and 5.18 taken on October 20th are thermal images of the unheated surface of Specimen 4. It can be seen that the simulated voids and the location of the tendons were more difficult to detect in the 30 cm (12 in) thick specimen than the 20 cm (8 in) thick specimens. The center tendon with 12.5 cm (5 in) of concrete cover was the only tendon visible in the specimen. The 20 steel strands and the insulating properties of the HDPE duct reduced the flow of thermal energy through the specimen in that location compared to the bottom tendon. The large depth of concrete cover allows thermal energy to dissipate into the cooler concrete as it flows through the specimen. Even with this occurring, the center tendon was still visible as indicated in Figure 5.17.

The largest surface temperature difference obtained through the thickness of Specimen 4 was approximately 36.1°C (65°F) utilizing the silicone rubber heating blankets. With this temperature difference, the top and bottom tendons were not visible in any of the images. As discussed previously, the bottom tendon was not visible because of the HDPE duct insulating the post-tensioning steel strands. The top tendon should have appeared cooler than the surrounding concrete with a cool spot half way across the width of the specimen indicating the location of the large simulated void. The uneven temperature distribution near the bottom of the specimen caused by uneven heating from the heating blankets and convection cooling from the cool laboratory air masked the bottom tendon. Another reason for these tendons not being visible was that a large temperature gradient was required through the thickness of the specimen. The results from the finite element models for the 30 cm (12 in) thick specimens indicated that a temperature differential of 51.7°C (125°F) would be required to detect the subsurface discontinuities. The temperature differential through the thickness of Specimen 4 during experimental testing was approximately 36.1°C (65°F).

As the heating blankets were in operation throughout the day, increasing temperature variations on the unheated surface of the specimen would appear. This was attributed to thermal energy propagating through the specimen unevenly caused by the uneven heat output from the heating blankets. Comparing Figure 5.18 to Figure 5.17 taken approximately one hour and thirty minutes earlier, large warm spots in Figure 5.18 can be seen. These large warm spots masked the presence of the center tendon. The only benefit of heating the specimen for this length of time was the transverse rebar became more clear near the center of the specimen.

Specimen 7 was 20 cm (8 in) thick and contained three HDPE post tensioning ducts, each containing 20 post-tensioning steel strands. As seen in previous testing, each of the tendons was

expected to reduce the flow of thermal energy through the specimen. The center duct contained two simulated voids located approximately at the third points across the width of the specimen. Therefore, on the unheated surface, the top and bottom tendons should appear as cool lines and the center tendon should appear as a cool line with two colder spots located at the third points.

Figure 5.15 taken on October 14th is a thermal image of the unheated surface of Specimen 7. Each tendon appeared as a cool line across the width of the specimen. The location of the larger simulated void in Specimen 7 was detected, appearing as a cool spot along the cool line representing the center tendon. The HDPE ducts reduced the heat transfer through the specimen because of their low thermal conductivity. Since each tendon contained the same size HDPE ducts, the same depth of concrete cover, and the same number of post-tensioning steel strands, each tendon appeared approximately 1.5°C (2.7°F) cooler than the surrounding concrete because each tendon reduced the flow of thermal energy by the same amount. The largest surface temperature difference obtained through the thickness of Specimen 7 was approximately 30.5°C (55°F). None of the transverse rebar was visible with this temperature differential.

### 6.3 – Analysis of the Infrared Heater Thermal Images

Specimen 8 was analyzed during testing using the infrared heater. The specimen was heated in two orientations on the wood support frame. In one orientation, the infrared heater was used to heat the surface closest to the simulated voids in the specimen (see Figure 3.2). For the other orientation, the specimen was rotated on the wood support frame and the infrared heater was used to heat the surface closest to the post-tensioning steel strands in the specimen (see Figure 3.2).

Specimen 8 was 30 cm (12 in) thick and contained three HDPE post-tensioning ducts, each having 10 cm (4 in) of concrete cover to each surface. The top and middle tendons each contained 20 post-tensioning steel strands and the bottom tendon contained 30 steel strands. The bottom and center tendon each contained two simulated voids. Since center and top tendons only contained 20 steel strands, the location of these tendons was expected to appear the cooler than the location of the bottom tendon on the unheated surface. The center and bottom tendons should appear as cool lines with two colder spots located at the third points across the width of the specimen.

Figure 5.19 is a thermal image taken of the unheated surface of Specimen 8 on October 26$^{th}$. On the 26$^{th}$, the specimen orientation matched the orientation used when Specimen 8 was modeled with finite elements (see Figure 3.20). The simulated voids were situated closer to the heated surface than the steel strands. In Figure 5.19, the center and bottom tendons appear as cooler regions extending across the specimen. The top tendon was not visible because the infrared heater was not large enough to direct the heat over all three tendons. The heat source was centered over the bottom and center tendons since these tendons contained simulated voids. The simulated voids in the center and bottom tendons were not visible in Figure 5.19. The location of the bottom tendon was 0.3°C (0.5°F) cooler than the surrounding concrete. The location of the center tendon was 0.8°C (1.4°F) cooler than the surrounding concrete. This was expected since the center tendon contained ten fewer post-tensioning steel strands than the bottom tendon and should appear colder. The lower overall thermal conductivity of the center tendon reduced the heat flow through the specimen more significantly than the bottom tendon. In all of the previous cases, the HDPE duct insulated the 30 post-tensioning steel strands, causing no detectable change in temperature on the specimen surface. According to Figure 3.20, as the

temperature gradient through the thickness of Specimen 8 increased, the temperature difference between the location of the bottom tendon and the surrounding concrete increased. Using the infrared heater, the temperature gradient through the thickness of a 30 cm (12 in) thick specimen was 83.3°C (150°F) while the maximum temperature gradient through the thickness of a 30 cm (12 in) thick specimen was 36.1°C (65°F) when the heating blankets were used. Therefore, it was determined that the increased temperature gradient through the thickness of Specimen 8 made the detection of the bottom tendon constructed with 30 post-tensioning steel strands and a HDPE duct possible.

Instead of having 10 cm (4 in) of cover to each surface, the specimen actually had approximately 5 cm (2 in) of cover to one surface and 15 cm (6 in) of cover to the opposite surface (see Table 3.1). When the specimen was orientated so the simulated voids were closest to the heated surface, Specimen 8 actually had 15 cm (6 in) of concrete cover between the duct and the unheated surface. This is a significant distance of concrete to allow the thermal energy to dissipate as it propagates through the specimen. This is one reason why the tendons appeared faint and the voids were not visible in Figure 5.19.

The maximum temperature gradient achieved through the thickness of Specimen 8 on October 26$^{th}$ was approximately 83.3°C (150°F). This large temperature gradient was not large enough to make the transverse and longitudinal rebar visible. With this temperature gradient, the location of the center tendon that contained 20 post-tensioning steel strands with 15 cm (6 in) of concrete cover was detected. Additionally, the location of the bottom duct containing 30 post-tensioning steel strands with 15 cm (6 in) of concrete cover was detected. Reviewing the results from the finite element model for Specimen 8 in Figure 3.20, it was predicted that a temperature

differential of approximately 166.7°C (300°F) was required across the thickness to create a 0.3°C (0.5°F) temperature change at the location of the transverse rebar.

Figure 5.20 was a thermal image taken of the unheated surface of Specimen 8 on October 28th. The specimen was orientated so the post-tensioning steel strands were closest to the heated surface. The depth of concrete cover to the tendons from the unheated surface was only 5 cm (2 in). This was the same depth of cover achieved in the 20 cm (8 in) thick specimens.

In Figure 5.20, both the bottom and center tendons are clearly visible in the thermal image and appear approximately 1°C (1.8°F) cooler than the surrounding concrete. Since the temperature dissipation in 5 cm (2 in) of concrete cover was minimal, the tendons were clearly identifiable in the thermal image. Near the top of the specimen in Figure 5.20, a distinct temperature transition is visible. This was the half of the top tendon appearing in the thermal image. Since the heat from the infrared heater was not focused on the top tendon, the entire tendon was not visible.

Three of the four simulated voids were detected in the bottom and center tendons in Figure 5.20. The only void not visible was the 5 cm (2 in) long by 5.2 cm (2.1 in) thick simulated void located on the left side of the center tendon. The 5 cm (2 in) long by 5.2 cm (2.1 in) simulated void was not detected because the temperature gradient was smaller near the center tendon since a majority of the thermal energy from the infrared heater was focused toward the bottom tendon.

The maximum temperature gradient obtained through the thickness of Specimen 8 was approximately 80.6°C (145°F) on October 28th. With this temperature gradient, the transverse and longitudinal rebar were not visible. As mentioned previously, the smaller diameter bars used in the specimen did not provide a large enough increase in thermal conductivity to make the bars

visible in the thermal images with these temperature differentials. This large temperature gradient was similar to the gradient obtained on the 26th, yet the images on the 28th appear much clearer. This is significant evidence that the depth of cover to the tendons in each specimen has a large effect on the resulting thermal images.

### 6.4 – Summary

When the 20 cm (8 in) thick specimens were constructed with HDPE ducts containing small amounts of post-tensioning steel, the temperature differences in the thermal image were the easiest to detect. The large simulated void embedded in a HDPE duct filled with only four steel strands seen in Specimen 2 was the easiest to detect (see Figure 5.4). This 15 cm (6 in) long by 8.5 cm (3.3 in) thick simulated void caused a surface temperature difference of approximately 2.0°C (3.6°F).

HDPE ducts containing 30 post-tensioning steel strands were more difficult to detect. The high thermal conductivity of the steel strands was offset by the low thermal conductivity of the HDPE ducts. Instead of reducing the flow of thermal energy through the specimen as seen with the HDPE ducts containing four strands, the HDPE duct containing 30 steel strands in Specimen 2 had a higher overall thermal conductivity and was not distinguishable from the surrounding concrete. This resulted in much smaller and in some cases undetectable temperature differences on the surface of the specimen.

Predictions were made based on the finite element models that the 20 steel strands embedded in a HDPE duct would increase the overall thermal conductivity of the tendon, increasing the heat transfer through these tendons (see Figures 3.12, 3.18, and 3.20). However, tendons containing 20 steel strands enclosed in a HDPE duct actually reduced the flow of

thermal energy through the specimen. Since there are small air voids and grout between each of the steel strands, the overall increase in heat transfer was not as large as anticipated in the finite element models. The small air voids and grout between the steel strands were not accounted for in the modeling. As seen during testing of Specimen 7, each tendon containing 20 post-tensioning steel strands appeared cooler than the surrounding concrete when the thermal image was taken of the unheated surface.

Steel ducts containing 30 steel strands in 20 cm (8 in) thick specimens were relatively easy to detect because of the increased thermal conductivity of the system. This increase in thermal conductivity increased the surface temperature of the unheated surface. Specimen 1 included a steel duct containing 30 steel strands and a small simulated void. This small simulated void was detected during the testing because it reduced the heat transfer through the tendon in that location. Since the surrounding area had an elevated temperature because of the high thermal conductivity of the steel strands and duct, the cool spot cause by the simulated void was easily detected.

Tendons constructed with steel ducts containing fewer than 30 steel strands were harder to distinguish (see Figure 5.3). Specimen 1 contained a steel duct filled with 20 steel strands. This tendon was detected, but was difficult because of the smaller temperature difference produced compared to the steel ducts containing 30 steel strands (see Figure 5.6). Steel ducts containing just four post-tensioning steel strands could not be detected during the research. The only steel duct containing four steel strands and a large simulated void was located at the top of Specimen 2. The 15 cm (6 in) long by 8.5 cm (3.3 in) thick simulated void and small number of steel strands should have reduced the thermal conductivity of the specimen at the location of the top tendon. In actuality, it appeared that the high thermal conductivity of the four post-

tensioning steel strands and the steel duct was offset by the low thermal conductivity of the simulated void, resulting in a minimal temperature change on the unheated specimen surface at the location of the top tendon.

After the bridge is tensioned, the steel strands will be forced into the top or bottom of the duct. As discussed by Pearson (2003), any voids that occur in a post-tensioning duct will occur above or below the steel strands. When the specimens used in this research were constructed, they were placed flat on the ground when the steel strands and grout were inserted. When the specimens were then placed on edge during testing, the void-steel orientation was similar to what is shown in Figure 6.1A. In the test specimen configuration, the thermal energy would flow through the void and the steel strands sequentially. This situation is not completely identical to a typical vertical post-tensioned concrete bridge wall. In a typical box girder bridge web, the void-steel configuration would be similar to Figure 6.1B.

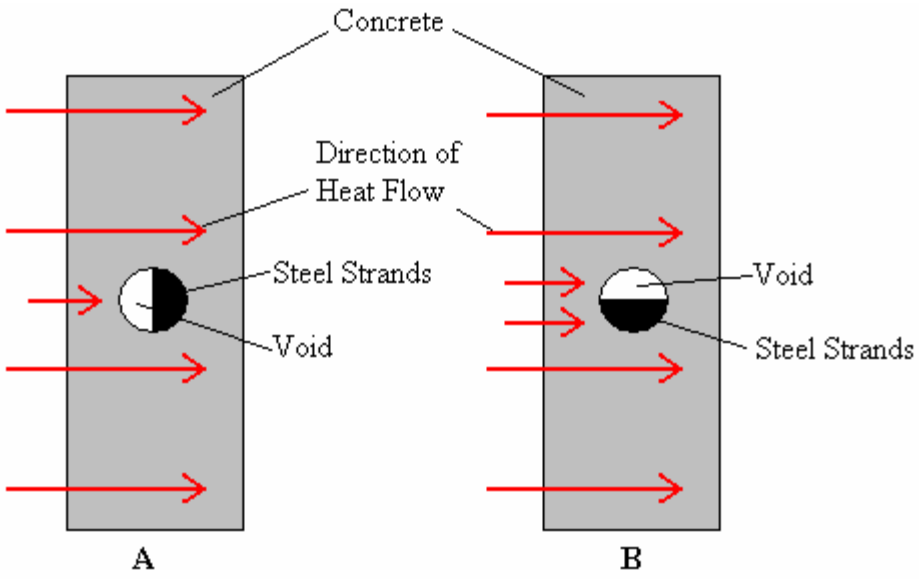


Figure 6.1 – Steel strand orientation inside post-tensioning ducts for A) specimens in this study, and B) typical box girder bridge wall (Pearson, 2003)

In an actual bridge configuration, the voids should be easier to detect. As seen in Figure 6.1B, a portion of the thermal energy would flow only through the air void embedded in the post-tensioning duct. Since air has a thermal conductivity very similar to the Styrofoam used in the test specimens, the flow of thermal energy should be reduced compared to thermal energy flowing through a configuration similar to Figure 6.1A, making it easier to detect voids in ducts in typical post-tensioned bridge walls. In a configuration similar to Figure 6.1A, thermal energy propagating through the thickness of the specimen would flow through a portion of the simulated void and the post-tensioning steel strands. The reduced flow of thermal energy through the simulated void would be increased when the thermal energy propagated through the post-tensioning steel strands.

Simulated voids ranging from 5 cm (2 in) in length to 15 cm (6 in) in length were detected during the research. These simulated voids were between 3.5 cm (1.4 in) and 6.2 cm (2.4 in) thick. All of these simulated voids were detected in specimens where the concrete cover to the surface being viewed was less than 10 cm (4 in). Most of the simulated voids detected had approximately 5 cm (2 in) of concrete cover. This was a valuable finding since voids are locations where corrosion of the post-tensioning steel strands may occur.

The transverse rebar and, in some cases, longitudinal rebar were visible in the thermal images of the 20 cm (8 in) thick specimens. The No. 5 rebar used in specimens constructed by Pearson (2003) was easier to detect than the No. 4 rebar used in the specimens constructed by Conner (2004). The rebar did not interfere with the detection of tendons and simulated voids in any specimens. Pearson (2003) also noted that the rebar did not appear to affect thermal images in his research. This is beneficial since rebar is often placed in close proximity to the tendons.

The locations of some simulated voids and tendons were detected in tests conducted on the 30 cm (12 in) thick specimens. The locations of steel ducts containing 30 steel strands were detected with a temperature differential of approximately 11.1°C (20°F) in a 30 cm (12 in) thick specimen. The depth of cover to this tendon was only 5 cm (2 in), but the location of the tendon was visible. The location of tendons in a 20 cm (8 in) thick specimen containing a steel duct filled with 30 steel strands were easier to distinguish compared to the 30 cm (12 in) thick specimen. The 30 cm (12 in) thick specimens required more thermal energy to heat the larger volume of concrete.

When a temperature differential of 33.9°C (61°F) was achieved in a 30 cm (12 in) thick specimen, the location of a HDPE duct filled with 20 steel strands under 12.5 cm (5 in) of concrete cover was detected (see Figure 5.17). When the infrared heater provided a temperature differential of 75°C (135°F), a HDPE duct filled with 20 steel strands was also detected in a 30 cm (12 in) thick specimen (see Figure 5.19). This duct had 15 cm (6 in) of concrete cover because the duct shifted toward one surface of the specimen during construction.

Overall, with a temperature gradient of approximately 11.1°C (20°F), tendons with less than 5 cm (2 in) of concrete cover can be detected in 20 cm (8 in) thick specimens. HDPE ducts containing 30 steel strands and steel ducts containing four steel strands are very difficult to detect. Detecting these subsurface discontinuities at greater depths of cover requires larger temperature differentials. HDPE ducts containing four steel strands and steel ducts containing 30 steel strands were the easiest to detect with an 11.1°C (20°F) temperature differential achieved through the thickness of the specimens.

The 30 cm (12 in) thick specimens require much larger temperature gradients to detect the location of voids and tendons. Only the tendons that caused the largest difference in heat

flow through the specimen were visible. In a 30 cm (12 in) specimen, tendons were detected with concrete cover depths up to 15 cm (6 in) with at least a 75°C (135°F) temperature gradient. Simulated voids were detected in the tendons with 5 cm (2 in) of concrete cover and smaller at these temperatures. Even with the large temperature differentials, only the transverse rebar constructed from No. 5 bars were detected in the 30 cm (12 in) thick specimens.

In conclusion, it can be seen that the depth of cover has a large influence on the ability to detect subsurface conditions in post-tensioned bridge walls. It was shown that a 30 cm (12 in) thick specimen containing tendons with 5 cm (2 in) of concrete cover can be clearly detected. Simulated voids ranging in size from 5 cm (2 in) long by 3.7 cm (1.5 in) thick to 10 cm (4 in) long by 5.2 cm (2.1 in) thick were detected in this thicker specimen. The thickness of the specimen has an effect on the ability to detect the location of tendons and simulated voids in thermal images. The thicker specimens require more thermal energy to be heated to the required temperature gradient. For thicker specimens, there is more surrounding concrete for thermal energy dissipation, which makes subsurface conditions more difficult to detect.

# Chapter 7 – Conclusions

## 7.1 – Accomplishment of Objectives

Two-dimensional finite element models were developed to model heat flow through concrete specimens with embedded prestressing tendons. Various temperature loadings and boundary conditions we applied to the models to mimic actual testing conditions. The temperature trends observed for the different tendons embedded in each specimen were similar to the results obtained from modeling. Tendons that were shown to reduce the flow of thermal energy through the specimen in the finite element models appeared as cool lines on the unheated surface in actual thermal images. Tendons which increased the flow of thermal energy through the specimen in the finite element models appeared as warm lines on the unheated surface in the thermal images. Since the models were only two-dimensional, actual temperature differentials obtained during laboratory testing did not precisely match the temperature differentials obtained with the models.

Passive solar heating, heating with silicone rubber flexible heating blankets, and heating using an infrared heater provided the thermal energy to cause a temperature gradient through the thickness of the specimens. Detection of simulated voids and post-tensioning tendons in a 20 cm (8 in) thick specimen with 5 cm (2 in) of concrete cover was possible with a temperature gradient of 11.1°C (20°F) obtained from solar heating. For larger concrete cover depths, a larger temperature gradient was required. A 75°C (135°F) temperature gradient achieved using the infrared heater was sufficient to detect a HDPE post-tensioning duct filled with 20 steel strands. This duct was embedded in a 30 cm (12 in) thick specimen with 15 cm (6 in) of concrete cover. In order to detect tendons at this large depth of concrete cover, a significant difference in the

thermal conductivity of the specimen was required. Examples would be tendons with the large 15 cm (6 in) long by 8.5 cm (3.3 in) thick simulated voids embedded in HDPE ducts or tendons constructed with 30 post-tensioning steel strands and steel post-tensioning ducts.

Simulated voids embedded in the HDPE and steel post-tensioning ducts were detected when concrete cover depths were less than 10 cm (5 in). At concrete cover depths larger than 10 cm (5 in), simulated voids were difficult to detect with the temperature gradients achieved with the heating methods used. Simulated voids embedded in HDPE ducts were easier to distinguish than simulated voids embedded in steel ducts.

The locations of some of the tendons and some of the simulated voids were detected in the 30 cm (12 in) thick specimens. During tests using the infrared heater, surface temperatures of the concrete were as high as 135°C (275°F). From the research conducted, 15 cm (6 in) is the depth of concrete cover that can be present in a 30 cm (12 in) thick specimen and still detect the location of the tendons using an infrared heater. The location of any of the tendons and simulated voids were not detected in the 40 cm (16 in) thick specimens.

Insulating the boundary edges of the specimens used during testing conducted with solar heating made detection of the tendons across the entire width of the specimens easier. As seen in Figures 5.2 through 5.5 and discussed by Pearson (2003), edge heating of the specimens caused by direct sunlight shining on the edges of the specimens resulted in large temperature variations across the surface of the specimens. Detection of the tendons and simulated voids was difficult with the thermal camera because of the large variation in temperature across the surface of the specimens. Figures 5.6 through 5.10 illustrate the improvement gained by insulating the edges of the specimens. Temperature variations across the surface of the specimens were reduced when the insulating barriers were installed around the perimeter of the specimens.

The use of both the silicone rubber thermal heating blankets and the infrared heater was successful in creating larger temperature differentials across the thickness of the specimens compared to passive solar heating. The maximum temperature differential obtained in 20 cm (8 in) thick concrete specimens using solar heating was approximately 11.1°C (20°F). The maximum temperature differential obtained in 30 cm (12 in) thick concrete specimens using solar heating was approximately 12.2°C (22°F). All of the tendons and simulated voids detected using solar heating were:

- A steel duct containing 20 post-tensioning steel strands and no simulated voids with 5 cm (2 in) of concrete cover embedded in a 20 cm (8 in) thick specimen.
- A steel duct containing 30 post-tensioning steel strands and no simulated voids with 5 cm (2 in) of concrete cover embedded in a 20 cm (8 in) thick specimen.
- A steel duct containing 30 post-tensioning steel strands and a 15 cm (6 in) long by 3.7 cm (1.5 in) thick simulated void with 5 cm (2 in) of concrete cover embedded in a 20 cm (8 in) thick specimen.
- A HDPE duct containing four post-tensioning steel strands and a 15 cm (6 in) long by 8.5 cm (3.3 in) thick simulated void with 5 cm (2 in) of concrete cover embedded in a 20 cm (8 in) thick specimen.
- A HDPE duct containing 20 post-tensioning steel strands and a 5 cm (2 in) long by 5.2 cm (2.1 in) thick simulated void and a 10 cm (4 in) long by 5.2 cm (2.1 in) thick simulated void with 5 cm (2 in) of concrete cover embedded in a 20 cm (8 in) thick specimen.
- A steel duct containing 30 post-tensioning steel strands and no simulated voids with 5 cm (2 in) of concrete cover embedded in a 30 cm (12 in) thick specimen.

The silicone rubber heating blankets achieved a maximum temperature differential through the thickness of a 20 cm (8 in) thick specimen of approximately 38.9°C (70°F). The maximum temperature differential obtained in 30 cm (12 in) thick concrete specimens using the heating blankets was approximately 36.1°C (65°F). All of the tendons and simulated voids detected using the silicone rubber flexible heating blankets were:

- A steel duct containing 20 post-tensioning steel strands and no simulated voids with 5 cm (2 in) of concrete cover embedded in a 20 cm (8 in) thick specimen.
- A steel duct containing 30 post-tensioning steel strands and no simulated voids with 5 cm (2 in) of concrete cover embedded in a 20 cm (8 in) thick specimen.
- A HDPE duct containing four post-tensioning steel strands and a 15 cm (6 in) long by 8.5 cm (3.3 in) thick simulated void with 5 cm (2 in) of concrete cover embedded in a 20 cm (8 in) thick specimen.
- A HDPE duct containing 20 post-tensioning steel strands and a 10 cm (4 in) long by 5.2 cm (2.1 in) thick simulated void with 5 cm (2 in) of concrete cover embedded in a 20 cm (8 in) thick specimen.
- A HDPE duct containing 20 post-tensioning steel strands and no simulated voids with 12.5 cm (5 in) of concrete cover embedded in a 30 cm (12 in) thick specimen.

During testing using the infrared heater, the largest temperature differential obtained through the thickness of a 30 cm (12 in) specimen was approximately 86.1°C (155°F). All of the tendons and simulated voids detected using the infrared heater were:

- A HDPE duct containing 20 post-tensioning steel strands and a 5 cm (2 in) long by 5.2 cm (2.1 in) thick simulated void and a 10 cm (4 in) long by 5.2 cm (2.1 in) thick

simulated void with 15 cm (6 in) of concrete cover embedded in a 30 cm (12 in) thick specimen. The simulated voids inside the HDPE duct were not detected.

- A HDPE duct containing 30 post-tensioning steel strands and a 5 cm (2 in) long by 3.7 cm (1.5 in) thick simulated void and a 10 cm (4 in) long by 3.7 cm (1.5 in) thick simulated void with 15 cm (6 in) of concrete cover embedded in a 30 cm (12 in) thick specimen. The simulated voids inside the HDPE duct were not detected.
- A HDPE duct containing 20 post-tensioning steel strands and a 10 cm (4 in) long by 5.2 cm (2.1 in) thick simulated void with 5 cm (2 in) of concrete cover embedded in a 30 cm (12 in) thick specimen.
- A HDPE duct containing 30 post-tensioning steel strands and a 5 cm (2 in) long by 3.7 cm (1.5 in) thick simulated void and a 10 cm (4 in) long by 3.7 cm (1.5 in) thick simulated void with 5 cm (2 in) of concrete cover embedded in a 30 cm (12 in) thick specimen.

These results are significant since Pearson (2003) was only able to detect tendons with 5 cm (2 in) of cover in previous research using solar heating. These results show promise for using thermal imaging as a nondestructive inspection method for concrete box girder bridge walls.

The ability to detect simulated voids embedded in the concrete specimens was affected by the size of the simulated void. The large 15 cm (6 in) long by 8.5 cm (3.3 in) thick simulated void found in the center tendon of Specimen 2 was the easiest to detect with the thermal camera. On average, this size simulated void caused a 2°C (3.6°F) temperature change on the surface of the specimen in a 20 cm (8 in) thick specimen. Smaller simulated voids caused less temperature change on the specimen surface, making detection more difficult. A small 5 cm (2 in) long by 3.7 cm (1.5 in) thick simulated void was detected in a 30 cm (12 in) thick specimen during tests

using the infrared heater, but caused only a 0.3°C (0.5°F) temperature change on the surface of the specimen. This temperature change was almost undetectable with the thermal camera. This was also attributed to the variation in temperature across the specimen face increasing the temperature range used by the thermal camera. Pearson (2003) noted that if the thermal camera was set to a temperature range of 10°C (18°F) or larger, temperature differences of 0.1°C (0.2°F) on the surface of the specimens were difficult to distinguish. Keeping the temperature difference on the surface of the specimens smaller than 10°C (18°F) should facilitate detection of the 5 cm (2 in) long by 3.7 cm (1.5 in) thick and smaller simulated voids.

**7.2 – Inspection Guidelines**

The following inspection guidelines are combined from the research discussed in this report and the research conducted by Pearson (2003) at Washington State University for inspecting post-tensioned concrete bridge systems using thermal imaging.

- Sunlight shining directly on the concrete surface can obscure small surface temperature differences caused by the subsurface conditions. The best time to obtain thermal images of concrete that has been exposed to direct sunlight is just after sundown (Pearson, 2003)
- The time it takes for thermal energy to propagate through a given thickness of concrete can be determined given that normal weight concrete conducts thermal energy at an approximate rate of 7.5 cm/hour (3.0 in/hour) (Pearson, 2003). For example, the time for thermal energy to propagate through a 20 cm (8 in) thick concrete specimen is approximately 2.7 hours. The time for the thermal energy to propagate through a 30 cm (12 in) thick concrete specimen is approximately 4 hours.

- To detect the location of tendons and simulated voids in concrete sections where the depth of concrete cover to the tendons is greater than 5 cm (2 in), a silicone rubber flexible heating blanket or infrared heater should be used to obtain a greater temperature gradient through the specimen thickness.
- An insulating shield can be applied to the surface of the silicone rubber flexible heating blankets not in contact with the specimen to minimize the thermal energy lost into the surrounding environment. The plywood shield used in the research increased the heated surface temperature of the specimens approximately 11.1°C (20°F).
- When uneven surface temperature distributions appear, removing the heat source to allow the temperature differences to equalize may help in obtaining a quality thermal image. However, if the heat source is removed for more than two hours, the specimen will cool too much to detect the location of tendons and simulated voids.
- The best color palette to use when taking thermal images using the FLIR Systems ThermaCAM P60 was the Rainbow HC color palette. Small temperature differences were easier to distinguish using the Rainbow HC color palette compared to the other color palettes available.

### 7.3 – Future Research

Further research should be conducted to continue investigating thermal imaging as a viable tool for inspecting post-tensioned box girder bridges. New specimens could be constructed to address a broader range of post-tensioning steel strand/post-tensioning duct layouts. Thinner simulated voids should be used in some tendons since the thinnest detected simulated void was 3.7 cm (1.5 in). These simulated voids could be as thin as 1.3 cm (1/2 in) to

simulate small voids in the grout of a post-tensioned box girder bridge wall. Larger specimens could be constructed to reduce the edge heating observed during testing using passive solar heating.

Focus should also be directed toward the use of infrared heaters. The infrared heater used in the research was not the same size as the specimens, causing an uneven heat distribution across the specimen surface. An infrared heater constructed with dimensions similar to the dimensions of the specimens would provide a more even heat distribution. An adjustable thermostat installed on the silicone rubber heating blankets would also be beneficial. As seen during the research, the preset thermostats used on the heating blankets were not precisely calibrated and caused an uneven temperature distribution on the specimens at times. Having the ability to regulate the temperature of the heating blankets more closely and being able to choose the maximum temperature the blankets operate at would be beneficial. Finally, inspections should be conducted on an actual bridge to compare the trends and results obtained in the laboratory with actual field conditions.

### 7.4 - Acknowledgements

Funding for this project was provided by the Federal Highway Administration through contract number DTFH61-03-C-00104. The post-tensioning steel strands and the steel post-tensioning ducts were provided by Central Pre-Mix Prestress in Spokane, Washington. The HDPE post-tensioning ducts were provided by General Technologies Inc. of Stafford, Texas.

# References


Alexander, D.R., Krause, J.K., and Poulain, D.E. (1999). "Evaluation of Rebar Corrosion in Concrete by Active Thermal Sensing." University of Nebraska-Lincoln, <http://gulliver.trb.org/publications/circulars/circ498/v1_B07.pdf>.

Allen, L.R., and Stockton, G.R. (1999). "Using Infrared Thermography to Determine the Presence & Correct Placement of Grouted Cells in Single Width Concrete Masonry Unit (CMU) Walls." *Thermosense XXI*, SPIE – The International Society for Optical Engineering, 483-493.

ASHRAE (1989). "Thermal and Water Vapor Transmission Data." *1989 Fundamentals Handbook*, American Society of Heating, Refrigerating, and Air-Conditioning Engineers, Inc., (ASHRAE), Atlanta, Georgia.

Beitelman, T.E. (2000). "Tensile Test Results of Post Tensioning Cables From the Midbay Bridge." Structures Research Center, Florida Department of Transportation, <http://ravenelbridge.net/post_tensioning_midbay_bridge.pdf>.

Breen, J.E., Kreger, M.E., Salas, R.M., Schokker, A.J., and West, J.S. (2004). "Conclusions, Recommendations, and Design Guidelines for Corrosion Protection of Post-Tensioned Bridges." Center for Transportation Research, University of Texas at Austin, <http://www.utexas.edu/research/ctr/pdf_reports/0_1405_9.pdf>.

Bugini, R., Della Torre, S., Rampazzi, L., Rosina, E., Sansonetti, A., and Segattini, R. (2003). "Merging Nondestructive Testing Techniques for Stucco Analysis: The Case Study of St. Abbondio in Como, Italy." *Materials Evaluation*, (61)5, 604-610.

Callister, W.D. (2001). *Fundamentals of Material Science and Engineering*, 2nd Edition, John Wiley & Sons, Inc., New York.

Cement Association of Canada. (2003). "Cold Weather Concreting." Ottawa, Ontario, <http://www.cement.ca/cement.nsf>.

Chajes, M., Hunsperger, R., Kunz, E., Li, J., and Liu, W. (2003). "Void Detection in Grouted Post-Tensioned Bridges Using Time Domain Reflectometry." Department of Civil and Environmental Engineering, University of Delaware, <http://www.ece.udel.edu /~hunsperg/corrosion/index.html>.

Chandra, V., Collard-Jenkins, S.J., Pearson-Kirk, D., and Theryo, T. (2004). "Improving the Durability of Segmental Bridges." *Segmental Bridges*, Vol. XIX, No.57.

Conner, J. (2004). "Detection of Tendons and Voids in Grouted Duct Using Ground-Penetrating Radar." *Masters Thesis*, Washington State University.

Del Grande, N.K., Durbin, P.F., Logan, C.M., Perkins, D.E., and Schaich, P.C. (1996). "Demonstration of Dual-Band Infrared Thermal Imaging at Grass Valley Creek Bridges." *Nondestructive Evaluation of Bridges and Highways*, SPIE – The International Society for Optical Engineering, 166-177.

DeWitt, D.P., and Incropera, F.P. (1996). *Introduction to Heat Transfer*, 3rd Edition, John Wiley & Sons, Inc., New York.

Fiorato, A.E., and Van Geem, M.G. (1983). "Heat Transfer Characteristics of a Structural Lightweight Concrete Wall." Oak Ridge National Laboratories, Oak Ridge, Tennessee.

FLIR Systems. (2005). "ThermaCAM P60 Infrared Camera." Boston, Massachusetts, <http://www.flirthermography.com/brazil/cameras/camera/1016/>.

Florida Department of Transportation. (2001). "Mid-Bay Bridge Post-Tensioning Evaluation." Tallahassee, Florida, <http://www.dot.state.fl.us/structures/Memos/TemporaryDesign BulletinC01-01.pdf>.

Florida Department of Transportation. (2002). "Grouting of Bridge Post-Tensioning Tendons." Tallahassee, Florida, <http://www.dot.state.fl.us/construction/Training/Final%20Grouting%20Training%20Manual%207-30-02.pdf>.

Forest Products Laboratory. (1987). "Fire Safety in Wood Construction." *Wood Handbook: Wood as an Engineering Material*, Forest Service, United States Department of Agriculture.

Frank, K.H., Poston, R.W., and West, J.S. (2003). "Enduring Strength." *Civil Engineering*, (73)9, 58-63.

Goss, W.P., and James, T.B. (1993). *Heat Transmission Coefficients for Walls, Roofs, Ceilings, and Floors,* American Society of Heating, Refrigerating, and Air-Conditioning Engineers, Inc., (ASHRAE), Atlanta, Georgia.

Guthrie, W.S., and Hema, J. (2005). "Concrete Bridge Deck Assessment Guidelines." Department of Civil and Environmental Engineering, Brigham Young University, <http://www.dot.state.ut.us/download.php/tid=1293/UT-05.01.pdf>.

Hartt, W.H., and Venugopalan, S. (2002). "Corrosion Evaluation of Post-Tensioned Tendons on the Mid Bay Bridge in Destin, Florida." Florida Department of Transportation Research Center, <http://www.dot.state.fl.us/Research-Center/Completed_Proj/Summary_SMO/FDOT_033890_rpt.pdf>.

Hillemeier, B., and Rieck, C. (2003). "Detecting Voids Inside Ducts of Bonded Steel Tendons Using Impulse Thermography." Technische Universität, Berlin, Germany, <http://www.ndt.net/article/ndtce03/papers/p021/p021.htm>.

Hukseflux Thermal Sensors. (2005). "Thermal Conductivity Science." <http://www.hukseflux.com/thermal%20conductivity/thermal.htm>.

Infrared Training Center. (2003). *Level 2 Course Manual,* N. Billerica, Massachusetts.

Jones, T.J., and Botsko, R. (1995). "Thermal and Infrared Nondestructive Testing." *Nondestructive Testing Handbook,* American Society for Nondestructive Testing, 308-328.

Ludwig, N. (2003). "Thermographic Testing on Buildings Using a Simplified Heat Transfer Model." *Materials Evaluation,* (61)5, 599-603.

MatWeb. (2005). "Styrofoam Polystyrene Rigid Foam Insulation." <http://www.matweb.com/search/SpecificMaterial.asp?bassnum=PDWZ00>.

NDT Resource Center. (2001). "Introduction to Thermal Testing." <http://www.ndt-ed.org/EducationResources/CommunityCollege/Other%20Methods/IRT/IR_index.htm>.

Pearson, E.J. (2003). "The Feasibility of Thermal Imaging For The Location and Inspection of Post-Tensioning Cables in Concrete Box Girder Bridges." *Masters Thesis,* Washington State University.

Potter, J.L. (2002). "Status of Post-Tensioning Condition Evaluations and Enhancements." *2002 Concrete Bridge Conference,* Office of Bridge Technology, Federal Highways Administration.

Salazar, A. (2003). "On Thermal Diffusivity." *European Journal of Physics*, (24)4, 351-358.

Serluppens, R., and Shaw, P. (2000). "High Energy Radiography Combined with the Agfa Strukturix DPS-Imaging System and Comparison with Other NDE-Methods for Inspection of Thick Reinforced Concrete Structures." <http://www.ndt.net/article/v05n08/shaw/shaw.htm>.

University of Arizona. (2004). Department of Atmospheric Sciences, <http://www.atmo.arizona.edu>.

VSL International. (2002). "Grouting of Post-Tensioning Tendons." *VSL Report Series 5*, Subingen, Switzerland.